Theoretical and Numerical Investigations of Accretion-Ejection Mechanism around Compact objects

A

Thesis Submitted

To

Pt. Ravishankar Shukla University, Raipur

For

The Degree of Doctor of Philosophy

in

PHYSICS

under the Faculty of Science

2015

Supervisor :
Dr. Indranil Chattopadhyay
Scientist – E
ARIES, Nainital

Investigator :
Rajiv Kumar
ARIES, Manora Peak
Nainital – 263 002

Research Centre

Aryabhatta Research Institute of observational

sciencES (ARIES)

Manora Peak, Nainital 263 002, India

Declaration by Candidate

I declare that the thesis entitled ''Theoretical and Numerical Investigations of Accretion-Ejection Mechanism around Compact Objects'' is my own work conducted under the supervision of Dr. Indranil Chattopadhyay at Aryabhatta Research Institute of observational sciencES (ARIES), Nainital, Uttarakhand, India, approved by the Research Degree Committee. I have put in more than 200 days of attendance with the supervisor at the center.

I further declare that to the best of my knowledge the thesis does not contain any part of any work, which has been submitted for the award of any degree either in this University or in any other University/Deemed university without proper citation.

Indranil Chattopadhyay

Dr. Indranil Chattopadhyay
Signature of the Supervisor

SCIENTIST 'F'
ARIES, NAINITAL

Rajiv Kumar
Signature of the Candidate

Rajiv Kumar

10.03.2015
Signature of the Chairman, DRC

Professor
S.O.S. in
Pt. Ravishankar
RAIPUR, (C.G.) 492010

Certificate by the Supervisor

This is to certify that the work entitled ''Theoretical and Numerical Investigations of Accretion-Ejection Mechanism around Compact Objects'' is a piece of research work done by Mr. Rajiv Kumar under my guidance and supervision for the degree of Doctor of Philosophy in PHYSICS of Pt. Ravishankar Shukla University, Raipur (Chhattisgarh), India. That the candidate has put in an attendance of more than 200 days with me.

To the best of my knowledge and belief this thesis

1. Embodies the work of the candidate himself.
2. Has duly been completed.
3. Fulfills the requirements of the Ordinance relating to the Ph.D. degree of the University;
   and
4. Is up to the standard both in respect of contents and language for being referred to the examiner.

Indranil Chattopadhyay

Dr. Indranil Chattopadhyay
Signature of the Supervisor

SCIENTIST 'E'
ARIES, NAINITAL

Forwarded

10.07.2015

Signature of the Chairman, DRC

Professor & Head
S.O.S. in Physics & Astrophysics
Pt. Ravishankar Shukla University,
RAIPUR, (C.G.) 492010

Certificate no: Pre-PhD/2009-10../JRF-3

Aryabhatta Research Institute of Observational Sciences
(ARIES)

[An autonomous institute under the Department of Science & Technology (DST) - Govt. of India]

Manora Peak, Nainital

This is to certify that **Mr. Rajiv Kumar** son of Shri. Shivbalak Ram has successfully completed ARIES Pre-PhD coursework **2009 - 2010**. The coursework consists of (i) course on topics as per ARIES pre-PhD coursework syllabus related to Physics, Astronomy & Astrophysics, Atmospheric Sciences and Solar Physics (ii) courses on quantitative methods and computer applications (iii) course on research methodology leading to three months project supervised by one of the ARIES faculties.

Date: August, 2010

Place: Manora Peak, Nainital

Director

निदेशक,
एरीज मनोरापीक
नैनीताल.

APPENDIX – 5

Copy Right Transfer Approval Form

(Clause 14e of the Ordinance - 45)

Name of the Candidate:	RAJIV KUMAR
Department:	School of Studies in Physics and Astrophysics
Degree :	Doctor or Philosophy in Physics
University:	Pt. Ravishankar Shukla University, Raipur
Supervisor:	Dr. Indranil Chattopadhyay
Thesis Title:	Theoretical and Numerical Investigations of Accretion-Ejection Mechanism around Compact Objects
Year of Award:	.....

Agreement

1. I hereby declare that, if appropriate, I have obtained and attended hereto a written permission/statement from owner(s) of each third party copyrighted matter to be included in my thesis/dissertation, allowing distribution as specified below.
2. I hereby grant to the university and its agents the non-exclusive license to archive and make accessible, under the condition specified below, my thesis/dissertation, in whole or in part in all forms of media, now or hereafter known. I retain all other ownership rights to the copyright of the thesis/dissertation. I and my Supervisor, also retain the right to use in future works (such as articles or books) all or part of this thesis, dissertation, or project report.

Condition:

1. Release the entire work for access worldwide

Rajiv Kumar

Signature of the Candidate

Place Nainital

Date 05/03/2015

Indranil Chattopadhyay

Signature and Seal of the Supervisor

SCIENTIST 'E'
ARIES, NAINITAL

SCHOOL OF STUDIES IN PHYSICS AND ASTROPHYSICS
Pt. RAVISHANKAR SHUKLA UNIVERSITY,
RAIPUR - 492010 , CHHATTISGARH (INDIA)

Dr. R. N. Baghel
Ph. D. (IIT Delhi), MCA,
Diploma in English,
Prof. & Head

Phone : (Mo) 9198934-24482
: (O) (0771) 2262864
: (R) (0771) 2262739
Fax : (0771) 2262583,2262857
Email : rnbaghel20@gmail.com

Ref. :...1068/Phy./15.

Date :...12.02.2015.....

Plagiarism Verification Report

This is to certify that plagiarism verification test of the Ph.D thesis submitted by **Mr. Rajiv Kumar** entitled "**Theoretical and Numerical Investigations of Accretion - Ejection Mechanism around Compact Objects**" has been carried out by the **ITHENTICATE** software available at **Pt. Sunder Lal Sharma library** of **Pt. Ravishankar Shukla University, Raipur (C.G.) India.** On the basis of its report it has been found that the percentage of similarity is 2% excluding scholar's own publications, that is within acceptable limit (less than 20%).

Hence DRC recommends that the thesis may be dispatched to the reviewers for further action.

Chairman

Departmental Research Committee (DRC)
School of Studies in Physics & Astrophysics
Pt. Ravishankar Shukla University, Raipur,
Chhattisgarh, 492010 India

SCHOOL OF STUDIES IN PHYSICS AND ASTROPHYSICS
Pt. RAVISHANKAR SHUKLA UNIVERSITY,
RAIPUR - 492010 , CHHATTISGARH (INDIA)

Dr. R. N. Baghel
Ph. D. (IIT Delhi), MCA,
Diploma in English,
Prof. & Head

Phone : (Mo) 9198934-24482
: (O) (0771) 2262864
: (R) (0771) 2262739
Fax : (0771) 2262583,2262857
Email : rnbaghel20@gmail.com

Ref. : 1040

Date : 10.03.2015

CERTIFICATE

This is to certify that **Rajiv Kumar** has given Pre-Ph.D. seminar on his thesis entitled **"THEORETICAL AND NUMERICAL INVESTIGATIONS OF ACCRETION-EJECTION MECHANISM AROUND COMPACT OBJECTS"**, on **10.03.2015** at School of Studies in Physics & Astrophysics, Pt. Ravishankar Shukla University, Raipur.

Chairman
Departmental Research Committee
SoS in Physics & Astrophysics
Pt. Ravishankar Shukla University, Raipur

This thesis is dedicated to,

My parents, my wife and well wishers.

Contents

Acknowledgements **vii**

Abstract **ix**

List of Publications **xi**

Notations and abbreviations **xiii**

List of Figures **xvii**

1 Introduction **1**

1.1 Compact Objects 1

1.1.1 Energy released by black holes 2

1.1.2 Observations of black holes and features 3

1.2 Theoretical models 7

1.2.1 Disc Theories 8

1.2.2 Aim of the thesis 10

1.2.3 Pseudo-Newtonian Potential 10

2 Governing equations and Assumptions **13**

2.1 Pseudo-Newtonian approach: 13

2.1.1 Equations of motion for accretion disc 16

2.1.2 Shock equations: 18

2.1.3 Jet geometry and jet equations of motion: 20

2.2 General Relativistic approach: 22

2.3 Equation of state (EoS): 24

3 Accretion-Ejection in pseudo - Newtonian description **29**

3.1 Fluid equations with fixed Γ 29

3.2 Solution Procedure 32

3.2.1 Method to find the sonic point 32

3.2.2 Method to find the shock 34

3.2.3 Self-consistent accretion-ejection solution 35

3.3 Study of viscous accretion disc: 37

3.3.1 All possible accretion solutions in the advective regime: 37

3.4 Study of radiatively-thermally driven outflows from the disc: 48

3.4.1 Radiative moments 48

3.4.2 Accretion-ejection solutions: 53

3.4.2.1 Effect of post-shock radiation on jet acceleration 54

3.4.2.2 Effect of pre-shock radiation on jets 57

3.4.2.3 Radiative driving of jets with computed post-shock and pre-shock radiations 60

3.5 Comparison of numerical simulation with analytical solutions 65

3.5.1 Basic equations 65

3.5.2 The code 66

3.5.2.1 Hydrodynamic part in multi-dimensional geometry . . . 66

3.5.2.2 Viscosity part 67

3.5.3 Results 68

4 Flow solutions with variable Γ around black holes **75**

4.1 Adiabatic flow with PW-potential 75

4.1.1 Solution procedure and Study of multispecies adiabatic flow . . . 78

4.1.1.1 Nature of critical points and accretion flow solutions . . 79

4.1.1.2 Accretion and ejection solutions 86

4.2 General fluid flow with PW-potential 93

4.2.1 Solution procedure 95

4.2.2 All possible transonic accretion solutions for $e^- - p^+$ flow 96

4.2.2.1 Dissipative shock in accretion flow 104

4.2.2.2 Hyper-accretion rate 108

4.2.3 Accretion-ejection in dissipative flow 110

4.3 Study of advective accretion disc in General relativistic approach: 111
4.3.1 Solution procedure 114
4.3.1.1 Method to find L_0 and Θ_{in} 115
4.3.1.2 Method to find sonic point and shock 116
4.3.2 All possible accretion solutions 116
4.3.3 Accretion-ejection solutions 120

5 Discussion and conclusion **125**
5.1 Discussion with chapters 125
5.2 Thesis summary and Future prospects 131

A Estimation of post-shock luminosity from pre-shock radiations **133**

Bibliography **137**

Acknowledgements

It is my great pleasure to express my sincerest gratitude to my supervisor Dr. Indranil Chattopadhyay who has given me inspiring guidance, enthusiasm and persistent support throughout the years of my Ph.D. period. I am indebted to him for introducing me to this fascinating topic of astrophysics and giving me the opportunity to work in his guidance. He has always motivated me to find my goals during my thesis work. Working under his guidance has been a rich and rare experience and certainly will help in the future path of my life.

I would like to thank all academic and non-academic staff members of ARIES, Nainital. I thank all the scientists of ARIES who have taught me various courses during my pre-Ph.D. course work. Special thank to Dr. Brijesh Kumar and Dr. Hum Chand for their invaluable advises and motivation throughout my Ph.D. period. I would also like to thank Pt. Ravi Shankar Shukla university, Raipur who has registered me for the degree of philosophy.

I would also like to thank my collaborators Prof. Sandip K. Chakrabarti, Dr. Samir Mandal and Dr. Chandra B. Singh for their invaluable advises and inspiring me for hard work. I also thank the organizers of various conferences who provided me the opportunity to attend them. Attending these conferences gave me a broad overview of field of astrophysics and astronomy and enriched me with essence of the subject.

I would also like to acknowledge the ARIES, its library, computer center and administrative staff for providing the academic and computing facilities required to complete this thesis. I would like to thank all my seniors and friends within the ARIES, for there constant help and suggestions. Special thanks to Arti, Neelam, Jessy, Manash, Rupak, RamKesh, Brajesh, Eswar, Sumana, Chrisphin, Hema, Rajesh, Narendra, Ravi, and Tapaswini for their valuable advice, understanding and help whenever needed. Warm thanks also goes to my batch-mates and office room-mates Devesh, Haritma, Sumit,

Krishna, Archana, Rashmi. And I also express thanks to all juniors for their nice company, specially to Subhash, Mukesh and Abhishek.

I would also like to thank my friends from my hometown for there help in my personal life and their nice company. Special thanks to Sanjeev, Brajendra, Gyanu, Kuldeep, Veeru, Dr. Pawan and Dr. Rinko.

Last but not the least, the main encouragements behind this effort came from my family. I thank my parents, my elder sister and my cousins for their love, blessing and support in my life. Special thanks to my wife for her love and support.

Abstract

The goal of this thesis is to understand the black hole accretion process, outflows and jets, and predict its observational properties. In the study of accretion disc, the highly non-linear process involves a transport of angular momentum by turbulent viscosity process and dissipation in the disc by various dissipative process. The disc in a full general relativistic regime is a very hard to study analytically. So here firstly, we have study analytically hydrodynamic disc with using pseudo-Newtonian geometry around compact objects then using full general relativistic approach. Pseudo-Newtonian potential carrys essential properties of general relativity such as the location of marginally stable orbit, the location of marginally bound orbit and the location of photon orbit and their corresponding angular momentum values. So, this mimic the black hole geometry with general relativity. This Pseudo-potential is given by and also known as Paczyński and Wiita (1980) potential.

Our accretion solutions are stationary, axisymmetric without or with turbulent viscosity in the disc around non-rotating black holes. We have developed all type of possible accretion solutions in a self-consistent manner for non-dissipative or dissipative process in the disc. We have mainly focused on shock disc solutions and jets solutions by assuming jets flow geometry around black hole with their corresponding disc luminosities. The accretion solutions have also been studied with time dependent numerical simulation by us. We want to check how well our numerical simulations by state of the art simulation code, can reproduce our analytical solutions, and thereby acts as check of our predictions based on analytical result.

This thesis mainly focused on two things, which are the origin of jets and the dynamics of the accretion discs. How does a collimated outflow arise from the hot accretion disc and spiraling into a central object ? Why do jets appear to turn “on” and “off” as the accretion disc changes spectral states ? So, it is mainly divided into

two parts one explains the dissipative and non- dissipative accretion disc model and other focused on jet geometry and outflow mechanism. These two main parts are also further divided into two parts on the basis of fixed and variable adiabatic index (Γ) equation of states for the fluids and in final part, I have concluded my work.
This thesis presented here is based on the articles, which have already been published or to be submitted in the refereed journals.

List of Publications

1. 'Estimation of the mass outflow rates from viscous accretion discs'; **Kumar R.**, Chattopadhyay I., 2013, MNRAS, 430, 386.

2. 'Effect of the flow composition on outflow rates from accretion discs around black holes'; **Kumar R.**, Singh C. B., Chattopadhyay I., Chakrabarti S. K., 2013, MNRAS, 436, 2864.

3. 'Radiatively and thermally driven self-consistent bipolar outflows from accretion discs around compact objects'; **Kumar R.**, Chattopadhyay I., Mandal S., 2014, MNRAS, 437, 2992.

4. 'Dissipative advective accretion disc solutions with variable adiabatic index around black holes'; **Kumar R.**, Chattopadhyay I., 2014, MNRAS, 443, 3444.

5. 'Time-dependent viscous accretion flow in two-dimensional cylindrical geometry'; Lee S-J, Chattopadhyay I., **Kumar R.**, Ryu D., Hyung S. *to be submitted soon.*

6. 'Estimation of mass outflow rates from general relativistic advective accretion discs'; Chattopadhyay I. **Kumar R.** *to be submitted soon.*

Conference proceedings

1. 'Study of jet properties around compact objects with the change in accretion disc parameters'; **Kumar, R.**, Chattopadhyay, I., Mandal, S., 2013, ASInC, 8, 147.

2. 'Accretion disc spectrum in presence of mass outflow around black holes'; Mandal, S., **Kumar, R.**, Chattopadhyay, I., 2013, ASInC, 8, 45.

3. 'Viscous accretion disc around black holes with variable adiabatic index'; Chattopadhyay, I., **Kumar, R.**, 2013, ASInC, 8, 19.

4. 'Effect of equation of state and composition on relativistic flows'; Chattopadhyay, I., Mandal, S., Ghosh, H., Garain, S., **Kumar, R.**, Ryu, D., 2012, ASInC, 5, 81.

Notations and abbreviations

The most commonly used notations and abbreviations in the thesis are given below. If a symbol has been used in a different connection than listed here, it has been explained at the appropriate place.

Notations

x, r	radial distance
λ	specific angular momentum
α	viscosity parameter
ξ	composition Parameter
a	sound speed
Γ	adiabatic index
ρ	mass density
v	bulk velocity of fluid
Θ	temperature of the fluid
k	Boltzman constant of gas
G	Universal gravitational constant
c	speed of light
r_g	Schwarzschild radius
x_s, r_s	shock location
kpc	kiloparsec (unit of distance)
L_{Edd}	Eddington luminosity
$\dot{M}_{Edd}$	Eddington mass accretion rate
$\dot{m}$	accretion rate in unit of $\dot{M}_{Edd}$
$\dot{\mathcal{M}}$	entropy-accretion rate
$\dot{\mathcal{M}}_{out}$	entropy-outflow rate

$R_{\dot{m}}$	outflow rate
M	Mach number
$\dot{M}$	mass-accretion rate
$\mathcal{K}$	entropy constant
$\mathcal{E}$	Bernoulli parameter (specific energy of the flow)
E	grand specific energy of the flow
ε	generalized Bernoulli parameter
$M_{\odot}$	mass of the Sun
h	enthalpy of the fluid
M_B	mass of the Black hole
pc	parsec (unit of distance)

Abbreviations

ADAF	Advection Dominated Accretion Flow
AGN	Active Galactic Nuclei
ARIES	Aryabhatta Research Institute of observational SciencES
BC	Boundary Condition
BH	Black Hole
BHC	Black Hole Candidate
CP	Critical Point
EoS	Equation of State
GR	General Relativity
HID	Hardness-Intensity Diagram
HS	High Soft state
Hz	Hertz
IBC	Inner Boundary Condition
IMBH	Intermediate Mass Black Hole
IS	Intermediate State
LS	Low Hard state
MCP	Multiple Critical Point
OBC	Outer Boundary Condition

PW-potential	Paczynski-Wiita potential
QPO	Quasi-Periodic Oscillation
SBH	Stellar-mass Black Hole
SMBH	Super Massive Black Hole
SPS	Shock Parameter Space
ULXs	Ultra Luminosous $X-$ ray source
VHS	Very High State
VLBA	Very Long Base-line Array

List of Figures

1.1 HID or $Q-$diagram 6

2.1 Jet geometry 20

3.1 MCP 38
3.2 Effect of viscosity 40
3.3 Comparison of shock and shock free solutions 42
3.4 Effect of BC 44
3.5 Shock parameter space 47
3.6 Cartoon for disc-jet system 48
3.7 Distribution of radiative moments 49
3.8 Accretion-ejection with Mach number 52
3.9 Effect of post-shock luminosity on jet flow variables 55
3.10 Effect of post-shock luminosity 56
3.11 Effect of pre-shock luminosity on jet flow quantities 58
3.12 Effect of pre-shock luminosity 59
3.13 Variation of shocks and outflow rate 61
3.14 Stages of increasing jet strength 63
3.15 Comparison of SPS with and without outflow 64
3.16 Shock free simulation and analytical solution 69
3.17 Bulk velocity field 70
3.18 Shock simulation and analytical solution 72
3.19 Precursor for outflow 73
3.20 Shock simulation and analytical viscous solution 74

4.1 Effect of λ on CP 80

4.2 Effect of ξ on CP 81
4.3 MCP space 82
4.4 Multiple shock transitions 84
4.5 Accretion flow quantities 85
4.6 Accretion-ejection solutions 87
4.7 Nature of $R_{\dot{m}}$ with $\mathcal{E}, \lambda$ 88
4.8 Nature of $R_{\dot{m}}$ with ξ, λ 90
4.9 $R_{\dot{m}}^{m}$ with ξ 91
4.10 Shock -domains with ξ 92
4.11 Division of parameter space 97
4.12 Effect of α and $\dot{m}$ 98
4.13 Effect of α and $\dot{m}$ with fixed either OBC or IBC 101
4.14 Variation of emissivity 103
4.15 Non-dissipative SPS 105
4.16 Comparison of non-dissipative and dissipative shocks 106
4.17 SPS for non-dissipative and dissipative shocks 107
4.18 SPS and luminosities 109
4.19 Mass outflow rate in dissipative disc 110
4.20 Variation of accretion flow variables 117
4.21 Division of parameter space 119
4.22 Jet flow variables 121
4.23 Mass outflow rate 122

A.1 Variation of shock location and photon index 135

1

Introduction

1.1 Compact Objects

Compact objects from stars are "born" when a normal star "dies", i.e., when most of their nuclear fuels have been used up. There are three kind of compact objects white dwarfs (least relativistic), neutron stars (highly relativistic) and black holes (the most relativistic). Out of all the three types of stellar residuals, stellar mass black holes (SBH) are formed either from core collapse of massive stars (Genzel et al. 2010; Mirabel & Rodrigues 2003) and/or by accreting materials onto other compact objects. Masses of these SBHs are typically around few to few tens of solar mass ($M_{\odot}$). However, the massive variety of such 'beasts' are also found in centers of many dormant and active galaxies, their typically masses are in the range $10^{6-9}M_{\odot}$ and they are called as super-massive black holes (or SMBH). The mechanism to form such beasts are still a matter of serious research. But people have also predicted a third variety of black holes, which is known as intermediate mass black holes (or IMBH) and they possess a mass range from $10^{2-5}M_{\odot}$ (e.g. $M82\ X-1$ having mass around $400M_{\odot}$, Pasham et al. 2014).The formation mechanism and presence of such type of black holes are also not clear but probably they are found in the center of clusters in the galaxy. This later class of objects or IMBHs are tentatively identified with Ultra Luminous $X-$ ray sources or ULXs with $X-$ ray luminosity in excess of the Eddington luminosity of normal SBHs (Colbert & Ptak 2002; Liu & Mirabel 2005; Fabbiano et al. 2006; Feng & Soria 2011; Swartz et al. 2011).

1.1.1 Energy released by black holes

One of the most mysterious object in the universe is a black hole. The technical definition of a black hole is that it is an object whose gravity is so strong that nothing, including light can escape from within it. A black hole, in fact it does not have any hard surface or an environment of its own, but pulls matter and radiation in its vicinity, towards it with greater gravity than any other object in the Universe. Since it is impossible to directly observe a black hole, their presence can be inferred from their gravitational influence on nearby stars and gas, i. e., by the radiation that is emitted from the accretion disc.

Classically, a mass of a black hole M_B is entirely compressed into a region with zero volume. This zero volume, infinitely dense region is called as gravitational or space-time singularity. This space-time singularity is separated from external space-time by a surface or a one way membrane known as "**event horizon**". Event horizon is defined by a distance from the central singularity, where the escape velocity is equal to the speed of light c, and is expressed as $r_g = 2GM_B/c^2$. This radius, r_g is also known as Schwarzschild radius or gravitational radius and G is universal gravitational constant.

Simple minded back of the envelope calculation shows that, if we consider an object of mass m falling from a large distance onto the surface of a star of mass M and radius R, then the amount of energy liberated is $\sim GMm/R$. If R is replaced by r_g then this energy release becomes roughly equal to the object's rest mass energy $\sim mc^2$. In other words, it is a fundamental property of the black hole that, if matter is accreting on to a black hole then it can efficiently convert a large fraction of its rest mass energy into other form of energy before it crosses the event horizon of the black hole. The study of black hole accretion is important for various reasons. Black holes may be considered as the final frontier of general theory of relativity. Identification of black holes in astrophysical sources that are thought to harbour these beasts, need a thorough understanding of matter behaviour around it. And radiations from such matter should leave a telltale signature of the strength of the gravity. Timing and spectral properties of astrophysical sources which are black hole candidates (BHC), show many behavioral differences from astrophysical sources which harbour other compact objects like neutron star and white dwarfs, but there is no consensus within the scientific community that these observational differences arise due to the effect of the black hole space-time. Both

theory and observations need to develop even further to pin point the signature, but still the effort to do so enhances our understanding of nature, and definitely a step towards the final goal.

1.1.2 Observations of black holes and features

The accretion of matter onto compact objects is supposed to be the fundamental mechanism powering a variety of high energy astrophysical sources, such as low-mass X-ray binaries and active galactic nuclei. What happens to the energy that is liberated by a BHC each time an object falls in? There are several possibilities, a part of the energy released will increase its kinetic energy, another part of the energy released will heat up the matter making the matter around black holes hotter. An amount of the generated heat may also be liberated in the form of radiation, which makes these objects luminous. Therefore, the region around the BHC are hot and luminous, and in such extreme environment photon-photon or photon-particle interaction may be prevalent and may as well create particles. This will definitely change the composition of the fluid around a black hole, and therefore the accretion disc near a black hole may be described by a fluid which is composed many types of particles.

Initially scientists were intrigued by the enormous luminosity of quasars (quasi stellar radio sources) and AGNs (Active Galactic Nuclei), in which the luminosities were around 10^{43-48}ergs/s. It was clear that nuclear reactions cannot generate such enormous luminosity, more over the spectra from these objects were dominated by non-thermal components, which convinced the community that these objects cannot be stars. Motion of matter around its center and other features like Doppler shift of emission lines suggested central objects of masses in the range $10^{6-9}\ M_{\odot}$ at the centers of these galaxies, and yet the object having such mass couldn't be resolved. This fueled the idea of gigantic black holes residing at the center of quasars and AGNs and it was proposed that it was the action of black holes onto the ordinary matter of the galaxy that is fueling the enormous energy release from these objects. This led to the opening up of the topic of relativistic accretion discs.

Not only centers of active galaxies, even in our galaxy some of the X-Ray binaries show enormous luminosity. For example, the high mass X-ray binary Cyg X-1 (Bowyer et al. 1965) has a luminosity of $L \sim 3 - 4 \times 10^{38}$ ergs/s. Cyg X 1 was discovered in 1964 during a rocket flight and is one of the strongest X-ray sources seen from

the Earth, producing a peak X-ray flux density of $2.3 \times 10^{-23} W m^{-2} Hz^{-1}$ (2.3×10^3 Jansky)(Lewin & van der Klis 2006). Studying its companion, a blue super giant HDE 226868 (Ziółkowski 2014), gives an estimated mass of an unresolved primary attractor to be around $14 M_\odot$. This was the first X-Ray binary where the primary was proposed to be a black hole. Subsequently, many more Galactic sources have been found which are identified as BHC. The term microquasar was first coined for a X-ray binary 1E1740.7-2942, because it exhibited double sided parsec scale radio jets much like scaled down quasar (Mirabel et al. 1992). Another highly variable, luminous, low-mass X-ray binary source is GRS1915+105 observed by GRANAT satellite (Castro-Tirado et al. 1992; Greiner 2001).This galactic X-ray binary has been observed as a first superluminal motion of ejected matter in our galaxy, and having jet velocity $\sim 0.92c$ (Mirabel & Rodríguez 1994).

These microquasars exhibit luminosity range of 10^{36-39}ergs/s and masses around a few to few $\times 10 M_\odot$. They show two canonical spectral states in their spectrum, one the 'canonical soft state or high soft state (HS)' peaks in the soft X-ray range, is more luminous but have dominant thermal component. The other state called the 'canonical hard state or low hard state (LS)' is dominated by power-law and peaks in hard X-ray range, but in this state the luminosity of the source goes down (Gallo et al. 2003).These two states may be connected by a series of intermediate states as observed in many sources, e.g., GRS1915-105 and GRO J1655-40 (Sobolewska et al. 2009).

Moreover, the microquasars exhibit quasi-periodic oscillations (QPOs) in the hard state (both LS and intermediate hard state or IS) in the light curve (Remillard & McClintock 2006), and only the hard photons exhibits this temporal property (Shaposhnikov et al. 2007; Shaposhnikov & Titarchuk 2007; Miller-Jones et al. 2012). The frequency of QPOs evolve along with the spectral states in out-bursting sources, starting from the LS to the IS/VHS (Shaposhnikov & Titarchuk 2009; Nandi et al. 2012, 2013) and disappears in the HS. For example, Shaposhnikov et al. (2007) observed the spectral transition in 2005 outburst of GRO J1655-40 from the LS-IS-VHS and simultaneously measured the QPOs frequencies from 0.8Hz to 17Hz with photon index changed from 1.35 to 2.1 and after that QPO disappeared in HS spectral state. Since, AGNs and quasars are scaled up version of microquasars, Therefore, QPO features are expected in AGNs but for much lower fundamental frequency and one observation has reported an ~ 1 hour X-ray periodicity in RE J1034+396 (Gierliński et al. 2008).

Interestingly, both these varieties i.e. microquasars and quasars exhibit relativistic, collimated bipolar outflows or jets. The terminal velocities of these jets may vary from mildly relativistic (26% of c SS433, Margon 1984), to a value comparable to the speed of light c (GRS 1915+105 or M87). Actual VLBA observations suggest these jets seem to originate only from a region very close to the central object few r_g to few$\times 10 r_g$ (Junor et al. 1999; Doeleman et al. 2012).As we have pointed above that the jets generated from these microquasars are morphologically similar to the quasar jets and have similar terminal speeds (M87, Biretta & Meisenheimer 1993; GRS1915+105 Mirabel & Rodríguez 1994), only a scaled down version in terms of size, e.g., AGN/Quasar jets are typically of sizes in the range of few kpc (kilo-parsec) to few$\times$100 kpc, but microquasar jets are a few pc to few $\times$10microquasar

Although, quasars and microquasars are having different physical sizes, masses and time scales but qualitatively they show similar properties. Since quasar and microquasar time scales depend on the mass of the central object, so microquasars vary much faster than the the quasars. For example, light crossing time of the Schwarzschild radius is $\tau_g = 2GM_B/c^3 = 10^{-5} M_B/M_\odot$microquasar So a microquasars minimum dynamical time scale is $\tau_g \sim 10^{-4}$microquasar a quasar with $10^8 M_\odot$ microquasars it is $\tau_g \sim 10^3$s. Therefore we observe the microquasars to change state in days, while quasars and AGNs remain at the same state for decades. So studying the evolution of microquasar spectral/jet states, might throw light on the expected evolution of AGNs.

The most famous and basic picture of the evolution of BHC in microquasars is represented by a 'Hardness-Intensity Diagram' (HID) in X-ray astronomy. Since the HID roughly resembles the English letter 'Q', it is also called as $Q-$ diagram fig.1.1. HID shows that out-bursting BHCs start from the left corner of bottom horizontal i.e., low luminosity branch, in other words, low hard state (LS). Then the source becomes gradually brighter but the spectral index is still hard, which in the 'Q' diagram means the right vertical branch. Then at upper right end, the spectrum starts to get softer although the brightness remains roughly the same. The microquasar continues its journey from IS to VHS and then to HS. This cycle is repeated over and over again, each object have its own duty cycle. For example GX 339-4 source duty cycle takes place over the course of about one year from LS-IS-VHS-HS-LS (Fender & Gallo 2014).The jet is also correlated with this evolution of spectral state changes, mild jets are observed at LS, as the luminosity increases keeping the spectral index hard to IS the jet strength

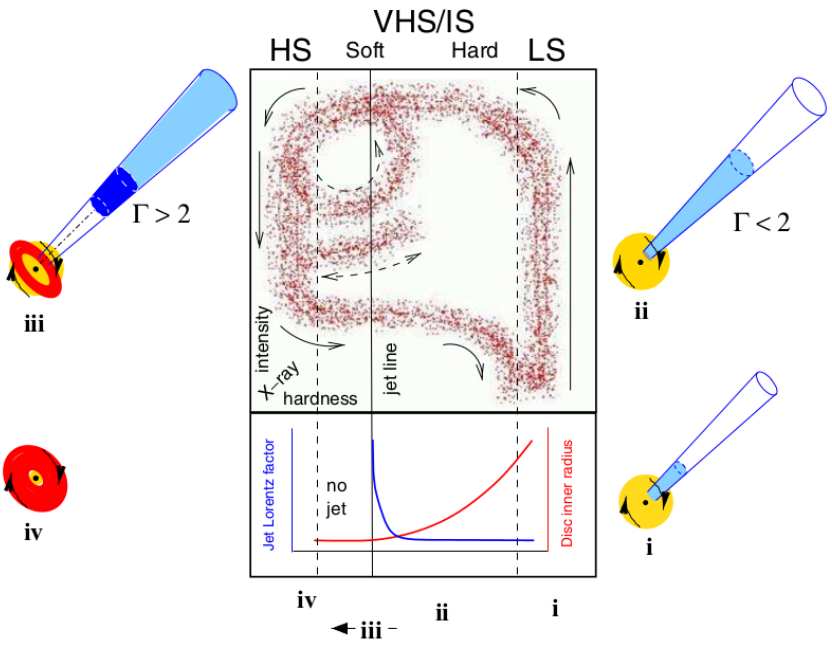

Figure 1.1: HID **or** $Q-$**diagram** - This is the simplified model example of jet-disc coupling in the BH-binary source, GRS 1915-105. Upper box represents the variation of $X-$ ray hardness-intensity diagram (HID) and corresponding variations in jet Lorentz factor (blue) with inner disc radius (red) are shown in lower box. HID is divided into the four part namely, 'low/hard state' LS-low state, 'hard or soft' VHS-very high state, transition(Fender et al. 2004).

increases too. And then during the transition of the source from IS to VHS there is ejection of relativistic jet. Once the source reaches HS no jet is observed. The QPO too follows a similar trend, i. e., mild QPOs are observed during LS, the frequency increases during the transition from LS → IS, and then it maximizes just before the transition from IS to VHS, and then disappears during HS. Viable accretion models should be able to generate the jets close to the compact object, and when this happens, the spectral state should be either in LS, IS and IS→VHS states. If the model can achieve this then the model should automatically correlate the physics, as well as, the dynamics of the hard X-ray emitting region with the evolution of QPO. And then may conjecture how this physics translate into observations as we go from X-ray binaries to the centers of active galaxies.

1.2 Theoretical models

Many theoretical models are proposed in literature to explain the observations from AGN/quasars to microquasars. It was understood that since black holes do not have intrinsic atmosphere, then the jet should originate from accreting matter itself. So whether to explain the generation of the spectra from these sources or to pinpoint the physics of jets, it is of utmost importance to understand the actual physics of accretion on to black holes.

Since black holes are super attractors, to the extent that the matter enters the event horizon with the speed of light, so the dynamics of the flow close to the horizon should be dominated by advection. Since the matter would start with negligible inward velocity at large distance form the black hole, but would enter the event horizon with the speed of light, so black hole accretion is essentially transonic (sub-sonic to super-sonic transition). Following these physical requirements, the first model proposed to explain black hole accretion was the relativistic radial accretion model by Michel (1972),which was basically the relativistic version of Bondi flow (Bondi 1952).Although this model of radial flow is compatible with the property of transonicity and have a dominant advection term, but being a radial flow it is too fast, so the accretion timescale is too small than cooling timescales to produce the luminosity observed (Shapiro 1973), and the computed luminosity from such an accretion model around a black hole could not explain the luminosities observed from microquasars and quasars.

1.2.1 Disc Theories

So rotating flows were contemplated, since the infall timescale would be long enough for the radiative processes to become active. Advective solutions of rotating matter onto a compact object described by the Newtonian potential in the inviscid limit gives closed topologies, i. e., multi-valued solutions in the shape of inverted-α and do not connect the compact object with large distances. This type of solution is meaningless because matter starting from large distance can not fall on to the surface of the compact object due to high centrifugal force, so reduction of angular momentum of the accreting matter is required. Therefore, a general accretion disc should have viscosity to remove the angular momentum.

The next model which became very popular is the standard disc, or the Keplerian disc or the Shakura-Sunyaev disc (Shakura & Sunyaev 1973, and the relativistic version by Novikov & Thorne 1973), which was constructed by keeping these problems in mind. Shakura & Sunyaev (1973), assumed that the viscosity is such that the angular-momentum at every radial distance has local Keplerian value. Since matter has angular momentum therefore the accreting matter would flatten in the form of a disc. They argued that since most of the matter will settle around the equatorial plane, so the disc should be optically thick. Now the radiations due to the heat generated by viscous dissipation would be lost and would attain locally black body distribution due to the interaction of the radiation in an optically thick medium. Shakura and Sunyaev assumed that the entire heat generated due to viscosity is lost in the process, and the disc would remain thin. They also assumed that the disc is chopped off at the location of the marginally stable orbit, or, $r_{ms}(= 3r_g$ for a non-rotating black hole). An open question still dogs the community, i. e., the nature of viscosity. It has been shown much earlier that ionic or molecular viscosity is too weak for tenuous astrophysical plasma and it would take about Hubble time for matter to reach the horizon from the outer edge of an accretion disc. They remained silent about the origin and tentatively proposed that the viscosity is anomalous and is proportional to the gas pressure. Remarkably, even with such simplifying and restrictive assumptions, this model have been successful in explaining the thermal part of a BHC spectrum. However, this model do not treat the pressure and advection terms in the conservation equations correctly, since the disc is terminated at the marginally stable orbit and no attempt was made to satisfy the

inner boundary condition on the horizon. A second problem arose when it was pointed out (Lightman & Eardley 1974) that the inner regions of these discs are viscously and thermally unstable. Along with these theoretical shortcoming, the Shakura-Sunyaev disc also failed to explain the non-thermal part of the BHCs spectrum.

To address the short coming of the thin accretion disc, many models were proposed, like thick accretion discs by Thorne & Price (1975) , or, the idea of thick accreting tori (Paczyńsky & Wiita 1980; Paczyński 1982; Rees et al. 1982) However, none of them correctly treated the advection term in the equations of motions, since all these models were predominantly rotating, although with sub-Keplerian angular momentum. Another model which got a wide attention was advection dominated accretion flow or ADAF (e.g., Ichimaru 1977; Narayan & Yi 1994, hereafter NY94). For simplicity, NY94 considered self similar flow around Newtonian gravitational potential, where the viscously dissipated energy is advected along the mass, momentum, and the entropy of the flow. The original ADAF solution was wholly subsonic, and therefore did not satisfy the inner boundary condition around a black hole. The global solution of ADAF, characterized by a wholly subsonic flow but becoming transonic through one sonic point near the horizon, showed that the flow actually becomes transonic at around few Schwarzschild radii (r_g), and the self-similarity may be maintained far away from the sonic point (Chen et al. 1997).

Simultaneously, there were some interesting research going on regarding sub-Keplerian flows around black holes. Liang & Thompson (1980) showed that multiple sonic points may exist for sub-Keplerian flows in a significant range of the energy-angular momentum parameter space. For such flows, shocks may form (Fukue 1987; Chakrabarti 1989). General global solutions in the advective domain incorporating viscosity and thermal effects were obtained by many independent researchers and ADAF solutions were shown to be a subset of the general advective solutions (Chakrabarti 1990, 1996; Lanzafame et al. 1998; Lu et al. 1999; Gu & Lu 2004). Since at the shock location various flow variables(e. g., matter velocity, sound speed and angular momentum etc) across the shock surface jump abruptly, marked change in cooling, heating, and other dissipation rates takes place. This may generate outflow or jets and may also render the shock unstable (Molteni et al. 1994, 1996a,b; Lanzafame et al. 1998; Chattopadhyay & Das 2007; Das & Chattopadhyay 2008; Becker et al. 2008; Das et al. 2009).

Although lot of investigation has been undertaken but many aspects of dissipative accretion disc, are still not fully understood. Simulations show presence of strong, weak or no jets even in presence of shocks. We would like to understand what are the regimes of strong and weak jets. We would like to investigate the feedback effect of failed jets on the accretion processes too. We propose to investigate theoretically and numerically to address these issues in presence of all kind of dissipative and cooling processes and how it affects the launching of the jet, and how to explain observations with these theoretical tools.

1.2.2 Aim of the thesis

We plan to undertake theoretical and numerical investigations of accretion disc starting with pseudo-Newtonian potential and then we would like address some issues in general theory of relativity too. In this study we would concentrate on all possible accretion solutions in presence of all possible dissipative processes, and how each accretion solution will be linked with various jet states. We would like to establish disc spectral states with actual dynamical states of black hole candidates. Moreover, due to the absence of continuous monitoring of the black hole candidates, relation between jet states, spectral states and the QPO states is not very clear from observations. We would like to find this relation theoretically and compare these relations with the observations.

1.2.3 Pseudo-Newtonian Potential

Since Newtonian gravity can not explain black hole accretion because its effective potential can not produce accretion solution, which connect the star's surface with infinity. So, we have to consider general relativistic effects. For this reason and simplicity, we have chosen pseudo-Newtonian potential for our study and it gives qualitatively similar results as in general theory of relativity such as the location of marginally stable orbit, the location of marginally bound orbit and the location of photon orbit and their corresponding angular momentum values. Moreover, expression of the Keplerian angular momentum distribution is same as in general relativity. So, the space-time geometry around a Schwarzschild black hole can be described by the pseudo-Newtonian potential, which is introduced by Paczyńsky & Wiita (1980). The expression of pseudo-Newtonian

potential is

$$\phi(r) = -\frac{GM_B}{x - r_g}. \tag{1.1}$$

This is also called as Paczyński-Wiita potential (or PW-potential). Schwarzschild radius of the black hole or $r_g = 2GM_B/c^2$. Here, G is the gravitational constant, M_B is the mass of black hole and c is the speed of light. In our study we have chosen geometrical unit system, where $2G = M_B = c = 1$ or $G = M_B = c = 1$, and have mentioned the same at appropriate places.

2

Governing equations and Assumptions

In this chapter we present the equations of motion governing fluid flow around black holes. Since black hole is an extremely relativistic object, one should employ general relativity to study fluid behaviour around it. However, as we have shown and is also well known that, one may gain valuable qualitative knowledge of matter behaviour around such objects by employing pseudo-Newtonian potential (detail in chapter 1) and one form of it, which is given by Paczyński-Wiita (1980). We have employed PW-potential to study non-rotating black holes. We have also re-calculated accretion-ejection solutions using general relativity, which apart from giving a more correct picture, also under-lines the inherent complications of a fully general relativistic treatment. Furthermore, we also present the analysis both in fixed Γ equation of state (EoS) and variable Γ EoS, where Γ is the adiabatic index. Here, we have divided this chapter into two sections, one, fluid equations with pseudo-Newtonian potential and other, with full general relativistic approach.

2.1 Pseudo-Newtonian approach:

For viscous fluids the conserved form of equations of motion (Landau & Lifshitz 1959; Choudhuri 1998) are written as,
Continuity equation

$$\frac{\partial \rho}{\partial t} + \frac{(\partial \rho v_i)}{\partial x_i} = 0, \tag{2.1}$$

Momentum balance equation

$$\frac{\partial}{\partial t}(\rho v_i) + \frac{\partial \Pi_{ik}}{\partial x_k} = \rho f_i, \tag{2.2}$$

and energy balance equation

$$\frac{\partial e_t}{\partial t} + \frac{\partial \mathcal{F}_k}{\partial x_k} = \rho v_k f_i, \tag{2.3}$$

where, $\Pi_{ik} = p\delta_{ik} + \rho v_i v_k - \sigma_{ik}$ is the generalized pressure tensor, which is also the flux of momentum density (ρv_i) for viscous fluid and ρ, v_i, p and f_i are density, velocity components, pressure and acceleration due to gravity, respectively. The terms $e_t = \rho(v^2/2+\epsilon)$ and $\mathcal{F}_k = \{\rho(v^2/2+h)v_k\} - \mathrm{v}.\sigma - K\nabla T$ are total energy density of the fluid and flux of total energy density due to transfer of the fluid mass, respectively. The term in curly bracket of $\mathcal{F}_k$ is the flux of energy density for ideal fluids. The second term $\mathrm{v}.\sigma$ is the flux of energy due to the process of internal friction or viscosity and third term $K\nabla T$ is due to heat conduction. Here, K and T are the coefficient of thermal conduction and temperature of the fluid, respectively. Enthalpy per unit mass (h) is defined as,

$$h = \epsilon + \frac{p}{\rho}, \tag{2.4}$$

here, ϵ is specific internal energy of the fluids. The first two terms of Π_{ik} represent the flux of bulk momentum and the flux of internal reversible momentum transfer of fluid particles i.e. due to fluid pressure, which are acting in the fluid. But if we study viscous fluid, which causes thermodynamic irreversibilities in the motion of the fluid. This irreversibility occurs due to internal friction (viscosity) and thermal conduction. So, for viscous fluid we have one more term σ_{ik} (viscous stress tensor) in addition to the flux of momentum density tensor, and is given by

$$\sigma_{ik} = \mu\left(\frac{\partial v_i}{\partial x_k} + \frac{\partial v_k}{\partial x_i} - \frac{2}{3}\delta_{ik}\frac{\partial v_l}{\partial x_l}\right) + \varsigma\delta_{ik}\frac{\partial v_l}{\partial x_l}. \tag{2.5}$$

The quantities μ and ς are functions of pressure and temperature and called as coefficient of dynamical viscosity and coefficient of bulk viscosity, respectively. Thus the equation of motion for the viscous fluid can be written by using equations (2.1, 2.2 and 2.5) as

$$\rho\left[\frac{\partial \mathbf{v}}{\partial t} + (\mathbf{v}.\overrightarrow{\nabla})\mathbf{v}\right] = \rho\mathbf{f} - \overrightarrow{\nabla}p + \mu\nabla^2\mathbf{v} + (\varsigma + \mu/3)\overrightarrow{\nabla}(\overrightarrow{\nabla}.\mathbf{v}). \tag{2.6}$$

This is called Navier-Stokes equation. If we assume, spatial variation of μ and ς to be negligible, then equation 2.6 can be also written as

$$\rho\frac{D\mathbf{v}}{Dt} = \rho\mathbf{f} - \overrightarrow{\nabla}p + \overrightarrow{\nabla}.\sigma, \tag{2.7}$$

where, $D/Dt = \partial/\partial t + \mathbf{v}.\overrightarrow{\nabla}$ is the total or Lagrangian time derivative and $\partial/\partial t$ is partial or Eulerian time derivative. By using equations 2.1 and 2.2 with scalar product of v_k , the energy equation 2.3 can be written as,

$$K\overrightarrow{\nabla}.(\overrightarrow{\nabla}T) + \rho\left[\frac{D\epsilon}{Dt} + p\frac{D}{Dt}\left(\frac{1}{\rho}\right)\right] - \sigma_{ik}\frac{\partial v_k}{\partial x_i} = 0. \tag{2.8}$$

First law of thermodynamic is defined as,

$$T\frac{Ds}{Dt} = \frac{D\epsilon}{Dt} + p\frac{D}{Dt}\left(\frac{1}{\rho}\right), \tag{2.9}$$

where, s is entropy per unit mass of the gas. Now, equation (2.8) can be written in form of the entropy equation,

$$\rho T\frac{Ds}{Dt} = \sigma_{ik}\frac{\partial v_i}{\partial x_k} - K\overrightarrow{\nabla}.(\overrightarrow{\nabla}T). \tag{2.10}$$

Since, viscous stress tensor is symmetric and traceless ($trace(\sigma_{ik}) = 0$), so $trace(\sigma_{ik}\delta_{ik})$ is also zero, then the last term of energy equation (2.8) becomes as $\sigma_{ik}\frac{\partial v_i}{\partial x_k} = (\sigma_{ik})^2/(2\mu)$.

Equations of motion in cylindrical coordinates: Accreting fluid has a tendency to settle in the form of a disc due to angular momentum and forms an axis-symmetry system. Therefore, we have expressed the fluid equations in cylindrical geometry (x, ϕ, z). The components of the viscous tensor (2.5) are

$$\begin{aligned}
&\sigma_{xx} = 2\mu\left(\frac{\partial v_x}{\partial x} - \frac{1}{3}(\overrightarrow{\nabla}.\mathbf{v})\right) + \zeta\ \overrightarrow{\nabla}.\mathbf{v}, \qquad \sigma_{x\phi} = \mu\left(\frac{1}{x}\frac{\partial v_x}{\partial \phi} + \frac{\partial v_\phi}{\partial x} - \frac{v_\phi}{x}\right),\\
&\sigma_{\phi\phi} = 2\mu\left(\frac{1}{x}\frac{\partial v_\phi}{\partial \phi} + \frac{v_x}{x} - \frac{1}{3}(\overrightarrow{\nabla}.\mathbf{v})\right) + \zeta\ \overrightarrow{\nabla}.\mathbf{v}, \quad \sigma_{\phi z} = \mu\left(\frac{\partial v_\phi}{\partial z} + \frac{1}{x}\frac{\partial v_z}{\partial \phi}\right),\\
&\sigma_{zz} = 2\mu\left(\frac{\partial v_z}{\partial z} - \frac{1}{3}(\overrightarrow{\nabla}.\mathbf{v})\right) + \zeta\ \overrightarrow{\nabla}.\mathbf{v} \qquad \text{and} \qquad \sigma_{zx} = \mu\left(\frac{\partial v_z}{\partial x} + \frac{\partial v_x}{\partial z}\right)
\end{aligned} \tag{2.11}$$

where, $\overrightarrow{\nabla}.\mathbf{v} = \frac{\partial(xv_x)}{x\partial x} + \frac{\partial v_\phi}{x\partial \phi} + \frac{\partial v_z}{\partial z}$.

The components of Navier-Stokes equation (2.7) are,

$x-$ component

$$\frac{\partial v_x}{\partial t} + (\mathbf{v}.\overrightarrow{\nabla})v_x - \frac{v_\phi^2}{x} = f_x - \frac{1}{\rho}\frac{\partial p}{\partial x} + \frac{1}{x}\frac{\partial}{\partial x}(x\sigma_{xx}) + \frac{1}{x}\frac{\partial \sigma_{x\phi}}{\partial \phi} + \frac{\partial \sigma_{zx}}{\partial z} - \frac{\sigma_{\phi\phi}}{x},$$

$\phi-$ component

$$\frac{\partial v_\phi}{\partial t} + (\mathbf{v}.\overrightarrow{\nabla})v_\phi + \frac{v_x v_\phi}{x} = f_\phi - \frac{1}{\rho x}\frac{\partial p}{\partial \phi} + \frac{1}{x}\frac{\partial}{\partial x}(x\sigma_{x\phi}) + \frac{1}{x}\frac{\partial \sigma_{\phi\phi}}{\partial \phi} + \frac{\partial \sigma_{z\phi}}{\partial z} + \frac{\sigma_{x\phi}}{x},$$

and $z-$ component

$$\frac{\partial v_z}{\partial t} + (\mathbf{v}.\overrightarrow{\nabla})v_z = f_z - \frac{1}{\rho}\frac{\partial p}{\partial z} + \frac{1}{x}\frac{\partial}{\partial x}(x\sigma_{xz}) + \frac{1}{x}\frac{\partial \sigma_{z\phi}}{\partial \phi} + \frac{\partial \sigma_{zz}}{\partial z}. \tag{2.12}$$

The continuity equation is,

$$\frac{\partial \rho}{\partial t} + \left[\frac{1}{x}\frac{\partial(\rho x v_x)}{\partial x} + \frac{1}{x}\frac{\partial(\rho v_\phi)}{\partial \phi} + \frac{\partial(\rho v_z)}{\partial z}\right] = 0. \tag{2.13}$$

2.1.1 Equations of motion for accretion disc

Since, we are considering rotating accretion disc in steady, axis-symmetric and vertically in hydro-static equilibrium $\left(i.e.\ \frac{\partial}{\partial t} = \frac{\partial}{\partial \phi} = 0 \text{ and } v_z = 0\right)$, assumptions, so for simplicity we have ignored all the components of viscous tensor except $\sigma_{x\phi}$ and the heat conduction, then equations 2.12, 2.13 and 2.10 are written as

x-component or radial momentum flux equation,

$$v\frac{dv}{dx} + \frac{1}{\rho}\frac{dp}{dx} + \frac{\lambda^2}{2x^3} - f_x = 0 \tag{2.14}$$

ϕ-component or azimuthal momentum flux equation,

$$\Sigma v x \frac{d\lambda}{dx} + \frac{d(x^2 W_{x\phi})}{dx} = 0 \tag{2.15}$$

z-component in vertical hydro-static equilibrium, so it gives local half height of the disc,

$$\frac{1}{\rho}\frac{dp}{dz} = f_z, \Longrightarrow \qquad H = \sqrt{\frac{2px}{\rho}}\,(x-1) \tag{2.16}$$

Continuity equation is

$$\frac{1}{x}\frac{\partial(\Sigma x v)}{\partial x} = 0, \Longrightarrow \quad \dot{M} = 2\pi\Sigma x v. \tag{2.17}$$

Energy generation equation is

$$\Sigma v T \frac{ds}{dx} = Q^+ - Q^-, \tag{2.18}$$

where, $\Sigma = 2\rho H$ and $W_{x\phi} = 2H\sigma_{x\phi} = \Lambda x(\partial\Omega/\partial x)$(Frank et al. 1985) are vertically integrated specific surface density and viscous shear tensor, respectively. The dynamical viscosity parameter $\Lambda = \Sigma\nu = \Sigma(\alpha a^2)/(\Gamma\Omega_K)$, where, ν, α, a and Ω_K are the kinematic viscosity parameter, Shakura-Sunyaev viscosity parameter, sound speed and the Keplerian angular velocity, respectively. Moreover, $\lambda = xv_\phi$ and $\Omega = v_\phi/x$ are the specific angular momentum and the angular velocity of the fluid, respectively. It may be noted, $Q^+ = (W_{x\phi})^2/(2\Lambda)$ and Q^- are viscous heating and radiative cooling terms, respectively. Here, $f_x = -d\phi/dx = -0.5/(x-1)^2$ is pseudo-Newtonian gravitational force in the radial direction.

Integrating eq. (2.14) with respect to the radial distance (x), we get constant of motion (ε) and that is

$$\frac{v^2}{2} + \int \frac{dp}{\rho} - \int \frac{\lambda^2}{x^3}dx - \frac{1}{2(x-1)} = \varepsilon. \tag{2.19}$$

By using eqs. (2.4, 2.9, 2.18 and integral form of eq. 2.15), the term $\int dp/\rho$ can be written as

$$\int \frac{dp}{\rho} = h - \int (\lambda - \lambda_0)d\Omega - \int \frac{Q^-}{\Sigma v}dx. \tag{2.20}$$

By using $\lambda = x^2\Omega$, the term $\int(\lambda^2/x^3)dx$ can be rewritten as

$$\int \frac{\lambda^2}{x^3}dx = -\frac{\lambda^2}{2x^2} + \int (2\Omega^2 x dx + \Omega x^2 d\Omega) \tag{2.21}$$

Now, replacing second and third terms of eq. (2.19) by eqs. (2.20), (2.21) and after doing some algebra, we get

$$\varepsilon = \frac{v^2}{2} + h - \frac{\lambda^2}{2x^2} + \frac{\lambda\lambda_0}{x^2} - \zeta - \frac{1}{2(x-1)}, \tag{2.22}$$

where, $\zeta = \int \frac{Q^-}{\Sigma v}dx$. Here ε is a constant of motion in presence of viscosity and cooling and we call it the generalized Bernoulli constant (Kumar & Chattopadhyay 2014). Let us denote, $h = h_{nr}$ or $h = h_r$ are enthalpy for polytropic and relativistic EoS, respectively. If we ignore cooling processes in the equation (2.18), equation (2.22) becomes,

$$E = \frac{v^2}{2} + h - \frac{\lambda^2}{2x^2} + \frac{\lambda\lambda_0}{x^2} - \frac{1}{2(x-1)}, \tag{2.23}$$

This is known as grand specific energy of the flow (Gu & Lu 2004; Kumar & Chattopadhyay 2013; Chattopadhyay & Kumar 2013) and is a constant of motion in presence of

viscosity but not in presence of radiative cooling. Now, if we ignore all dissipative processes in the flow, we get

$$\mathcal{E} = \frac{v^2}{2} + h + \frac{\lambda^2}{2x^2} - \frac{1}{2(x-1)}, \tag{2.24}$$

which is the canonical definition of Bernoulli parameter and it is a constant of motion for non-dissipative flows or ideal fluid flows.

2.1.2 Shock equations:

Astrophysical fluids can become supersonic, being compressible and may harbour shock waves. The shock conditions are obtained from conservation of mass, momentum and energy fluxes across the discontinuity (Landau & Lifshitz 1959).The general, compact, and conserved form of the fluid equations (2.1 - 2.3) are,

$$\partial_t(q) + \partial_x(F_q) = 0, \tag{2.25}$$

where, q's are the conserved quantities and F_q are corresponding fluxes. We now impose the conditions that is $v_z = 0$, $\partial/\partial\phi = \partial/\partial z = 0$, stationary shocks and $\sigma_{x\phi} \neq 0$. Assuming hydro-static balance in the vertical direction we obtained the integrated form of the mass flux ($F_{\rm mass}$), the radial momentum flux ($F_{x-{\rm mom}}$), the azimuthal momentum flux ($F_{\phi-{\rm mom}}$), and the energy flux ($F_{\rm energy}$) in the radial direction, and are given by,

$$F_{\rm mass} = \dot{M},\ F_{x-{\rm mom}} = (W + \Sigma v^2),\ F_{\phi-{\rm mom}} = \dot{J} = \dot{M}\lambda + x^2 W_{x\phi} \text{ and } F_{\rm energy} = \dot{M}(\varepsilon - \Phi), \tag{2.26}$$

where, Φ is the gravitational potential. It is quite interesting to see that the mass flux along the radial direction is $\dot{M}$, the momentum flux in the radial direction is the sum of the thermal pressure and the ram pressure, in the azimuthal direction the momentum flux is $\dot{J}$ or the angular momentum flux, and the energy flux is related to the generalized Bernoulli parameter ε. After some straight forward algebra, we find the generalized version of non-dissipative shock condition in presence of viscosity and cooling, and is given by

$$\dot{M}_+ = \dot{M}_-, \tag{2.27}$$

$$W_+ + \Sigma_+ v_+^2 = W_- + \Sigma_- v_-^2, \tag{2.28}$$

$$\dot{J}_+ = \dot{J}_-, \tag{2.29}$$

and

$$\varepsilon_+ = \varepsilon_-, \tag{2.30}$$

In presence of massloss, condition 2.27 is modified as,

$$\dot{M}_+ = \dot{M}_- - \dot{M}_{out} = \dot{M}_-(1 - R_{\dot{m}}). \tag{2.31}$$

where subscripts minus(-) and plus(+) denote the quantities of supersonic and subsonic branches across the shock in the black hole accretion flow, respectively. The equation (2.30) can be changed according to types of shock in the accretion flow such as
for dissipative shock

$$\varepsilon_+ = \varepsilon_- - \triangle\varepsilon, \tag{2.32}$$

where, $\triangle\varepsilon = f_e(h - h)$ is thermal dissipation energy at the shock front. Here, f_e is fraction of the difference in thermal energy generation across the shock transition.
For Isentropic shock:- The condition 2.30 is replacing by conserving entropy across the shock front,

$$\mathcal{K}_+ = \mathcal{K}_-. \tag{2.33}$$

Here, energy dissipation is change in the energy parameter across the shock transition i.e. $\triangle\varepsilon = \varepsilon_- - \varepsilon_+$.
In the inviscid and adiabatic limit, if we put $\alpha = Q^- = 0$, we retrieve the original Rankine-Hugoniot shock conditions, i.e. equation (2.29) is redundant and equation (2.30) reduces to the conservation of the canonical Bernoulli parameter ($\mathcal{E}$) across the shock (Landau & Lifshitz 1959; Chakrabarti 1989) . In literature, various authors have used various forms of shock conditions for viscous flow. The shocked disc solution with viscosity was obtained by Chakrabarti (1996) and later by (Gu & Lu 2004; Das 2007; Chattopadhyay & Das 2007; Das & Chattopadhyay 2008) by choosing the viscous stress to be proportional to the total pressure, which made equation (2.29) redundant. Becker et al. (2008)on the other hand, used isothermal condition instead of equation (2.30). In Kumar & Chattopadhyay (2013) and Kumar et al. (2014) cooling was ignored, so equation (2.30) was replaced by the conservation of E across the shock front. Since, equations (2.27-2.30) do not depend explicitly on the form of h, and viscosity and cooling processes have been considered, therefore this form of shock condition is the most

general form of Rankine-Hugoniot type shock conditions obtained by strict conservation of fluxes of the equations of motion by following the prescription laid down by Landau & Lifshitz (1959).

Using equations (2.27-2.30), the supersonic branch radial velocity, temperature, and the angular momentum can be obtained from the post-shock quantities and vice versa.

2.1.3 Jet geometry and jet equations of motion:

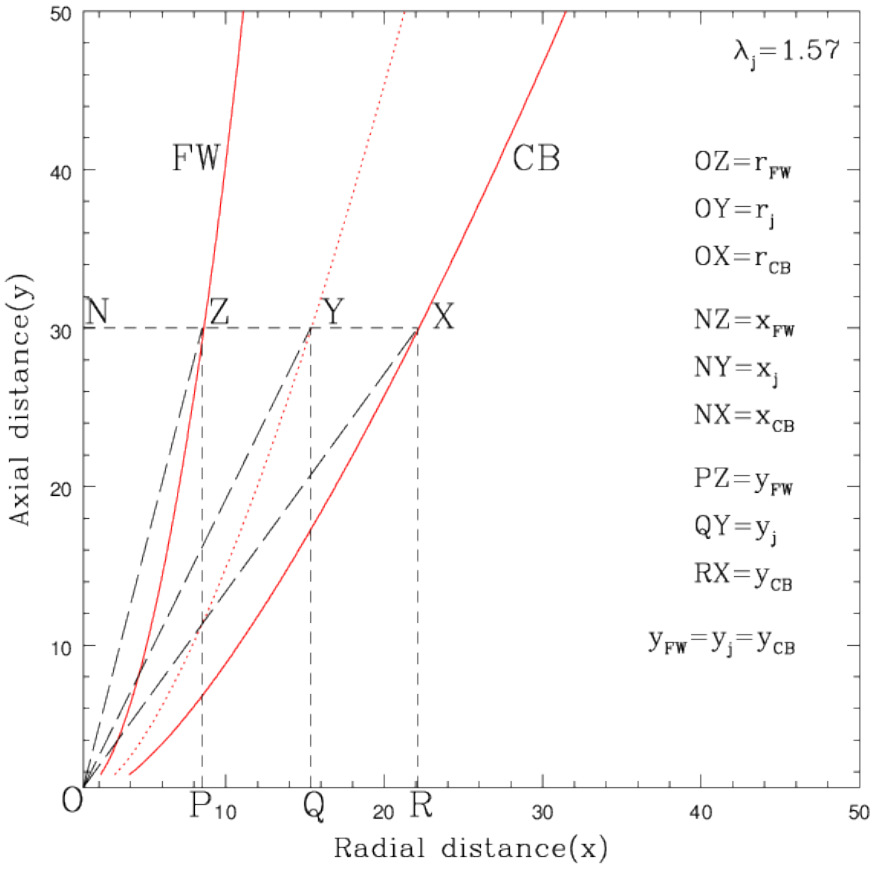

Figure 2.1: Jet geometry - geometry for rotating outflow along axis and between funnel wall (FW) and centrifugal barrier (CB).

Simulations (Molteni et al. 1996a)have shown that extra thermal gradient force along the vertical direction, drives bipolar outflows, therefore the outflow and the accretion solution is connected by the shock. As has been suggested by Molteni et al.

(1996a)and is described in details by Chattopadhyay & Das (2007); Kumar & Chattopadhyay (2013) and Kumar et al. (2014) the outflowing matter tend to move out through the region between the funnel wall (FW) and the centrifugal barrier (CB) as shown in Fig.2.1. The cylindrical radius of the CB is,

$$x_{CB} = [2\lambda^2 r_{CB}(r_{CB}-1)^2]^{\frac{1}{4}}, \tag{2.34}$$

and that of FW is,

$$x_{FW}^2 = \lambda^2 \frac{(\lambda^2-2) + \sqrt{(\lambda^2-2) - 4(1-y_{CB}^2)}}{2}, \tag{2.35}$$

where, the spherical radius of CB is $r_{CB} = \left(x_{CB}^2 + y_{CB}^2\right)^{1/2}$, while y_{CB} is the local height of CB. The streamline is computed as, $r_j = \sqrt{x_j^2 + y_j^2}$, where $x_j = (x_{FW} + x_{CB})/2$, and $y_j = y_{FW} = y_{CB}$ i.e. at every r_j the direction of jet flow is along the tangent to the curve streamline. The cross-sectional area of the jet is defined as,

$$\mathcal{A} = \frac{2\pi(x_{CB}^2 - x_{FW}^2)}{\sqrt{1+(dx_j/dy_j)^2}}. \tag{2.36}$$

Implementing the assumptions of axisymmetry, steady state motion along the tangent to the direction $\hat{e}_{r_j} = \vec{r}_j/|\vec{r}_j|$ onto fluid equations (2.10 - 2.13), we obtain the jet equations. The momentum balance equation along the jet stream line is given by

$$v_j \frac{dv_j}{dr} + \frac{1}{\rho_j}\frac{dp_j}{dr} - \frac{\lambda_j^2}{x_j^3}\frac{dx_j}{dr} + \frac{1}{2(r_j-1)^2}\frac{dr_j}{dr} = R_f, \tag{2.37}$$

Here the derivative is with respect to $r = r_{CB}$. Suffix 'j' denotes jet quantities and the term R_f represents the radiative forces due to radiation, which are coming from the disc. The integrated continuity equation along the jet stream line is given by

$$\dot{M}_{out} = \rho_j v_j \mathcal{A} \tag{2.38}$$

This integration constant is called as mass flux which is moving along the stream line of the jet. The entropy equation is written as,

$$\frac{d\epsilon_j}{dr} + p\frac{d}{dx_j}\left(\frac{1}{\rho_j}\right) = 0 \tag{2.39}$$

If $R_f = 0$, then equation (2.37) can be integrated with the help of equations (2.4) and (2.39) then it gives the Bernoulli parameter for jet,

$$\mathcal{E}_j = \frac{v_j^2}{2} + h_j + \frac{\lambda_j^2}{2x_j^2} - \frac{1}{2(r_j-1)} \tag{2.40}$$

where $\mathcal{E}_j$ is specific energy and h_j is enthalpy for the jet.

2.2 General Relativistic approach:

We have studied accretion onto black holes by using pseudo-Newtonian approach and that gives reasonability good result. Since black holes are relativistic objects, so we also want to study the same by employing correct general relativistic equations and relativistic EoS. In this study, we have used Schwarzchild metric around black holes in cylindrical coordinates, that is

$$ds^2 = g_{tt}dt^2 + g_{rr}dr^2 + g_{\phi\phi}d\phi^2 + dz^2, \tag{2.41}$$

where, $g_{tt} = -(1-2/r),\ g_{rr} = 1/(1-2/r),\ g_{\phi\phi} = r^2$ and $g_{zz} = 1$ are metric components. The energy-momentum tensor for viscous flow

$$T^{\delta\beta} = (e+p)u^{\delta}u^{\beta} + pg^{\delta\beta} + t^{\delta\beta}, \tag{2.42}$$

where, e and p are the energy density and gas pressure (measured in local frame), respectively. u^{μ} and $g^{\mu\nu}$ are four-velocities and metric components. Here the viscous stress tensor is $t^{\delta\beta} = -\zeta\Theta_{\rm exp}h^{\delta\beta} - 2\mu\sigma^{\delta\beta}$, where, ζ and μ are bulk and shear viscosity coefficients. We assume the viscosity is generated only by shear and therefore $\zeta = 0$. The shear tensor has the general form

$$\sigma_{\delta\beta} = \frac{1}{2}(u_{\delta;\gamma}h^{\gamma}_{\beta} + u_{\beta;\gamma}h^{\gamma}_{\delta}) - \frac{1}{3}\Theta_{\rm exp}h_{\delta\beta}, \tag{2.43}$$

where, $h_{\gamma\beta} = \delta_{\gamma\beta} + u_{\gamma}u_{\beta}$ is the projection tensor, $\delta_{\gamma\beta}$ is Kronecker delta and $\Theta_{\rm exp} = u^{\gamma}_{;\gamma}$ is expansion of fluid world line. Now equation (2.43) can be written as,

$$\sigma_{\delta\beta} = \frac{1}{2}(u_{\delta;\beta} + u_{\beta;\delta} + a_{\delta}u_{\beta} + a_{\beta}u_{\delta}) - \frac{1}{3}\Theta_{\rm exp}h_{\delta\beta}, \tag{2.44}$$

where, $a_{\delta} = u_{\delta;\gamma}u^{\gamma}$ is the four-acceleration. The co-variant derivative of four-velocity is defined as $u_{\beta;\gamma} = u_{\beta,\gamma} - \Gamma^{\delta}_{\beta\gamma}u_{\delta}$, where $\Gamma^{\delta}_{\beta\gamma} = g^{\delta\chi}(g_{\chi\beta,\gamma} + g_{\chi\gamma,\beta} - g_{\beta\gamma,\chi})/2$ is Christoffel symbol.

The governing equations of relativistic fluid are energy-momentum conservation and baryon number conservation given by,

$$T^{\delta\beta}_{;\beta} = 0;\ (nu^{\beta})_{;\beta} = 0. \tag{2.45}$$

The relativistic Navier-Stokes equation is obtained by projecting the energy momentum conservation along some spatial direction i. e., $h^{i}_{\delta}T^{\delta\beta}_{;\beta} = 0$ and can be written as

$$[(e+p)u^{\beta}u^{i}_{;\beta} + (g^{i\beta} + u^{i}u^{\beta})p_{,\beta}] + h^{i}_{\delta}t^{\delta\beta}_{;\beta} = 0, \tag{2.46}$$

The energy generation equation, $u_\delta T^{\delta\beta}_{;\beta} = 0$ and is given by,

$$u^\delta \left[\left(\frac{e+p}{n} \right) n_{,\delta} - e_{,\delta} \right] = Q^+, \tag{2.47}$$

where, $Q^+ = t^{\delta\beta}\sigma_{\delta\beta}$ is the heating term and for the time being we are ignoring the cooling term.

We have assumed the accretion flow to be in steady state, axis-symmetric and in vertical hydro-static equilibrium. Since the relativistic shear is very very complicated, we have only considered the $r-\phi$ component of the shear tensor. This would on one hand simplify the equations tremendously, on the other would allow us for direct analogy with the plethora of work done with pseudo potentials. With these assumptions we write down the radial component of relativistic Navier-Stokes equation ($h^r_\delta T^{\delta\beta}_{;\beta} = 0$),

$$u^r \frac{du^r}{dr} + \frac{1}{r^2} - (r-3)u^\phi u^\phi + \left(1 - \frac{2}{r} + u^r u^r \right) \frac{1}{e+p} \frac{dp}{dr} = 0, \tag{2.48}$$

the integrated version of the azimuthal component equation ($h^\phi_\delta T^{\delta\beta}_{;\beta} = 0$),

$$-\rho u^r (L - L_0) = 2\mu\sigma^r_\phi, \tag{2.49}$$

and z-component equation taking in vertical hydro-static equilibrium, it gives local disc half height expression (Riffert & Herold 1995; Peitz & Appl 1997),

$$H = \sqrt{\frac{2\Theta r^3}{\tilde{t}\gamma^2_\phi}}. \tag{2.50}$$

Now, integrating mass-conservation equation, which gives mass flux expression as,

$$-\dot{M} = 4\pi\rho H u^r r. \tag{2.51}$$

Here, $L = hu_\phi = hl$ and L_0 are the local bulk angular momentum and bulk angular momentum at the horizon of black hole, respectively. HereL_0 is the integration constant, and is the value of angular momentum where the viscous stress goes to zero. Here, the viscous stress tensor takes the form as $t^{r\phi} = -2\mu\sigma^{r\phi}$, where, μ is shear viscosity coefficient, defined as $\mu = \rho\nu$, $\nu = \alpha a r f_c$, and $f_c = (1-v^2)^2$. Since $\sigma_{r\phi}$ may or may not be equal to zero on the horizon, with the choice of f_c we have made $t^{r\phi}|_{\text{horizon}} = 0$. We are assuming only $r-\phi$ component of viscous shear tensor and it is written as (Peitz & Appl 1997),

$$2\sigma^\phi_r = u^r_{;\phi} + g^{rr}u_{\phi;r} + a^r u_\phi + a_\phi u^r - \frac{2}{3}\Theta_{\text{exp}} u^r u_\phi \tag{2.52}$$

Considering spatial derivative of radial four-velocity and expansion of the fluid is negligible so, the eq.(2.52) becomes,

$$2\sigma^r_\phi = g^{rr}\gamma_v^2\frac{dl}{dr} - \frac{2l}{r}g^{rr}. \tag{2.53}$$

In our study, we have used this form of viscous shear tensor. Here γ_v is bulk Lorentz factor.

The constant of motion can be obtained by integrating equation (2.48), we get,

$$log(E) = -\frac{1}{2}log(1-v^2) + \frac{1}{2}log(1-\frac{2}{r}) - \int\frac{(r-3)l^2}{r^3(r-2)\gamma_v^2}dr + \int\frac{1}{e+p}dp. \tag{2.54}$$

The last term of equation (2.54) with the help of equations (2.4) and (2.47) with assuming $Q^- = 0$ can be written as

$$\int\frac{1}{e+p}dp = \int\frac{1}{h}\frac{dp}{\rho} = \int\frac{1}{h}[dh - \frac{t^{r\phi}\sigma_{r\phi}}{\rho u^r}dr]. \tag{2.55}$$

Using equation (2.49) and relation $t^{r\phi} = -2\mu\sigma^{r\phi}$ in equation (2.55) with some algebra, we get,

$$\int\frac{1}{e+p}dp = \int\frac{1}{h}\left[dh + \frac{u^r(L-L_0)^2}{2\nu r(r-2)}dr\right]. \tag{2.56}$$

Combining equation (2.56) in equation (2.54) and re-arranging, we get,

$$E = \frac{h\gamma_v\sqrt{1-\frac{2}{r}}}{\exp(X_f)}, \tag{2.57}$$

where, $X_f = \int[(\frac{r-3}{r-2})\frac{l^2}{r^3\gamma_v^2} - \frac{u^r(L-L_0)^2}{2\nu hr(r-2)}]dr$. E is constant of motion in presence of viscous dissipation.

2.3 Equation of state (EoS):

Fluid equations have five independent components (equations 2.1 - 2.3), but has six variables (ρ, v_i, e and p). Therefore to solve fluid equations we need a closure relation. This closure relation between e, p and ρ is called EoS of gas.

Polytropic EoS: From kinetic theory of gases, one may compute the average energy density of non-relativistic particles obeying Maxwell-Boltzmann statistics, the general expression for the internal energy of a perfect gas is written as

$$e = \frac{p}{(\Gamma-1)}, \quad \text{and specific energy density,} \quad \epsilon = \frac{e}{\rho} = \frac{p}{\rho(\Gamma-1)} \tag{2.58}$$

Here, $\Gamma = c_p/c_v$ is adiabatic index, which is the ratio between two specific heats at constant pressure to constant volume of gas. Considering adiabatic gas flow ($ds = 0$), from equations (2.58) and (2.9), it is easily shown that

$$p = k\rho^{\Gamma}. \tag{2.59}$$

where k is constant of entropy. This is known as polytropic equation of state. Enthalpy per unit mass is defined as

$$h = \epsilon + \frac{p}{\rho} = \frac{\Gamma p}{\rho(\Gamma - 1)}. \tag{2.60}$$

The adiabatic sound speed is defined as

$$a^2 = \frac{dp}{d\rho} = \frac{\Gamma p}{\rho} \tag{2.61}$$

Using equation (2.59) in (2.17), we obtain expression for entropy accretion rate for the accretion disc

$$\dot{\mathcal{M}} = a^{2n} H x v, \tag{2.62}$$

and using 2.59 and 2.38 then we get entropy outflow rate for bipolar jets

$$\dot{\mathcal{M}}_{out} = a_j^{2n} v_j \mathcal{A}. \tag{2.63}$$

For adiabatic flow, $\dot{\mathcal{M}}$ and $\dot{\mathcal{M}}_{out}$ are constant along streamline. Its significance can be understood in the next chapter.

Relativistic EoS: Following Chattopadhyay (2008) and Chattopadhyay & Ryu (2009), we consider flows which are composed of electrons (e^-), positrons (e^+) and protons (p^+) of varying proportions, but always maintaining the overall charge neutrality. The number density is given by,

$$n = \Sigma_i n_i = n_{e^-} + n_{e^+} + n_{p^+}, \tag{2.64}$$

where, n_{e^-}, n_{e^+} and n_{p^+} are the electron, positron and proton number densities, respectively. Charge neutrality condition over a reasonable volume element demands that

$$n_{e^-} = n_{e^+} + n_{p^+}, \tag{2.65}$$

which implies,

$$n = 2n_{e^-}, \text{ and } n_{e^+} = n_{e^-}(1 - \xi), \tag{2.66}$$

where $\xi = n_{p^+}/n_{e^-}$ is the relative proportion of protons. The mass density is given by

$$\rho = \Sigma_i n_i m_i = n_{e^-} m_{e^-} \left[2 - \xi(1 - 1/\eta)\right], \tag{2.67}$$

where, $\eta = m_{e^-}/m_{p^+}$, and m_{e^-} and m_{p^+} are the electron and proton masses, respectively. For single temperature flows, the isotropic pressure is given by

$$p = \Sigma_i p_i = 2 n_{e^-} kT = 2 n_{e^-} m_{e^-} c^2 \Theta. \tag{2.68}$$

The EoS for multi-species flow is (Chattopadhyay 2008; Chattopadhyay & Ryu 2009),

$$e = \Sigma_i e_i = \Sigma \left[n_i m_i c^2 + p_i \left(\frac{9p_i + 3 n_i m_i c^2}{3p_i + 2 n_i m_i c^2} \right) \right]. \tag{2.69}$$

The non-dimensional temperature is defined with respect to the electron rest mass energy, $\Theta = kT/(m_{e^-} c^2)$. Using equations (2.64)-(2.68), the expression of the energy density in equation (2.69) simplifies to,

$$e = n_{e^-} m_{e^-} c^2 f = \rho_{e^-} c^2 f = \frac{\rho c^2 f}{[2 - \xi(1 - 1/\eta)]}, \tag{2.70}$$

where,

$$f = (2 - \xi) \left[1 + \Theta \left(\frac{9\Theta + 3}{3\Theta + 2} \right) \right] + \xi \left[\frac{1}{\eta} + \Theta \left(\frac{9\Theta + 3/\eta}{3\Theta + 2/\eta} \right) \right].$$

This is relativistic equation of state for multispecies gas flow. It is an approximation but is very accurate to the actual EoS for relativistic Maxwell-Boltzmann gas (see Chandrasekhar 1939 and Ryu et al. 2006 for further explanation).

The enthalpy is given by,

$$h = \frac{(e + p)}{\rho} = \frac{f c^2}{\tilde{t}} + \frac{2 c^2 \Theta}{\tilde{t}}, \tag{2.71}$$

where, $\tilde{t} = [2 - \xi(1 - 1/\eta)]$.

The expression of the polytropic index is given by,

$$N = \frac{1}{2} \frac{df}{d\Theta}. \tag{2.72}$$

The adiabatic index is

$$\Gamma = 1 + \frac{1}{N}. \tag{2.73}$$

Integrating of first law of thermodynamics (2.18, 2.47) by assuming adiabatic flow and using equation 2.70, it can be shown by Kumar et al. (2013); Chattopadhyay & Kumar (2013)that is

$$\rho = \mathcal{K}\ \exp(k_3)\ \Theta^{3/2}(3\Theta+2)^{k_1}(3\Theta+2/\eta)^{k_2}, \tag{2.74}$$

where, $k_1 = 3(2-\xi)/4, k_2 = 3\xi/4$, and $k_3 = (f-\tilde{t})/(2\Theta)$. This is the adiabatic equation of state for multispecies flows, where $\mathcal{K}$ is the constant of entropy. Combining equations (2.74) and (2.17), we get the expression of entropy accretion rate,

$$\dot{\mathcal{M}} = \frac{\dot{M}}{4\pi\mathcal{K}} = \exp(k_3)\Theta^{3/2}(3\Theta+2)^{k_1}(3\Theta+2/\eta)^{k_2}Hxv. \tag{2.75}$$

And combining equations (2.74) with (2.38), we get entropy outflow rate,

$$\dot{\mathcal{M}}_{out} = \frac{\dot{M}_{out}}{2\pi\mathcal{K}} = \exp(k_3)\Theta_j^{3/2}(3\Theta_j+2)^{k_1}(3\Theta_j+2/\eta)^{k_2}v_j\frac{\mathcal{A}}{2\pi}, \tag{2.76}$$

for relativistic flows.

3

Accretion-Ejection in pseudo - Newtonian description

This chapter, we have divided into two parts on the basis of solution methodology, one with study of accretion-ejection analytically and other with numerical simulation with polytropic EoS or fixed Γ in PW-potential around BHs. In next section, we presented viscous fluid and jet equations, then solution procedure and methodology in the section (3.2). In the section (3.3) we investigated various type of accretion solutions with different boundary conditions and full accretion-ejection solutions with raditively driven outflow presented in the section (3.4). In the last section (3.5) we presented time dependent viscous accretion solutions in 2-dimensional cylindrical geometry.

3.1 Fluid equations with fixed Γ

In this section, we have solved viscous fluid equations (2.14 - 2.18) applicable to accretion with fixed Γ equation of state (EoS) (2.58) by following the methodology described below.

Differential form of accretion equations:- Simplifying the equations (2.14 - 2.18) with the help of EoS (2.58) and by ignoring cooling Q^- in this section, we get spatial derivatives of fluid variables (v, a and λ) as gradient of fluid bulk velocity,

$$\frac{dv}{dx} = \frac{\left(\frac{2}{\Gamma+1}\frac{(5x-3)v}{2x(x-1)} + \frac{(\lambda^2-\lambda_k^2)v}{a^2x^3} + \Gamma\left(\frac{\Gamma-1}{\Gamma+1}\right)\frac{v^2\lambda_k(\lambda-\lambda_0)^2}{\alpha a^4x^4}\right) = \mathcal{N}}{\left(\frac{v^2}{a^2} - \frac{2}{\Gamma+1}\right) = \mathcal{D}} \tag{3.1}$$

gradient of fluid sound speed,

$$\frac{da}{dx} = \left(\frac{a}{v} - \frac{\Gamma v}{a}\right)\frac{dv}{dx} + \frac{(5x-3)a}{2x(x-1)} + \frac{\Gamma(\lambda^2 - \lambda_k^2)}{ax^3}, \tag{3.2}$$

and gradient of fluid specific angular momentum,

$$\frac{d\lambda}{dx} = 2x\Omega + x^2\frac{d\Omega}{dx}, \tag{3.3}$$

$$\text{where,} \quad \frac{d\Omega}{dx} = -\frac{\Gamma u \Omega_k(\lambda - \lambda_0)}{\alpha a^2 x^2} \tag{3.4}$$

is obtained by integrating equation (2.15) with the help of equation (2.17). Moreover, $\Omega_K(x) = \left(\sqrt{1/2x}\right)/(x-1)$ and $\lambda_K = \Omega_K x^2$ are the Keplerian angular velocity and the Keplerian specific angular momentum, respectively. In order to obtain the accretion disc solutions, we have to integrate equations (3.1–3.3).

Sonic point conditions:- Accretion onto black hole is necessarily transonic, since matter velocity far away from the object should be small and subsonic, and matter must cross the horizon of black hole with velocity equal to the speed of light (c), therefore, it is supersonic sonic close to the black hole. So, at some location the denominator $\mathcal{D}$ of equation (3.1) will go to zero and for smooth solution, numerator $\mathcal{N}$ also goes to zero, such a point is called a sonic point or critical point and this zero by zero form gives sonic point conditions. They are given by $\mathcal{N} = 0$ and $\mathcal{D} = 0$ and written as,

$$M_c^2 = \frac{v_c^2}{a_c^2} = \frac{2}{\Gamma + 1} \tag{3.5}$$

$$\left[\frac{(5x_c - 3)M_c^2}{2x_c(x_c-1)}\right]a_c^3 + \left[\frac{(\lambda_c^2 - \lambda_{K_c}^2)}{x_c^3}\right]a_c + \Gamma\left(\frac{\Gamma-1}{\Gamma+1}\right)\frac{M_c\lambda_{K_c}(\lambda_c - \lambda_0)^2}{\alpha x_c^4} = 0 \tag{3.6}$$

where $M_c, v_c, a_c, x_c, \lambda_c$ and λ_{K_c} are Mach number, the bulk velocity, the sound speed, the radial distance, the specific angular momentum and the specific Keplerian angular momentum at the critical point, respectively.

The radial velocity gradient at the critical point is calculated by employing the L′Hospital rule.

$$\left(\frac{dv}{dx}\right)_c = \left(\frac{dN/dx}{dD/dx}\right)_{r=r_c}, \Longrightarrow \mathcal{A}_2\left(\frac{dv}{dx}\right)_c^2 + \mathcal{A}_1\left(\frac{dv}{dx}\right)_c + \mathcal{A}_0 = 0, \tag{3.7}$$

where, $\mathcal{A}_2 = 2\Gamma M_c^2$, $\mathcal{A}_1 = \mathcal{A}_2\left(\frac{\mathcal{F}_{\lambda_0}}{4\alpha h_c} + \frac{M_c a_c \mathcal{F}_{x_c}}{\Gamma N}\right)$ and
$\mathcal{A}_0 = \mathcal{A}_2\left[\mathcal{F}_{x_c}\mathcal{F}_{\lambda_K} - \frac{M_c\mathcal{F}_{\lambda_0}}{2\alpha N a_c}\left(\frac{3}{2}\mathcal{F}_{x_c} + \frac{\Gamma}{a_c^2}\mathcal{F}_{\lambda_K}\right)\right] + \frac{\mathcal{A}_2 M_c\mathcal{F}_{\lambda_0}}{4\alpha N a_c}\left[\frac{2\lambda_c'}{\lambda_c-\lambda_0} - \frac{1}{x_c}\right]$
$+ \frac{M_c^2 a_c^2}{x_c(x_c-1)}\left[\frac{5}{2} - (3x_c-2)\mathcal{F}_{x_c}\right] + \frac{2(\lambda_c\lambda_c' - \lambda_{K_c}\lambda_{K_c}')}{x_c^3} - \frac{3\mathcal{F}_{\lambda_K}}{x_c}$.
where, $\mathcal{F}_{\lambda_0} = \frac{\lambda_{K_c}(\lambda_c-\lambda_0)^2}{x_c^4}$, $\mathcal{F}_{x_c} = \frac{(5x_c-3)}{2x_c(x_c-1)}$, $\mathcal{F}_{\lambda_K} = \frac{\lambda_c^2-\lambda_{Kc}^2}{x_c^3}$ and $h_c = N_c a_c^2$. Moreover, λ_c' and λ_{K_c}' represent the derivatives of λ_c and λ_{K_c} with respect to radial distance x at critical point. By combining equations (3.2 & 4.17) we get,

$$\left(\frac{da}{dx}\right)_c = \left(\frac{a_c}{v_c} - \frac{\Gamma v_c}{a_c}\right)\left(\frac{dv}{dx}\right)_c + \frac{(5x_c-3)a_c}{2x_c(x_c-1)} + \frac{\Gamma(\lambda_c^2-\lambda_{K_c}^2)}{a_c x_c^3}. \tag{3.8}$$

So, the solution of equations (3.1–3.3), can only be obtained if we know the sonic point and its conditions (equations 3.5–3.8).

Differential form of jet equations: Using equations (2.58,2.38) in equation (2.39), we get

$$\frac{d\Theta_j}{dr} = -\frac{\Theta_j}{N}\left[\frac{1}{v_j}\frac{dv_j}{dr} + \frac{1}{\mathcal{A}}\frac{d\mathcal{A}}{dr}\right] \tag{3.9}$$

The jet velocity gradient equation obtain by combining equations (2.4, 2.37-3.9), we get

$$\frac{dv_j}{dr} = \frac{\mathcal{N}_j}{\mathcal{D}_j}. \tag{3.10}$$

where,

$$\mathcal{N}_j = \frac{a_j^2}{\mathcal{A}}\frac{d\mathcal{A}}{dr} + \frac{\lambda_j^2}{x_j^3}\frac{dx_j}{dr} - \frac{1}{2(r_j-1)^2}\frac{dr_j}{dr} + R_f$$

and

$$\mathcal{D}_j = v_j - \frac{a_j^2}{v_j}.$$

where, $R_f = \mathcal{F}_{r_j} - v_j(\mathcal{E}_{r_j} + \mathcal{P}_{r_j})$ are the radiative forces due to radiation from the disc and it is correct up to first order in velocity (Mihalas & Mihalas 1984; Chattopadhyay & Chakrabarti 2002), which is explained in detail in the next section (3.4). Here, $\mathcal{F}_{r_j} = \sigma_T F_{r_j}/m_e c, \mathcal{E}_{r_j} = \sigma_T E_{r_j}/m_e$, and $\mathcal{P}_{r_j} = \sigma_T P_{r_j}/m_e$, where, σ_T is Thompson scattering cross section, m_e is the electron mass, and F_{r_j}, E_{r_j}, P_{r_j} are radiative flux, radiative energy density and radiative pressure, respectively.

The critical point conditions are,

$$a_{jc} = \frac{-A_2 + \sqrt{A_2^2 - 4A_1A_3}}{2A_1}; \qquad \& \qquad v_{jc} = a_{jc} \tag{3.11}$$

where, $A_1 = \left[\frac{1}{\mathcal{A}_c}\left(\frac{d\mathcal{A}}{dr}\right)_{r_c}\right]$, $A_2 = -(\mathcal{E}_{rj} + \mathcal{P}_{rj})$, $A_3 = \left[\mathcal{F}_{rj} - \frac{1}{2(r_{jc}-1)^2}\left(\frac{dr_j}{dr}\right)_{r_c} + \frac{\lambda_{jc}^2}{x_{jc}^3}\left(\frac{dx_j}{dr}\right)_{r_c}\right]$. The derivatives at r_{jc} is obtained by L′Hospital rule at sonic point as,

$$\left(\frac{dv_j}{dr}\right)_{r_c} = \left(\frac{dN_j/dr}{dD_j/dr}\right)_{r_c}; \quad \left(\frac{d\Theta_j}{dr}\right)_{r_c} = -\frac{\Theta_{jc}}{N}\left[\frac{1}{v_{jc}}\left(\frac{dv_j}{dr}\right)_{r_c} + \frac{1}{\mathcal{A}_c}\left(\frac{d\mathcal{A}}{dr}\right)_{r_c}\right] \tag{3.12}$$

The subscript c denotes the quantities at critical point in the outflow.

3.2 Solution Procedure

The accretion-ejection solutions have been solved self-consistently and simultaneously, and we are presenting the methodology to find such solutions in this sub-section. Since every solution has unique boundary values, which correspond to a set of flow parameters. These set of parameters are constant of motion ε, constant of integration λ_0, viscosity parameter α, and in presence of radiative cooling $\dot{M}$. In absence of cooling, the solutions are independent of $\dot{M}$. It has been shown earlier that the transonic solutions (solutions matching smoothly from subsonic to supersonic transition) have entropy higher than all other physical global solutions (i.e. those joining large distances and the horizon), (Bondi 1952; Chakrabarti 1990), so the entropy accretion rate ($\dot{\mathcal{M}}$) at the outer or inner boundary differentiates between subsonic and transonic branches. However, for viscous flow $\dot{\mathcal{M}}$ is not constant. So, we use the expression of entropy accretion rate (2.62) at the inner boundary to determine the transonic solution.

3.2.1 Method to find the sonic point

Since the angular momentum distribution equation is still in differential form (3.3). Therefore it is difficult to find the sonic point for a given boundary condition, i.e., sonic points are not known a priori. Moreover, this problem is compounded by the presence of coordinate singularity on the horizon makes it impossible to integrate the differential equations by considering the horizon as the initial point. The problem could be circumvented if the asymptotic values of the flow variables are known close to the horizon. So, by using the conservation equations and assuming free fall velocity close to the horizon, Becker & Le (2003) found the asymptotic distribution of the specific

angular momentum and the radial velocity close to the horizon. Equation (3.3) is a first order differential equation, so we can expand it by Frobenius expansion for $\lambda(x)$ about r_g (Becker & Le 2003),

$$\lambda(x) = \lambda_0 + \mathcal{B}(x - r_g)^{\tau}, \qquad x \longrightarrow r_g, \tag{3.13}$$

where, $\mathcal{B}$ and τ are constants, which can be determined. Equation (3.3) can be written as,

$$\frac{d\lambda}{dx} = \frac{2\lambda}{x} - \frac{\Gamma\Omega_K v(\lambda - \lambda_0)}{\alpha a^2}. \tag{3.14}$$

Using equation (3.13) in equation (3.14), in the limit $x \rightarrow r_{\rm g}$ we obtain,

$$\lim_{x\to r_g} \frac{\Gamma v \Omega_{\rm K}}{\alpha a^2}\mathcal{B}(x - r_{\rm g})^{\tau} = \frac{2\lambda_0}{r_{\rm g}} - \lambda_0' \tag{3.15}$$

We replace $v = u_{ff} = 1/\sqrt{(x-1)}$ and a between equations (3.15) and (2.62), use the expression of $\Omega_{\rm K}$, and the definition of H (equation 2.16), we obtain,

$$\lim_{x\to r_{\rm g}} \frac{\Gamma}{\alpha\sqrt{2x}(x - r_{\rm g})^{3/2}} \left[\frac{2x^3(x - r_{\rm g})}{\dot{\mathcal{M}}^2}\right]^{\frac{\Gamma-1}{\Gamma+1}} \mathcal{B}(x - r_{\rm g})^{\tau} = \frac{2\lambda_0}{r_{\rm g}} - \lambda_0', \tag{3.16}$$

A constant value warrants that net exponent of $(x - r_{\rm g})$ goes to zero, i.e. $\tau = \frac{\Gamma+5}{2(\Gamma+1)}$. Since by equation (3.13), $\lambda \rightarrow \lambda_0$ as $x \rightarrow r_{\rm g}$, therefore we have

$$\mathcal{B} = \frac{2\sqrt{2}\alpha\lambda_0}{\Gamma}\left(\frac{\dot{\mathcal{M}}^2}{2}\right)^{\frac{\Gamma-1}{\Gamma+1}}. \tag{3.17}$$

Now using values of $(\tau, \mathcal{B})$ in equation (3.13), we get λ at $x = x_{in}$,

$$\lambda_{in}(x) = \lambda_0\left[1 + \frac{2\sqrt{2}\alpha}{\Gamma}\left(\frac{\dot{\mathcal{M}}^2}{2}\right)^{\frac{\gamma-1}{\gamma+1}}(x-1)^{\frac{\gamma+5}{2\gamma+2}}\right],\ x \rightarrow 1 \tag{3.18}$$

and bulk velocity (v) with the help of equation (2.23) obtained as,

$$v_{in}(x) = u_{ff}(x)\left[1 + \frac{2Ex^2 - \lambda_0^2 - (\gamma+1)f(x)}{x^2u_{ff}^2(x) - (\gamma-1)f(x)}\right]^{1/2},\ x \rightarrow 1 \tag{3.19}$$

where the function $f(x)$ is $f(x) = \frac{2x^2}{\gamma^2-1}\left[\frac{\dot{\mathcal{M}}^2}{2x^3(x-r_g)}\right]^{\frac{\gamma-1}{\gamma+1}}$ and u_{ff} the free fall velocity in the pseudo-Newtonian potential geometry. So, v_{in} and λ_{in} are the flow variable calculated at a distance very close to the horizon, $x = x_{in} = 1.01$. For given values

of the parameters α, E, λ_0 at the horizon and $\dot{\mathcal{M}}_{in}$ at x_{in}, equations (3.18 - 3.19) can be used to determine the asymptotic values of the fluid variables close to the horizon, and which can be used as the initial values for the integration. With these values, equations (3.1 - 3.3) are integrated outwards, simultaneously checking for the location of the sonic point by using equations (3.5 - 3.8). For a given value of E, λ_0, α, there is only a unique value of $\dot{\mathcal{M}}$, which with pass through a sonic point. The sonic point x_c is determined iteratively, and once it is found, the sonic point conditions are used to integrate the equations of motions, outwards. It is well known that matter with angular momentum may posses *multiple critical points* (MCP). But the flow may pass through various sonic points only if a shock is present, in other words, the existence of MCP is mandatory for the formation of shock in black hole accretion. Only a supersonic flow can undergo shock transition and so existence of one sonic point at larger distance (i.e. x_{co}) from the horizon is warranted. The post shock flow is subsonic. However, the inner boundary condition of black hole accretion is supersonic, and hence the subsonic post-shock flow has to pass through another sonic point (x_{ci}), before it dives into the black hole. In other words, shock in black hole accretion may exist only if MCP exists. It is to be remembered though, that there is no smooth transition between various branches of the solution passing through different sonic points. This is true for both inviscid and adiabatic flows as well as viscous and non-adiabatic flow. However, if the flow is inviscid, for a given value of E and λ_0, all possible sonic points are known apriori. In case of viscous flow which is following a viscosity prescription of the form Equation (2.11), the existence of multiple sonic points can only be ascertained only if there is a shock.

3.2.2 Method to find the shock

Using shock conditions (2.27 - 2.30), which are described in subsection (2.1.2) of chapter 2, which gives flow variables of supersonic branch (λ_-, a_- and v_-) with the help of flow variables of a subsonic branch (λ_+, a_+ and v_+).

Since shock width is infinitesimally thin, so we assume that $d\Omega/dx$ is continuous across the shock. The angular momentum jump condition is calculated by considering the conservation of angular momentum flux, and is given by

$$\lambda_- = \lambda_+ + C_{sh}\left[\frac{a_+^2}{v_+} - \frac{a_-^2}{v_-}\right], \tag{3.20}$$

where, $C_{sh} = -v_+(\lambda_+ - \lambda_0)/a_+^2$. Using shock condition equations (3.19) and (3.20), the pre-shock sound speed and bulk velocity can be written as,

$$a_-^2 = k_1 v_- - \gamma v_-^2 \tag{3.21}$$

where, $k_1 = (a_+^2 + \gamma v_+^2)/(f v_+)$, $f = 1/(1 - R_{\dot{m}})$. Now substituting for a_- and λ_- in equation (3.23), we find a quadratic equation of v_- as,

$$C_2 v_-^2 + C_1 v_- + C_0 = 0 \tag{3.22}$$

where,

$$C_2 = \left[\frac{1}{2} - n\gamma - \frac{\gamma^2 C_{sh}^2}{2x_s^2}\right],$$

$$C_1 = \left[n k_1 - \frac{\gamma C C_{sh}}{x_s^2} + \frac{\gamma \lambda_0 C_{sh}}{x_s^2}\right],$$

$$C_0 = \left[\frac{\lambda_0 C}{x_s^2} - \frac{C^2}{2x_s^2} - k_2\right],$$

$$C = \lambda_+ + C_{sh}\left[\frac{a_+^2}{v_+} - k_1\right]$$

and

$$k_2 = E_+ - \Phi(x_s)$$

So, the mass outflow rate in term of flow variables at the shock front is given by,

$$R_{\dot{m}} = \frac{\dot{M}_{out}}{\dot{M}_{in}} = \frac{1}{[2\pi\Sigma_+ v_- x_s/(R\rho_j v_j(r_{cb})\mathcal{A}(r_{cb})) + 1]} \tag{3.23}$$

where, $R = \Sigma_+/\Sigma_- = v_-/v_+$, $\rho_j = \rho(r_b)exp(-x_j/h(r_b))$, $v_j(r_{cb})$ and $\mathcal{A}(r_{cb})$ are the compression ratio, jet base density, base velocity and base cross section, respectively. Here, $r_b = (x_{ci} + x_s)/3$ and $r_{CB} = \sqrt{r_b^2 + h_b^2}$, h_b being the height of the disc at r_b. The angular momentum of the jet $\lambda_j = \lambda|_{(x=r_b)} = \lambda_b$, i.e., the jets are launched with the angular momentum of the accretion disc at the base of the jet.

3.2.3 Self-consistent accretion-ejection solution

The accretion-ejection is computed self-consistently. We have set $\Gamma = 1.4$ and $x_{in} = 1.01$ throughout this section. The method to find the accretion-ejection solution is as follows,

1. First we assume that $R_{\dot{m}} = 0$. With chosen values of λ_0, E, and α , we follow the procedure described in subsection (3.2.1), i.e. determine the inner sonic point iteratively and integrate outwards. Equations (3.20 - 3.22) are checked to calculate the pre-shock quantities. We find out the outer sonic point (x_{co}) iteratively, from the pre-shock quantities. Two possibilities may arise, either the flow passes through only one sonic point and gives a smooth solution, or, finds a stable shock solution and passes through two sonic points. The location of the jump for which x_{co} exists is the possible shock location ($\tilde{x}_s$).

2. Once $\tilde{x}_s$ is found out, we assign $\mathcal{E}_j = \mathcal{E}_b$ and $\lambda_j = \lambda_b$ and solve jet equations (3.10 & 3.9) and compute the corresponding $R_{\dot{m}}$. Now, we can also compute the radiative moments $\mathcal{E}_{r_j}, \mathcal{F}_{rj}$ and $\mathcal{P}_{rj}$ from flow variables of accretion disc as discussed in next section (3.4) and these radiative moments are used in jet equation. Since entire post-shock disc participates in the jet generation (Molteni et al. 1994; Nagakura & Yamada 2009). The jet base is the post-shock disc, so the jets are launched with the post-shock disc quantities. If $x = r_b$ is the jet launch site in the post-shock disc, then the specific energy of the disc at r_b i.e. $\mathcal{E}_b = \mathcal{E}(r_b)$, and the post-shock specific angular momentum at r_b i.e. $\lambda_b = \lambda(r_b)$ and the density at the top of the disc at r_b i.e. ρ_b, are the flow variables of the jet at its base. Here we have taken $r_b = (x_{ci} + x_s)/3$, and since the disc is assumed to be in hydro-static equilibrium along the z direction, $\rho_j = \rho(r_b)\exp(-x_j/h_b)$, where, h_b is the height of the disc at r_b. The jet velocity v_{jb} and the sound speed a_{jb} at the jet base are not arbitrarily assigned, but are computed self consistently. We eliminate a_j from equation (2.40) by using equation (2.63), and express $\mathcal{E}_b$ in terms of $\dot{\mathcal{M}}_j$, v_{jb}, λ_b etc. Since $\mathcal{E}_b$ and λ_b are obtained from the post-shock disc and therefore known for the jet, we iterate with various values of entropy i.e. $\dot{\mathcal{M}}_j$ to obtain the correct value of v_{jb} and a_{jb}, with which the unique transonic solution is determined by integrating equation (3.10) and checking for the sonic point conditions (3.11,3.12). Once the transonic jet solution is obtained, then $R_{\dot{m}}$ is easily calculated from equation (3.23).

3. We put this value of $R_{\dot{m}}$ into shock conditions (3.20 - 3.22), go back to step (1) to recalculate a new shock location and from step (2) to recalculate the new $R_{\dot{m}}$.

4. Steps (2) & (3) are repeated till the temporary shock location $\tilde{x}_s$ converges to the actual shock location (x_s). The converged shock solution therefore gives the actual jet solution too. Therefore, we find out the self-consistent, converged accretion-ejection solutions, there are three iteration processes, namely, (1) to find out inner sonic point of accretion disc, (2) accretion shock and the outer sonic point, and (3) the jet sonic point when launched with the post-shock disc variables. We also find that the $\dot{\mathcal{M}}_j > \dot{\mathcal{M}}_-$ and $\dot{\mathcal{M}}_+ > \dot{\mathcal{M}}_-$. Since matter prefers higher entropy solutions, therefore, the post-shock fluid would prefer both the channels, one through the x_{ci} onto the black hole, and the other through r_{jc} and out of the disc-jet system. In other words, a shock in accretion would generate a bipolar outflow from the post-shock region too.

The outer boundary is chosen as $x_{inj} = 10^4 r_g$, or the distance at which $\lambda(x_{inj}) = \lambda_K(x_{inj})$, which ever is shorter.
Since, accretion-ejection are coupled system and matter ejected from accretion disc, so we have divided it into two sections, first the study of viscous accretion disc and second radiatively-thermally driven outflow from disc.

3.3 Study of viscous accretion disc:

In this section, considering $R_{\dot{m}} = 0$, we have generated all types of possible accretion solutions in advective regime with and without viscosity and also compared shock solutions with global smooth solutions. We have also studied the effect of viscosity on accretion solutions by keeping either inner boundary conditions (IBC) or outer boundary conditions (OBC) fixed.

3.3.1 All possible accretion solutions in the advective regime:

Since black hole accretion is necessarily transonic, at first, we present the simplest rotating transonic solutions i.e., inviscid global solutions in Figs. 3.1a-d. The inviscid solutions are presented as an attempt to recall the simplest accretion case (Chakrabarti 1989; Das et al. 2001). For inviscid flow the constants of motions are E, λ ($= \lambda_0$), and if outflows are not present then, $\dot{M}$ is also a constant of motion. Moreover, in absence of viscosity, it straightaway follows from Eq. (2.23) that $E = \mathcal{E}$. In Figs. 3.1a-d, accretion solutions in terms of the Mach number M ($= v/a$) distribution are presented, and in

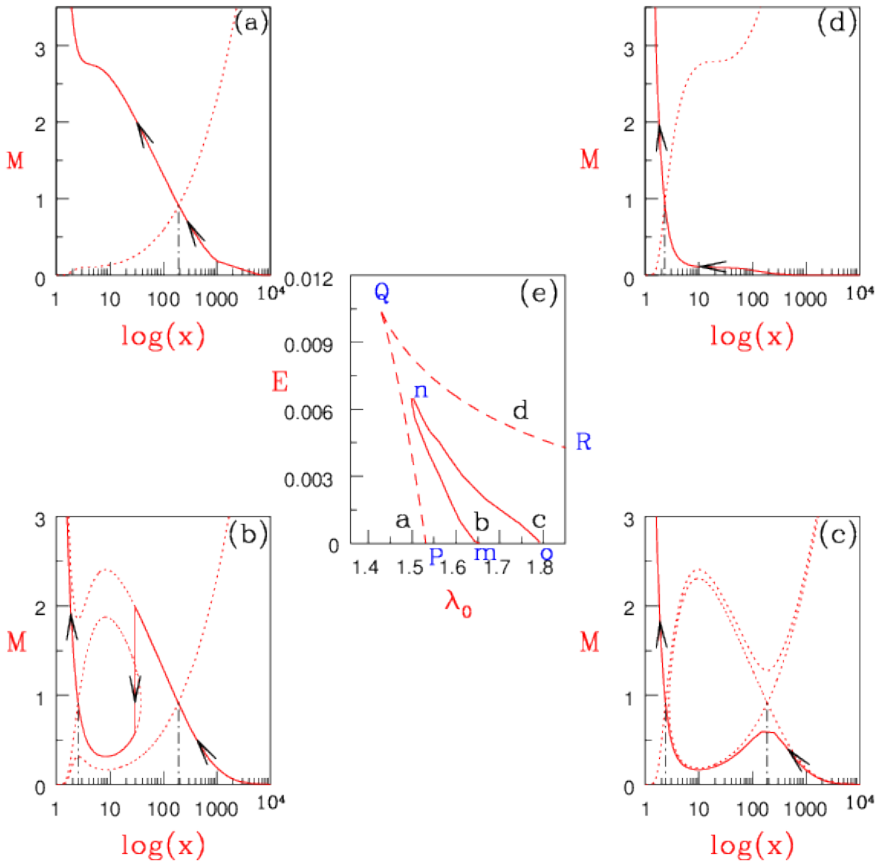

Figure 3.1: MCP - The domain for MCP (dashed, PQR) and shock (solid, mno) in $E-\lambda$ parameter space (e) is presented. The solution topologies or the plot of Mach number M with $log(x)$ of the O type for $E = 0.001,\ \lambda = 1.5$ (a); A type for $E = 0.001,\ \lambda = 1.68$ (b); W type fort $E = 0.001,\ \lambda = 1.75$ (c); and I type for $E = 0.005,\ \lambda = 1.77$(d), are presented. The solution type and their location in the parameter space is also indicated in (e). All the plots are for $\alpha = 0$. The dotted lines in the panels named a, b, c, and d show all possible solutions while, the solid line with arrow heads show the actual accretion solution. The vertical long-short dashed line shows the location of the sonic points. Kumar & Chattopadhyay (2013).

Fig. 3.1e, the $E = \mathcal{E} - \lambda_0$ parameter space for multiple sonic point, PQR and the shock, mno is presented too. Depending on E & λ_0 of the flow, the solutions are also different. If the λ_0 is low, there is only one outer sonic point x_{co}, and solution type is O-type or Bondi type ($E = 0.001,\ \lambda_0 = 1.5$, Fig. 3.1a). As λ_0 is increased, the number of physical sonic points increases to two and the accretion flow which becomes supersonic through x_{co} can enter the black hole through x_{ci} if a shock condition is satisfied. Although the shock free solution is possible but in this part of the parameter space a shocked solution will be preferred because a shocked solution is of higher entropy (or in other words of higher $\dot{\mathcal{M}}$). Such a class of solution is called A-type ($E = 0.001,\ \lambda_0 = 1.68$, Fig. 3.1b). For even higher λ_0 only one sonic point is possible ($E = 0.001,\ \lambda_0 = 1.75$ for W-type; and $E = 0.005,\ \lambda_0 = 1.77$ for I-type shown in Figs 3.1c and d), and the solutions are wholly subsonic till x_{ci} and then dives on to black hole supersonically. W-type solutions are different than I-type, in the sense, W-type is still within the MCP domain while I-type is not. Moreover, I-type is a smooth monotonic solution, although W-type is smooth and shock free but is not monotonic and has an extremum at around x_{co}. The parameter space $E - \lambda_0$, bounded by solid line (mno) shows the RH shock parameter space, while the dotted one (PQR) shows the MCP domain (Fig. 3.1e). It is to be noted, that in the inviscid limit, accretion is only possible if $\lambda_0 < \lambda_K$.

Figures 3.2 (a, e, i, m), represent the inviscid solutions corresponding to the O-type solutions ($E,\ \lambda_0 =\ 0.001,\ 1.5$), A-type ($E,\ \lambda_0 =\ 0.001,\ 1.68$), W-type ($E,\ \lambda_0 =\ 0.001,\ 1.75$), and I-type ($E,\ \lambda_0 =\ 0.005,\ 1.75$), and are also shown in figures 3.1 a-d. Figures 3.2 a-d, has same E & λ_0, but progressively increasing $\alpha = 0.06$ (Fig. 3.2 b), 0.068 (Fig. 3.2 c) and 0.07 (Fig. 3.2 d). Similarly for Figs. 3.2 (e-h, i-l and m-p), each set is for same E & λ_0 but different α. Interestingly, the viscous I-type is in principle the much vaunted ADAF type solution presented in Figs 3.2 (d, h, k-l, and n-p). The shock-free solution is characterized by monotonic spatial distribution of flow variables, and wholly subsonic except very close to the horizon which are essentially the viscous I-type solutions and has also been shown by (Lu et al. 1999; Becker et al. 2008; Das et al. 2009). It is evident from Figs. 3.2 a-p, that the effect of viscosity is to create additional sonic points in some part of the parameter space, and might trigger shock formation where there was no shock, opening up of closed topologies, while removing both shock and multiple critical points in other regime of the parameter space. All of this is achieved by removing angular momentum outwards while increasing the entropy

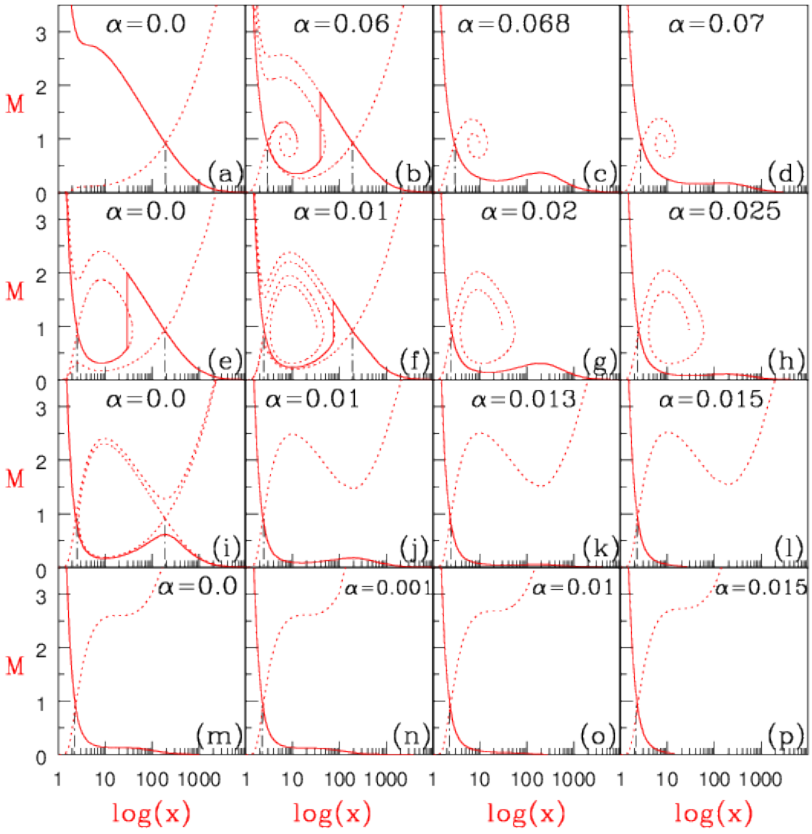

Figure 3.2: Effect of viscosity - Variation of M with $log(x)$ for the accretion solutions with different viscosity parameter α. In a, e, i, m we present inviscid solutions corresponding to the O, A, W, I -type of solutions from Figs. 2a-d. Towards right E, λ_0 is kept the same but α is increased. The flow parameters for which these plots are generated $E = 0.001,\ \lambda = 1.5$ (a, b, c, d); $E = 0.001,\ \lambda = 1.68$ (e, f, g, h); $E = 0.001,\ \lambda = 1.75$ (i, j, k, l) and $E = 0.005,\ \lambda = 1.75$ (m, n, o, p). The viscosity parameter α is mentioned on the figure. The vertical long-short dashed line shows the location of sonic points. Kumar & Chattopadhyay (2013).

inwards. In this connection one may find two kind of critical viscosity parameters in the advective domain. If the inviscid solution is O-type (Fig. 3.2 a), then there would be a lower bound of critical viscosity $\alpha_{\rm cl}$ which would transport angular momentum in a manner that would trigger the standing shock. And there would be another upper bound of viscosity parameter $\alpha_{\rm cu}$ that would quench the standing shock. While, if the inviscid solution has a shock to start with (Fig. 3.2 e), then there could only be $\alpha_{\rm cu}$. For the case presented in Figs. 3.2 a-d, $\alpha_{\rm cl} = 0.0465$ and $\alpha_{\rm cu} = 0.065$. And for the case presented in Figs. 3.2 e-h, $\alpha_{\rm cu} = 0.0126$.

So far, we have compared solutions with different viscosity but same inner boundary condition (IBC), ($E,\ \lambda_0$). Let us compare two solutions with same outer boundary condition (OBC). In Figs. 3.3 a-e, we compare two solutions starting at the same outer boundary $x_{inj} = 5117$, same grand energy $E = 10^{-3}$ and $\lambda_{inj} = \lambda_K(x_{inj}) = 50.6$. Both the solution starts with the same entropy $\sim \dot{\mathcal{M}}_{inj} = 2.72 \times 10^{-5}$. For $\alpha = 0.15$ (solid) the accretion solution has a standing shock at $x_s = 49.68$ (the vertical jump in solid), while the shock free solution is for $\alpha = 0.02$ (dotted). The flow variables plotted are M (Fig. 3.3 a), a (Fig. 3.3 b), u (Fig. 3.3 c), λ (Fig. 3.3 d), and $\mathcal{E}$ (Fig. 3.3 e). In case of inviscid flow $E = \mathcal{E}$ is constant, for viscous flow E is still a constant of motion but $\mathcal{E}$, the specific energy, varies with x as is shown in Fig. 3.3 e. The inner part of the shocked solution is faster, hotter, and of lesser angular momentum. The inner boundary for the shocked flow is $E = 10^{-3},\ \lambda_0 = 1.29$, while that for the shock free solution is $E = 10^{-3},\ \lambda_0 = 1.7$. The jump in λ at the shock follows Eq. 3.20. Interestingly, the post shock flow is of higher entropy [$\dot{\mathcal{M}}(x \sim 1) = 7.49 \times 10^{-5}$] than the inner part of the shock free solution [$\dot{\mathcal{M}}(x \sim 1) = 7.12 \times 10^{-5}$]. Although it may seem contradictory that a shock free solution exists for lower α, while shocked solution appears for higher α, however, it is to be remembered that with such high λ_{inj}, there would be no accretion solution for $\alpha = 0$. One has to have a certain non-zero viscosity to even have a global (that connects horizon and outer edge) solution. In fact, for this particular case we have identified a limiting viscosity parameter $\alpha_1 = 0.00747$, such that advective global solutions are possible for any viscosity parameter $\alpha \geq \alpha_1$. And for flows starting with such high initial λ_{inj}, if the viscosity parameter α is small, then the λ distribution will be higher. Therefore, for such high λ radial velocities will not be high enough to become supersonic and form a shock. So one needs higher $\alpha \geq \alpha_{\rm cl} = 0.1496$ to reduce the angular momentum to the extent that may produce standing accretion shock.

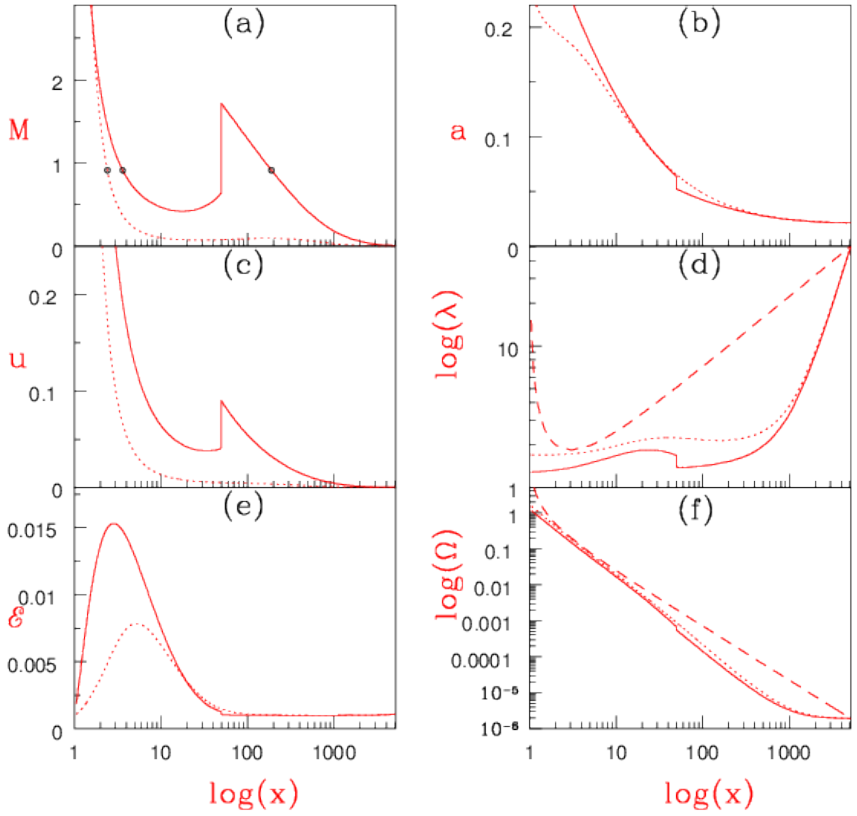

Figure 3.3: Comparison of shock and shock free solutions - Comparison of shock free (dotted) and shocked solution (solid). Both the solution starts with the same outer boundary condition $x_{inj} = 5117$, $\lambda_{inj} = \lambda_K(x_{inj}) = 50.6$, $E = 10^{-3}$. The viscosity parameter for the shock free solution is $\alpha = 0.02$ (dotted) and that for the shocked one $\alpha = 0.15$ (solid). Various flow variables are plotted are M (a), a (b), u (c), λ (d), $\mathcal{E}$ (e) and Ω (f) as a function of x. The sonic points are marked with open circles (a). The shock free solution has only one x_{ci}, the shocked solution has both x_{ci} and x_{co} and the shock location is at $x_s = 49.68$. Dashed plots of λ_K and Ω_K in (d) and (f) are Keplerian angular momentum and angular velocity drawn for comparison. Kumar & Chattopadhyay (2013).

And if α is increased beyond another critical value $\alpha_{\rm cu} = 0.1555$, steady shock is not found. Hence one can identify three critical α's for accretion flows starting with the same outer boundary condition, where the angular momentum at the outer boundary is local Keplerian value. Interestingly, α prescription originally invoked to generate Keplerian disc (Shakura & Sunyaev 1973), can produce sub-Keplerian accretion flow with or without shock even if angular momentum is Keplerian at the outer boundary. This is not surprising since, the gravitational energy released by the infalling matter, would be converted to kinetic energy and thermal energy (by compression and viscous dissipation). If the gravitational energy is converted to thermal energy and only the rotation part of kinetic energy, and also if the thermal energy gained by viscous dissipation is efficiently radiated away, then one would produce Keplerian disc solutions. The λ_K (Fig. 3.3d) and Ω_K (Fig. 3.3f) are presented for comparison. In the present study, the radiative processes have been ignored which produces hot flow, but the advection terms have not been ignored. Therefore, sub-Keplerian flow with significant advection are obtained.

The effect of α on shock location x_s is an interesting issue. Numerical simulations show that, for fixed outer boundary condition, x_s expands to larger distances with the increase of α (Lanzafame et al. 1998; Lee et al. 2011), while analytically Chattopadhyay & Das (2007) showed that for the same outer boundary condition, x_s shifts closer to the horizon with the increase in α. Although, the viscosity prescription of Chattopadhyay & Das (2007) and the simulations are different, namely the former chose the stress to be proportional to total pressure, while in simulations the stress is proportional to the shear, still viscosity reduces angular momentum, and we know for lower angular momentum if the shock forms, it should form closer to the black hole! Since the viscosity prescription in this study is similar to the simulations, we should be able to answer the dichotomy. So a concrete question may arise, if viscosity is increased, does the x_s expands to larger distances or, contracts to a position closer to the horizon? If the viscosity acts in a way such that the λ_+ (immediate post-shock λ) is less than its inviscid value at the shock then x_s will move closer to the horizon. However, such simple minded reasoning may fail, if shocks exists, then the post shock flow being hotter would transport more efficiently than the immediate pre-shock flow. So although, $\lambda_- < \lambda(x_{inj})$, it is not necessary λ_+ will be less than $\lambda(x_{inj})$. We scourged the parameter space to find the answer, and in the following we present the explanation. Let x_b be

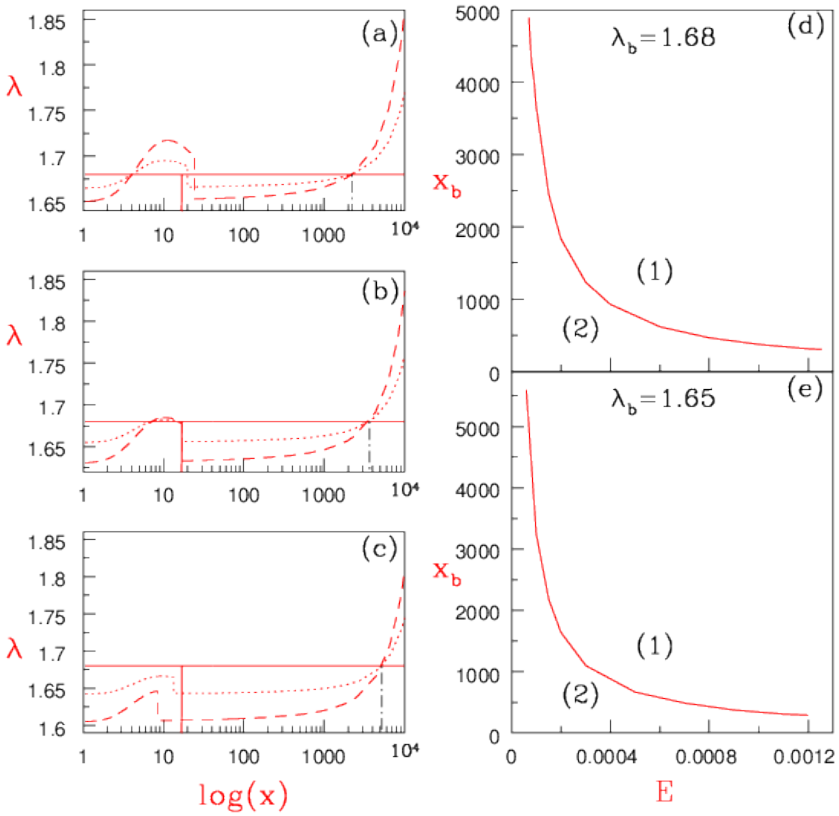

Figure 3.4: Effect of BC - Variation of λ with $log(x)$ of shocked accretion flow (a, b, c), for parameters $E = 0.0001$, & $\lambda_b = 1.68$. Each curve represents $\alpha = 0.0$ (solid), $\alpha = 0.0075$(dotted) and $\alpha = 0.015$ (dashed). First three panels are for $x_b = 2220r_g$(a), $x_b = 3660r_g$ (b), and $x_b = 5230r_g$ (c). Vertical solid line and dash-dotted line show the shock location for $\alpha = 0.0$ curve and outer boundary location (x_b), respectively. The variation of limiting x_b with E for $\lambda_b = 1.68$ (d), and $\lambda_b = 1.65$ (e). Domain 1 represents all x_b for which x_s decrease with the increase with α, but for any x_b in 2, x_s will increase with the increase of α. Kumar & Chattopadhyay (2013).

the distance at which the λ distribution of the viscous solution is coincident with the λ value of the inviscid solution, let us further assign $\lambda_b = \lambda(x_b)$. It is to be remembered that $\lambda_0 = \lambda_b$ for the inviscid ($\alpha = 0$) solution, but $\lambda_0 < \lambda_b$ for viscous solution because viscosity reduces the angular momentum. In all the simulations done on viscous flow in the advective regime referred in this study, one starts with an inviscid solution (since analytical solutions are easily available), and then the viscosity is turned on, keeping the values at the outer boundary fixed. In other words, it is this x_b that is called the outer boundary in numerical simulations, and generally, $x_b \lesssim$ few $\times$ 100 since it is computationally expensive to simulate a large domain from just outside the horizon to few$\times$1000 r_g and still retain required resolution to achieve intricate structures in the accretion disc. In Figs. 3.4 a-c, we compare the $\lambda(x)$ of shocked accretion flows starting with the same $E = 10^{-4}$, & $\lambda_b = 1.68$ for various viscosity parameters such as, $\alpha = 0$ (solid), $\alpha = 0.0075$ (dotted), $\alpha = 0.015$, but for different points of coincidence, e.g. $x_b = 2220$ (5a), $x_b = 3660$ (5b), and $x_b = 5230$ (5c). The vertical solid line is the location of the shock for the inviscid flow. Although, we match the λ_b at x_b of the viscous and inviscid solutions, we still integrate outwards upto $x_{inj} = 10^4$. Since $x_{inj} >> x_b$, this distance may be considered as the size of the disc. In Figs. 3.4a-c, we show that depending upon the choice of x_b, the outer boundary conditions can be remarkably different. If x_b is short (Fig. 3.4a), then flow with higher α will be able to match λ_b at the same x_b, only if one starts with much higher λ_{inj}, in other words the gradients will be steeper. Consequently, the increase of α will create higher λ_+, which will result in the increase of x_s. In case x_b is large (Fig. 3.4c), the gradients are smoother and the resulting λ_{inj} will be approximately similar for any value of α. Hence as α is increased, λ_+ would decrease and consequently x_s will decrease too. In Fig. 3.4a, the parameters are $\lambda_{inj} = \lambda_b = 1.68$ for inviscid or $\alpha = 0$ (solid), $\lambda_{inj} = 1.769$ for $\alpha = 0.0075$ (dotted) and $\lambda_{inj} = 1.858$ for $\alpha = 0.015$ (dashed). Since $x_b = 2220$ is short, the gradients are steeper, and as discussed above, in such cases x_s increases with increasing α. While in Fig. 3.4c, $\lambda_{inj} = 1.744$ for $\alpha = 0.0075$ (dotted) and $\lambda_{inj} = 1.807$ for $\alpha = 0.015$ (dashed), where $x_b = 5230$ is larger, the shock x_s decreases with increasing α. Since for shorter values of x_b, x_s increases with the increase of α, and for longer x_b, x_s decreases with the increase of α, so a limiting x_b should exist for which x_s will neither increase or decrease with the increase of α. In Fig. 3.4b, we show that for $x_b = 3660$, the shock neither increase or decrease with the increase of α.

Moreover, these shock forms with the help of both centrifugal force and thermal pressure in the disc. Since, viscosity by nature reduces λ as the fluid advects but also increases thermal pressure and these processes are highly non-linear with fluid moving close to the compact objects. Therefore, for the shorter x_b reduction of λ is lesser compare to longer x_b, so λ_- for shorter x_b is higher than longer x_b and therefore thermal compression increases λ_+ in post-shock region with increase of α and resulting x_s increases for the former case as in fig. (3.4 a). For the longer x_b reduction in λ is more than shorter x_b, so the momentum balance across the shock location is restored closer to the horizon as in fig. (3.4 b). Figure (3.4 c) reduction in λ is exactly compensated by increase in thermal pressure in the flow with increasing α, so for such boundary x_b, shock does not moves away or inward.

In Figs. 3.4 d & e, we plot the limiting x_b as a function of E for $\lambda_0 = 1.68$ (d) and $\lambda_0 = 1.65$ (e). The domain name '1' corresponds to any x_b at which the x_s will decrease and '2' signifies the domain where at any x_b, x_s increases with α. Hence Fig. 3.4 a lies in domain 2, Fig. 3.4b on the curve, and Fig. 3.4 c on domain 1 of Fig. 3.4 d. Incidentally, if the outer boundary condition for all the advective solutions start with the Keplerian angular momentum, then the shock location x_s decreases with the increase of α. Since the numerical simulations are usually performed with a smaller computational box ($x_b \sim$ few $\times 10$— few$\times 100$), this is similar to the case x_b lying in the domain 2. As a result, earlier simulations of advective accretion flows have reported the increase of x_s with the increase of α. Hence we may conclude that the increment of x_s with the increase of α is an artifact of faulty assignment of outer boundary condition in the simulations. In Fig. 3.5, the E—λ_0 parameter space for standing accretion shock has been plotted for various viscosity parameters, $\alpha = 0$, 0.05, 0.1, 0.15, 0.2, 0.25, 0.3. Since viscosity will in general reduce the angular momentum along the flow, λ_0 should decrease with the increase of α. As a result, the shock parameter space shift to the lower end of the λ_0 scale. One may compare the RH shock parameter space with that of the isothermal shock space Das et al. (2009). For all possible boundary conditions, RH shocks may be obtained upto $\alpha = 0.3$. For values outside the bounded regions there are no standing shocks, although transient and oscillating shocks may still exist. It is to be remembered though, the parameter space shown here corresponds to inner boundary. In the outer boundary λ might be much higher for viscous flow as has been shown in Figs. 3.3 a-e.

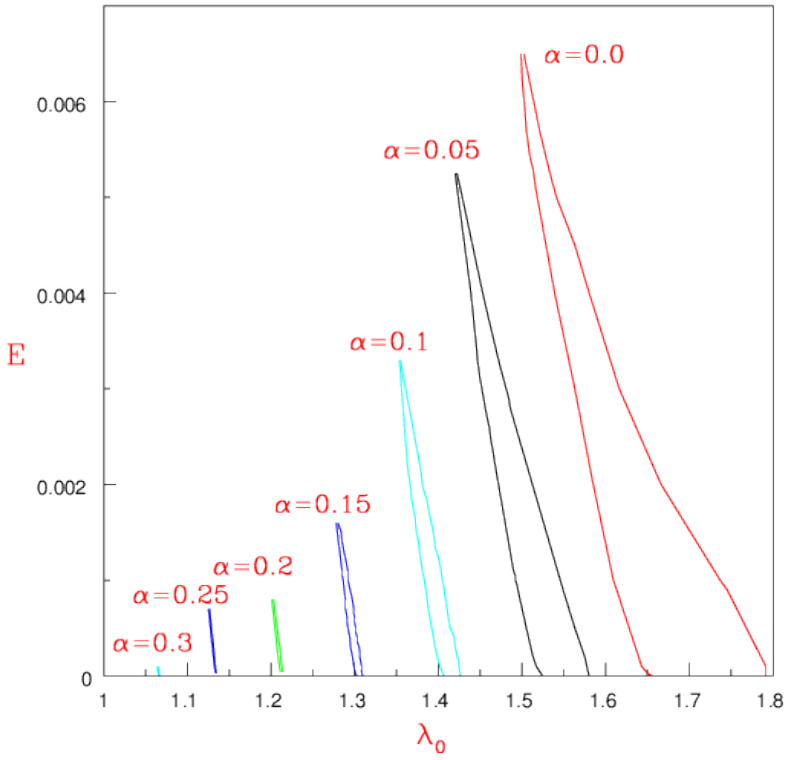

Figure 3.5: Shock parameter space - E—λ_0 parameter space for shock, for various viscosity parameters $\alpha = 0$, 0.05, 0.1, 0.15, 0.2, 0.25, 0.3 marked on the figure. Kumar & Chattopadhyay (2013).

3.4 Study of radiatively-thermally driven outflows from the disc:

In the previous section we discussed all possible solutions that one can have in presence of viscosity prescription given by Equation (2.11), and non-dissipative shocks. In this section we present the self consistent inflow-outflow solutions, where the outflow is acted by radiative moments from the disc. In presence of massloss, the mass conservation equation across the shock will be modified in the form of Equation (2.31). All the steps mentioned in subsection (3.2.3) are followed to compute the self-consistent inflow-outflow solution. Assuming jets are rotating, adiabatic and optically thin, using Thompson elastic scattering between radiation and matter. We have used radiative forces R_f into the Euler-momentum equation (2.37) of jet in this section, which we ignored in previous section.

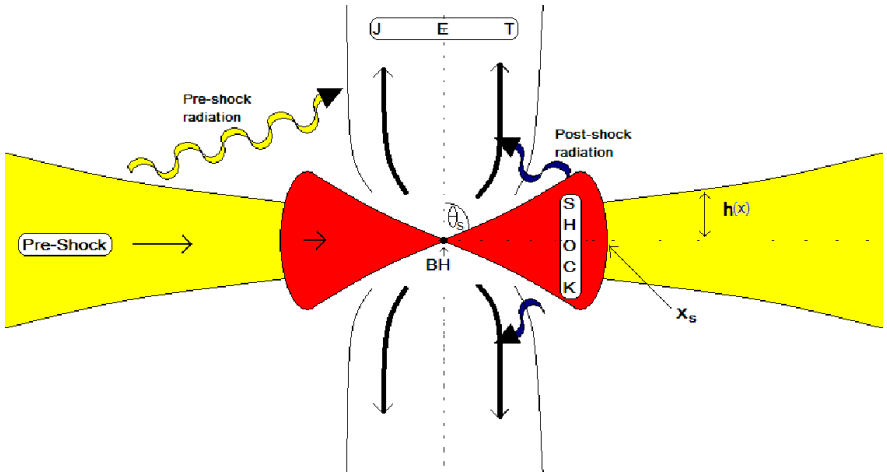

Figure 3.6: Cartoon for disc-jet system - BH is the acronym for black hole. Both pre-shock and post-shock disc shines radiation on the bipolar jet.The shock location x_s, the axis (vertical dotted) and equatorial plane (horizontal dotted) are shown. The half height $h(x)$, and the opening half angle θ_s of the funnel like region between the inner torus is shown. Kumar et al. (2014).

3.4.1 Radiative moments

Now as the jet is generated due to compression as well as shock heating from the post-shock disc (see Fig. 3.6), the jet will be moving through the radiation field of the

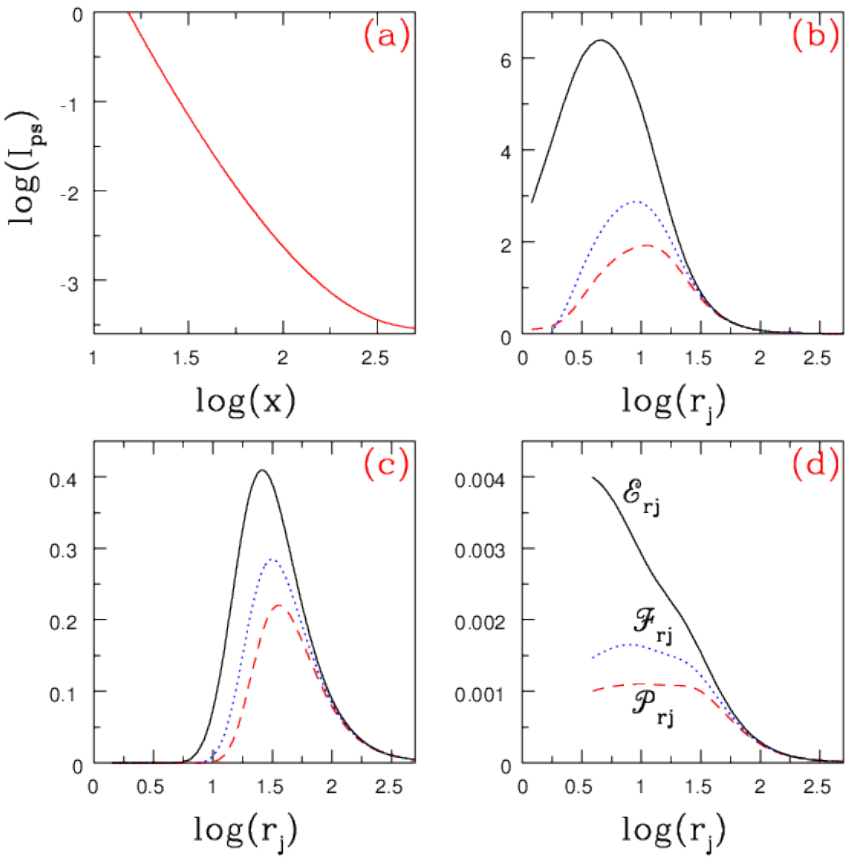

Figure 3.7: Distribution of radiative moments - (a) Normalized intensity of synchrotron radiations (solid, red) from pre-shock disc with $log(x)$ (b) Moments of the radiation field due to the post-shock disc $\mathcal{E}_{r_j s}/\mathcal{K}_0$ (solid, black), $\mathcal{F}_{r_j s}/\mathcal{K}_0$ (dotted, blue) and $\mathcal{P}_{r_j s}/\mathcal{K}_0$ (dashed, red), are plotted with $log(r_j)$, and (c) $\mathcal{E}_{r_j ps}/\mathcal{J}_0$ (solid, black), $\mathcal{F}_{r_j ps}/\mathcal{J}_0$ (dotted, blue) and $\mathcal{P}_{r_j ps}/\mathcal{J}_0$ (dashed, red), the moments of the radiation field due to the pre-shock disc are plotted. (d) Total moments of radiation field due to post-shock and pre-shock disc, are generated by an accretion disc with parameters $E = 3.5\times10^{-3}$, $\lambda_0 = 1.5435$, $\alpha = 0.02$, $\gamma = 1.4$ (forming shock at $x_s = 15.18$). The radiation field is for equal post-shock and pre-shock luminosities $\ell_s = \ell_{ps} = 0.4$. Kumar et al. (2014).

accretion disc. We now outline the method to compute radiative moments and the net radiative acceleration of the jet. The radiative acceleration term is proportional to the radiative flux F_{r_j}, but the radiation drag term (negative terms in R_f of equation 3.10) depends on jet flow velocity v_j, the radiation energy density E_{r_j} and the radiation pressure P_{r_j}. Figure 3.6 shows the schematic diagram of the radiations coming from various parts of the disc, and how it can interact with the out flowing jet, generated due to shock heating of the inner disc. The radiative moments along the jet streamlines (r_j) are calculated from the post-shock (s) and pre-shock (ps) disc respectively. The radiative terms in equation 2.37 are given by,

$$\mathcal{E}_{r_j} = \frac{\sigma_T}{mc}\left(\int I_s d\Omega_s + \int I_{ps} d\Omega_{ps}\right) = \frac{\sigma_T}{m}\left(E_{r_j s} + E_{r_j ps}\right) = \mathcal{E}_{r_j s} + \mathcal{E}_{r_j ps} \tag{3.24}$$

$$\mathcal{F}_{r_j} = \frac{\sigma_T}{mc}\left(\int I_s \hat{r_j} d\Omega_s + \int I_{ps} \hat{r_j} d\Omega_{ps}\right) = \frac{\sigma_T}{mc}\left(F_{r_j s} + F_{r_j ps}\right) = \mathcal{F}_{r_j s} + \mathcal{F}_{r_j ps} \tag{3.25}$$

$$\mathcal{P}_{r_j} = \frac{\sigma_T}{mc}\left(\int I_s \hat{r_j}\hat{r_j} d\Omega_s + \int I_{ps} \hat{r_j}\hat{r_j} d\Omega_{ps}\right) = \frac{\sigma_T}{m}\left(P_{r_j s} + P_{r_j ps}\right) = \mathcal{P}_{r_j s} + \mathcal{P}_{r_j ps} \tag{3.26}$$

Since the jet streamline is close to the axis of symmetry, we calculate the radiative moments on the axis and approximate these to hold at the same radial distance on the jet streamline. Here, we are not dealing with the detailed features of the radiation spectrum from the accretion disc. Rather, we are interested to see the effect of the total pre-shock and post-shock radiation on the acceleration of the jet. Hence, we do not include radiative transfer dynamically into the hydrodynamic solution. To calculate the moments of radiation due to the pre-shock disc, as an example, we consider only synchrotron processes from the pre-shock disc.

The synchrotron emissivity is due to the presence of stochastic magnetic field, where the magnetic pressure (p_m) is in partial equipartition with the gas pressure (p_g), i.e.

$$p_m = \frac{B^2}{8\pi} = \beta p_g; \quad \text{where, } 0 \leq \beta \leq 1,$$

here, for $\beta = 0$ implies no magnetic field and therefore the total pressure in Eq. (2.14) $p = p_g$, while $\beta = 1$ implies strict equipartition between gas and magnetic pressure and therefore $p = p_g + p_m$. The analytical expression for synchrotron emissivity is given by Shapiro & Teukolsky (1983), and the resulting intensity is,

$$I_{ps} = I_{syn} = \frac{16}{3}\frac{e^2}{c}\left(\frac{eB}{m_e c}\right)^2 \Theta^2 n_e \left(\frac{hr_g}{sec\theta_{ps}}\right) \quad \text{erg cm}^{-2}\text{s}^{-1} \tag{3.27}$$

where, Θ, n_e, h and θ_{ps} are the pre-shock local dimensionless temperature $k_bT/(m_ec^2)$, electron number density, disc half height and angle from the axis of symmetry to the pre-shock disc surface, respectively. The dependence of I_{ps} on disc radius is through flow variable like T & n_e. Integrating I_{ps} over the pre-shock disc gives us the pre-shock luminosity ℓ_{ps}. The radiative intensity from the post shock disc is $I_s = \ell_s/A_s$, where ℓ_s is the post-shock luminosity in units of Eddington luminosity and A_s is the total surface area of the post-shock disc. The total luminosity is $\ell = \ell_s + \ell_{ps}$. The moments of the radiation field above the accretion disc was calculated before (Chattopadhyay & Chakrabarti 2000, 2002; Chattopadhyay et al. 2004; Chattopadhyay 2005) , and for the above mentioned approximations, they are given by,

$$\mathcal{E}_{r_js} = 2\pi\mathcal{K}_0\int_{x_{in}}^{x_s}\frac{zxdx}{[(z-x\ cot\theta_s)^2+x^2]^{3/2}};\ \ \mathcal{E}_{r_jps} = 2\pi\mathcal{J}_0\int_{x_s}^{x_{inj}}\frac{a^5zxdx}{v^2x^{3/2}(x-1)[(z-x\ cot\theta_{ps})^2+x^2]^{3/2}}, \tag{3.28}$$

$$\mathcal{F}_{r_js} = 2\pi\mathcal{K}_0\int_{x_{in}}^{x_s}\frac{z(z-x\ cot\theta_s)xdx}{[(z-x\ cot\theta_s)^2+x^2]^2};\ \ \mathcal{F}_{r_jps} = 2\pi\mathcal{J}_0\int_{x_s}^{x_{inj}}\frac{a^5z(z-x\ cot\theta_{ps})xdx}{v^2x^{3/2}(x-1)[(z-x\ cot\theta_{ps})^2+x^2]^2}, \tag{3.29}$$

$$\mathcal{P}_{r_js} = 2\pi\mathcal{K}_0\int_{x_{in}}^{x_s}\frac{z(z-x\ cot\theta_s)^2xdx}{[(z-x\ cot\theta_s)^2+x^2]^{5/2}};\ \ \mathcal{P}_{r_jps} = 2\pi\mathcal{J}_0\int_{x_s}^{x_{inj}}\frac{a^5z(z-x\ cot\theta_{ps})^2xdx}{v^2x^{3/2}(x-1)[(z-x\ cot\theta_{ps})^2+x^2]^{5/2}}, \tag{3.30}$$

where, $\theta_s = tan^{-1}(x_s/h_s)$, $h_s = \sqrt{(2/\gamma)}(a_{s+})x_s^{1/2}(x_s-1)$ and $\theta_{ps} = tan^{-1}(x/h)$ for pre-shock disc, i.e. for $x > x_s$. Moreover,

$$\mathcal{K}_0 = \frac{1.3\times10^{38}\ell_s\sigma_T}{2\pi cm_pA_sGM_\odot} \qquad \text{and,} \qquad \mathcal{J}_0 = \frac{2.93\times10^{34}e^4\mu_m^2\beta\sigma_T\dot{m}^2}{3\pi m_e^4c^2sec\theta_{ps}\gamma^{5/2}G^2M_\odot^2} \tag{3.31}$$

where, $\dot{m}$ is the accretion rate in units of Eddington accretion rate, σ_T is Thomson scattering cross section, μ_m is mean molecular weight of the plasma, m_p is the proton mass, m_e is the electron mass and $M_\odot$ is the solar mass. It is to be noted that the pre-shock radiation would depend on the product $\beta\dot{m}^2$. It is interesting to know that, the post-shock region by virtue of its geometry will block some of the pre-shock photons to the base of the jet, an effect coined as the shadow effect of the post-shock disc (Chattopadhyay et al. 2004; Chattopadhyay 2005) That is to say, if the height of the jet is $y_j < y_{jl}$, then $\mathcal{E}_{r_jps} = \mathcal{F}_{r_jps} = \mathcal{P}_{r_jps} = 0$, where

$$y_{jl} = h_s - \frac{h_{inj}-h_s}{x_{inj}-x_s}(x_s-x_j), \tag{3.32}$$

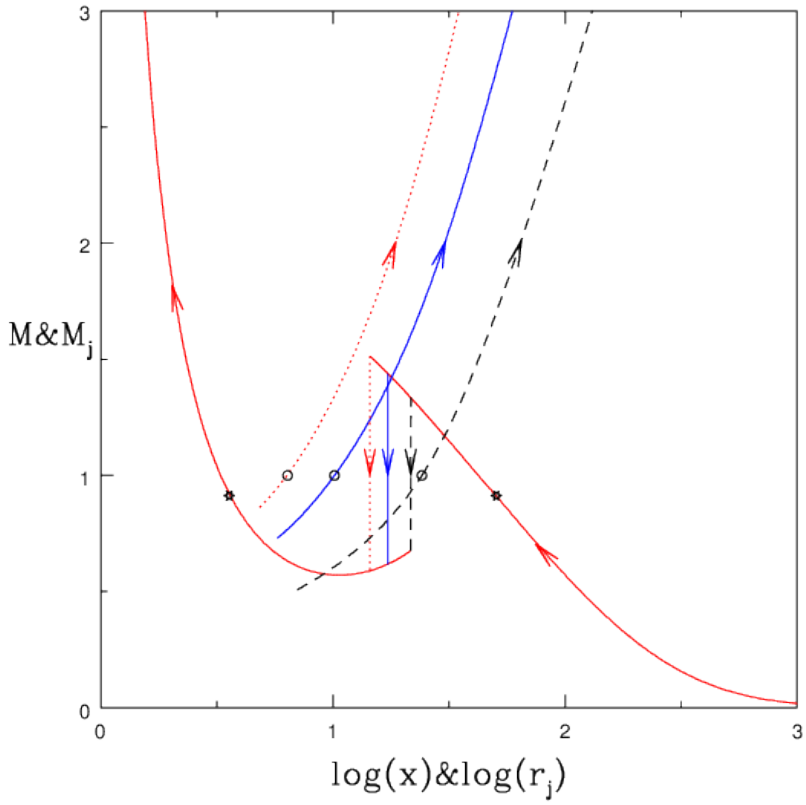

Figure 3.8: Accretion-ejection with Mach number - Accretion Mach number (M) and jet Mach number (M_j) with radial distance x and jet streamline r_j in log scale, are shown in the plot. Open circle represents the critical points of jets and star marks for accretion solutions, while arrows show flow directions. Solid curve (red) with inward arrows is accretion solution for parameters $E = 3.3 \times 10^{-3}$, $\lambda_0 = 1.353$, $\alpha = 0.1$. The post shock disc generate jets. Each jet curve represents M_j vs $log(r_j)$ for parameters $\ell_s = 0.0$ ($\ell = 0.0386$) (dashed, black), $\ell_s = 0.1$ ($\ell = 0.151$) (solid, blue), and $\ell_s = 0.2$ ($\ell = 0.274$) (dotted, red). The shocks are shown by vertical jumps (line style and color corresponds to that of the jet it generates). The parameter $\beta\dot{m}^2 = 0.01$ is kept constant. Kumar et al. (2014).

here, h_{inj} & x_{inj} are height and radius at outer edge of the disc. Additionally due to the shadow effect, the inner edge of the pre-shock disc as seen by an observer at some height y_j will be,

$$x_i = -\frac{x_s y_j}{h_s - y_j - x_s cot\theta_{ps}}$$

we use $\beta\dot{m}^2$ as a supplied parameter to calculate ℓ_{ps}. Also we use ℓ_s initially as a parameter (except figs. 3.13 and 3.14) in order to understand the effect of the relative proportions of radiation coming from different parts of disc on the ejected jet, but finally we will use the relation ℓ_s/ℓ_{ps} as a function of x_s (see Appendix A), to compute ℓ_s from the pre-shock radiation, and solve the accretion-ejection solution.

In Figs. 3.7 a-d, all the plots are generated for a disc characterized by $(E, \lambda_0, \alpha, \Gamma) = (3.5 \times 10^{-3}, 1.5435, 0.02, 1.4)$, which generates a shock at $x_s = 15.18$. In Fig. 3.7 a, I_{ps} is plotted as a function of x, starting from x_s outwards. In Fig. 3.7 b, we plot $\mathcal{E}_{r_j s}/\mathcal{K}_0$ (solid, black), $\mathcal{F}_{r_j s}/\mathcal{K}_0$ (dotted, blue) and $\mathcal{P}_{r_j s}/\mathcal{K}_0$ (dashed, red), the radiation moments due to the post-shock disc. In Fig.3.7 c, we plot $\mathcal{E}_{r_j ps}/\mathcal{J}_0$ (solid, black), $\mathcal{F}_{r_j ps}/\mathcal{J}_0$ (dotted, blue) and $\mathcal{P}_{r_j ps}/\mathcal{J}_0$ (dashed, red), the radiation moments due to the pre-shock disc. The shadow effect of the post-shock disc is clearly shown in the figure. In Fig.3.7 d, we plot $\mathcal{E}_{r_j}$ (solid, black), $\mathcal{F}_{r_j}$ (dotted, blue) and $\mathcal{P}_{r_j}$ (dashed, red) taking equal post-shock and pre-shock luminosities, $\ell_s = \ell_{ps} = 0.4$, respectively. From the above figures it is clear that radiative moments from the post shock region peaks at a height closer to the black hole and the moments from the pre-shock disc peaks typically at a distance few times larger. However, the space dependent parts of the moments (Figs.3.7b-c) shows that the moments of radiation from the pre-shock disc is typically an order of magnitude weaker than those due to the post-shock disc. However, the second distinct bulge in Fig.3.7 d shows, if the pre-shock luminosity is comparable to post-shock luminosity then the radiation moments peaks at two places, and hence presents a prospect for multi-stage acceleration scheme for the jets.

3.4.2 Accretion-ejection solutions:

In Kumar & Chattopadhyay (2013) we have shown in details various cases of accretion solutions, and also have shown that post shock disc naturally produces bipolar outflows. Presently, we discuss only the shocked accretion solution. The accretion solutions are characteristic by flow parameters like the grand energy E, the specific angular

momentum at the horizon λ_0 (conversely, λ_{inj} at the outer edge of the disc) and the viscosity parameter α. The jet is launched from the disc with the specific energy ($\mathcal{E}_j$ and angular momentum (λ_j) of the post-shock disc at the jet launch site (r_b). We also compute the moments of radiation fields ($\mathcal{E}_{r_j}$, $\mathcal{F}_{r_j}$, $\mathcal{P}_{r_j}$) above the disc, and are used to accelerate the jets. The pre-shock disc radiation depends on $\beta\dot{m}^2$, where, β is the ratio of the magnetic and the gas pressure and $\dot{m}$ is the accretion rate in units of Eddington rate. In order to find the effect of post-shock radiation and pre-shock radiation on jet acceleration, the post-shock luminosity ℓ_s and $\beta\dot{m}^2$ (conversely, ℓ_{ps} the pre-shock luminosity) are supplied as independent parameters. However, since post-shock radiation is produced by inverse-Comptonization of self generated and intercepted photons from the pre-shock disc, we compute the post-shock radiation self-consistently by employing the techniques of Chakrabarti & Mandal (2006). And in Figs. (3.13 - 3.15) the jets are accelerated by self consistent estimation of radiation field, both from pre and post-shock discs.

3.4.2.1 Effect of post-shock radiation on jet acceleration

The radiations produced from accretion is governed by the solution. However, we will now treat the post-shock luminosity as a parameter just to see how it affects the jet acceleration. The accretion Mach number $M = v/a$ with $log(x)$ is plotted for the parameters $E = 3.3 \times 10^{-3}$, $\lambda_0 = 1.353$, $\alpha = 0.1$, in Fig.3.8 . We first consider $\ell_s = 0$ and $\beta\dot{m}^2 = 0.01$, the shock is at $x_s = 21.546$ (vertical dashed, black), and drives bipolar outflow, where the jet Mach number M_j (dashed, black) is plotted with $log(r_j)$, and the mass outflow rate is $R_{\dot{m}} = 0.032$ and the sonic point of the jet is at $r_{jc} = 24.160$. Radiation field from the accretion disc deposit its momentum and accelerate the shock generated jets. Assuming $\ell_s = 0.1$ for same set of accretion boundary condition, accretion-ejection solution is computed. The shock is found to be at $x_s = 17.92$ (solid, blue) and the jet M_j distribution (solid, blue) has a sonic point at $r_{jc} = 9.59$ and $R_{\dot{m}} = 0.046$. The total luminosity for this case is $\ell = (\ell_s + \ell_{ps}) = 0.151$ ($\ell_s = 0.1$). Keeping $\beta\dot{m}^2$ same, we increase $\ell_s = 0.2$, so the total luminosity increases to $\ell = 0.274$, The accretion-ejection solution shows that the mass outflow increases to $R_{\dot{m}} = 0.058$ and the shock in accretion decreases to $x_s = 14.4$ (dotted, red). In this case too, due to the increase of radiation, the sonic point decreases to $r_{jc} = 6.36$, indicating stronger jet. It is interesting to note that, the pre-shock luminosity increases even though $\beta\dot{m}^2$ is

kept constant, because, with the decrease in x_s, the size of the pre-shock disc increases.

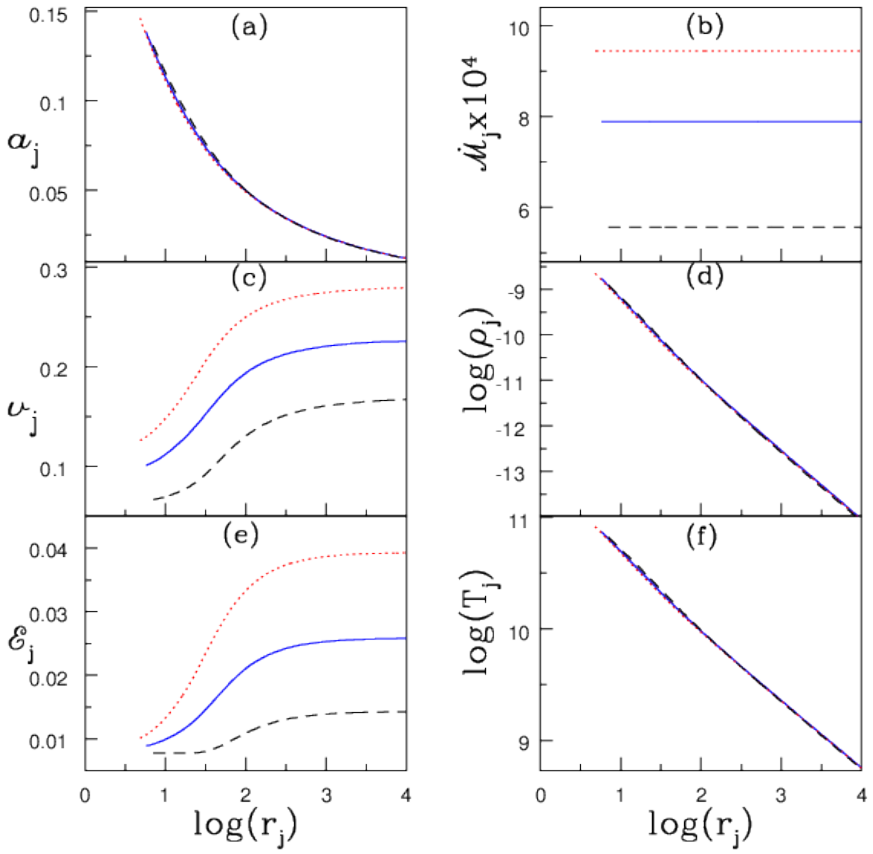

Figure 3.9: Effect of post-shock luminosity on jet flow variables - Jet flow variables like (a) sound speed a_j, (b) entropy-accretion rate $\dot{\mathcal{M}}_j$, (c) jet velocity v_j, (d) density ρ_j, (e) specific energy $\mathcal{E}_j$, and (f) temperature T_j are plotted with $log(r_j)$. The disc, radiation parameters, the line colours and line styles are same as Fig. 3.8. Kumar et al. (2014).

The jet solutions are explored in more details in the following figure. Jet variables a_j (Fig.3.9 a), $\dot{\mathcal{M}}_j$ (Fig.3.9 b), v_j (Fig.3.9 c), ρ_j (Fig.3.9 d), $\mathcal{E}_j$ (Fig. 3.9e) and T_j (Fig.3.9f) are plotted with $log(r_j)$. Each curve corresponds to $\ell_s = 0$ (dashed, black), $\ell_s = 0.1$ (solid, blue), and $\ell_s = 0.2$ (dotted, red), and which are exactly the same cases of jet solutions as in Fig. 3.8. The increase in ℓ_s, accelerates the jets further, and therefore increases $R_{\dot{m}}$, this in turn decreases the post-shock pressure and the location of the shock front moves close to the horizon. As a result the jet base moves closer. At

a given r_j, we find v_j is higher for higher ℓ_s, but difference in a_j or T_j are imperceptible. This shows, that enhanced jet acceleration is due to the radiative momentum deposition onto the jets and not due to conversion of thermal energy to the kinetic one. Since higher ℓ_s accelerate the jet, the sonic point is formed closer to the horizon. Higher ℓ_s not only means faster jet, but also a jet with higher entropy (Fig.3.9 b).

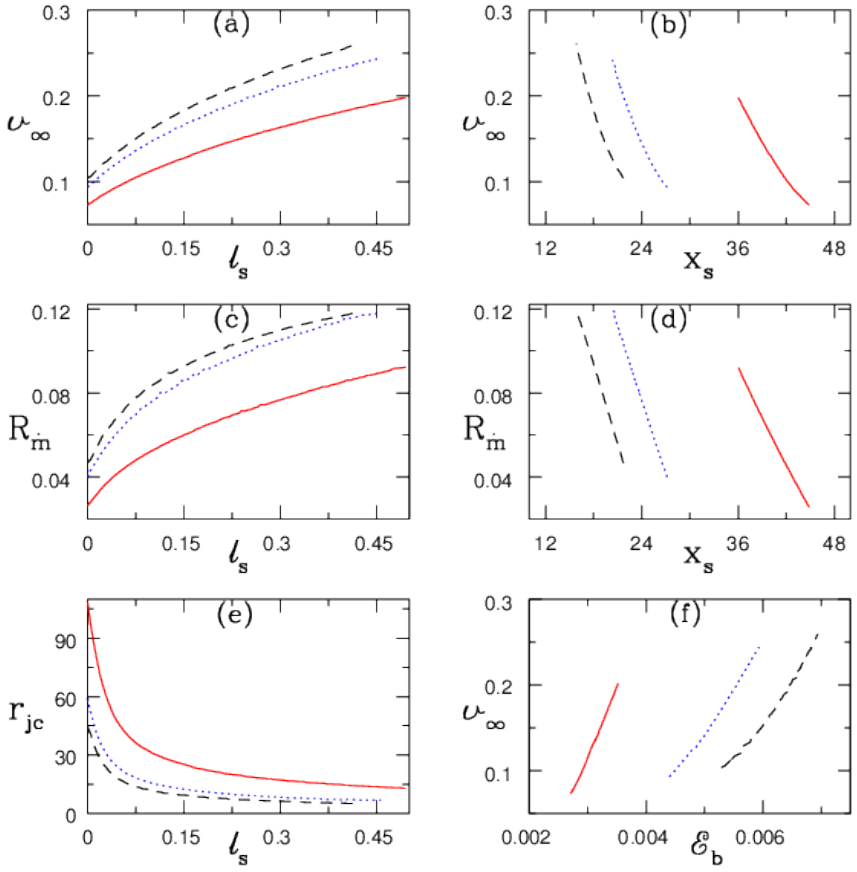

Figure 3.10: Effect of post-shock luminosity - Jet terminal velocity v_∞ is plotted with ℓ_s (a), with x_s (b), and with $\mathcal{E}_b$ (f). $R_{\dot{m}}$ is plotted with ℓ_s (c) and x_s (d). Moreover, r_{jc} is plotted with ℓ_s (e) too. The accretion solution corresponds to disc parameters $E = 0.001$ and $\lambda_{inj} = 70.6$ at disc outer boundary $x_{inj} = 10^4$ and keeping pre-shock luminosity is $\ell_{ps} = 0.0$. Each curve correspond for $\alpha = 0.04944$ (solid, red), 0.049887 (dotted, blue), and 0.050113 (dashed, black). Kumar et al. (2014).

The jet terminal speed is defined as $v_\infty = v$ (at $r_j \rightarrow$ large) where $dv_j/dr_j \rightarrow 0$. As shown in Figs. 3.9, v_∞ increases appreciably with the increase of ℓ_s and ℓ_{ps}, for a given value of disc viscosity parameter α. We would like to see whether this behaviour of v_∞

holds true for a range of α. In Fig. 3.10a, v_∞ is plotted with ℓ_s, in Figs. 3.10b & 3.10f, v_∞ is plotted with x_s and the jet base specific energy $\mathcal{E}_b$. And $R_{\dot{m}}$ is plotted with ℓ_s (Fig.3.10 c) and x_s (Fig.3.10d). Each curve correspond for $\alpha = 0.04944$ (solid, red), 0.049887 (dotted, blue), and 0.050113 (dashed, black). All these figures are generated with outer boundary condition $E = 0.001$ and $\lambda_{inj} = 70.6$ at $x_{inj} = 10^4$. It is clear that v_∞ increases with ℓ_s at a given value of α, as well as, increases with α at a given ℓ_s. Since x_s moves closer with the increase of both ℓ_s and α, the jets are launched with higher $\mathcal{E}_b$, which in turn increases v_{jb}. This is also the reason that the relative mass outflow rate $R_{\dot{m}}$ increases with the increase of both ℓ_s and α. Since v_{jb} increases with ℓ_s and α, therefore the jets become supersonic at a distance nearer to the jet base, i.e. r_{jc} decreases with the increase of ℓ_s (Fig.3.10e).

3.4.2.2 Effect of pre-shock radiation on jets

The effect of radiation from pre-shock disc as it impinges on the jet is illustrated through Figs.3.11 b-f. In Fig.3.11 a, the Mach number M of the accretion solution is plotted with $log(x)$ for disc parameters $E = 3.3 \times 10^{-3}, \lambda_0 = 1.353,$ and $\alpha = 0.1$. The shock is at $x_s = 17.92$. We choose $\ell_s = 0.1$, but the pre-shock radiation is changed by varying $\beta\dot{m}^2$. The solutions correspond to $\beta\dot{m}^2 = 0.01$ ($\ell = 0.151$) (solid, red), $\beta\dot{m}^2 = 0.02$ ($\ell = 0.202$) (dotted, blue), and $\beta\dot{m}^2 = 0.04$ ($\ell = 0.303$) (dashed, black). The post-shock disc actually hides the base of the jet from most of the radiation from the pre-shock disc, while shines its own light onto the jets (see Fig. 3.6). As a result, if the post-shock radiation remains unaltered and the jet sonic point is formed in the portion of the funnel like region where pre-shock radiation is negligible, then the jet base velocity v_{jb}, the jet base r_{jb} or the jet base properties are likely to remain roughly same, keeping the massloss rate unaltered. Consequently, the change in the accretion shock is imperceptible (Fig.3.11a). All the jet variables closer to the base, e.g. M_j (Fig. 3.11b), v_j (Fig.3.11c), $\mathcal{E}_j$ (Fig.3.11e), and T_j are indistinguishable, while they differ from each other in the supersonic region, where the interaction of pre-shock radiation with the jet is significant too. It is to be remembered, that the temperature plotted here is the single temperature of the outflow. The corresponding electron temperature should be about two orders of magnitude less. However, the entropy accretion rates $\dot{\mathcal{M}}$ (Fig.3.11 d) are distinguishable even at the base. Once again it is clear from the temperature plot, that radiative driving is significant. It is also interesting to note from Figs. 3.8 -

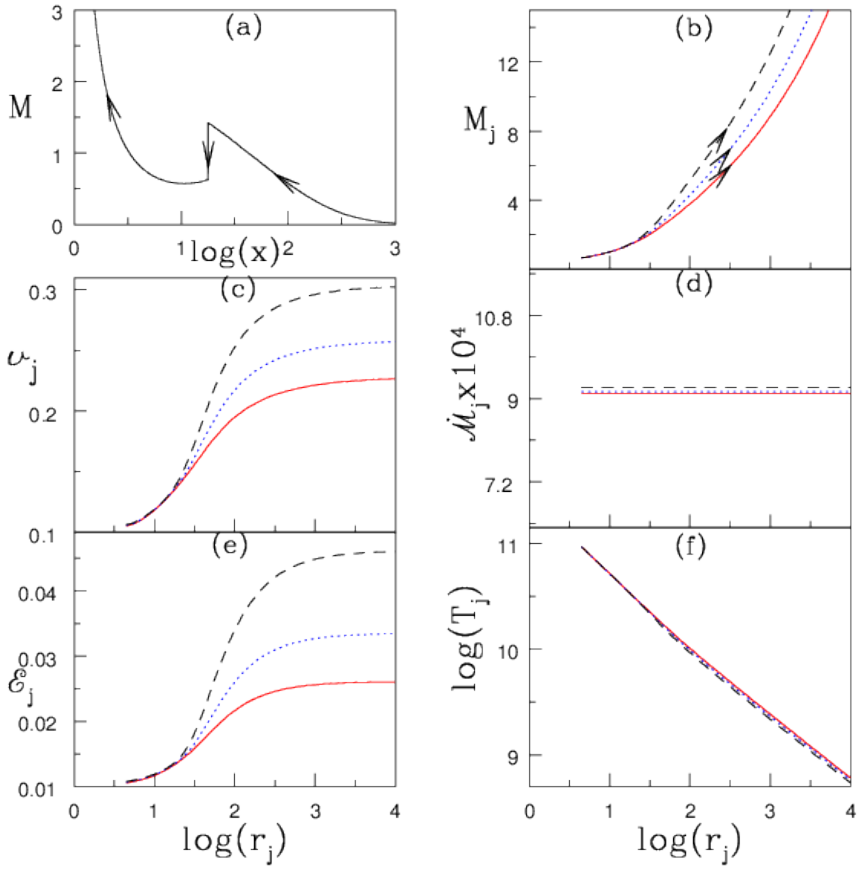

Figure 3.11: Effect of pre-shock luminosity on jet flow quantities - (a) Accretion Mach Number M with $log(x)$, and (b) jet Mach number M_j, (c) jet velocity v_j, (d) jet entropy rate $\dot{\mathcal{M}}_j$, (e) specific energy $\mathcal{E}_j$, and (f) temperature T_j plotted with $log(r_j)$ for the disc parameters $E = 3.3 \times 10^{-3}, \lambda_0 = 1.353, \alpha = 0.1$, and shock forms at $x_s = 17.92$. Each curve is for $\beta\dot{m}^2 = 0.01$ ($\ell = 0.151$) (solid, red), $\beta\dot{m}^2 = 0.02$ ($\ell = 0.202$) (dotted, blue), and $\beta\dot{m}^2 = 0.04$ ($\ell = 0.303$) (dashed, black) and $\ell_s = 0.1$ is kept constant. Each jet solutions have critical points at $r_{jc} \sim 9.59$ and mass outflow rates, $R_{\dot{m}} \sim 0.046$. Kumar et al. (2014).

3.9, that increasing ℓ_s, would result in faster jets, with higher $R_{\dot{m}}$ and lower jet sonic point (r_{jc}). While increasing the pre-shock radiation also results in faster jets, but with almost no change in $R_{\dot{m}}$ and r_{jc}. Since relative mass outflow rates affects the accretion solutions (Eq. 3.23), so the feed-back effect of the jet on the disc due to ℓ_s might be more significant than that due to ℓ_{ps}.

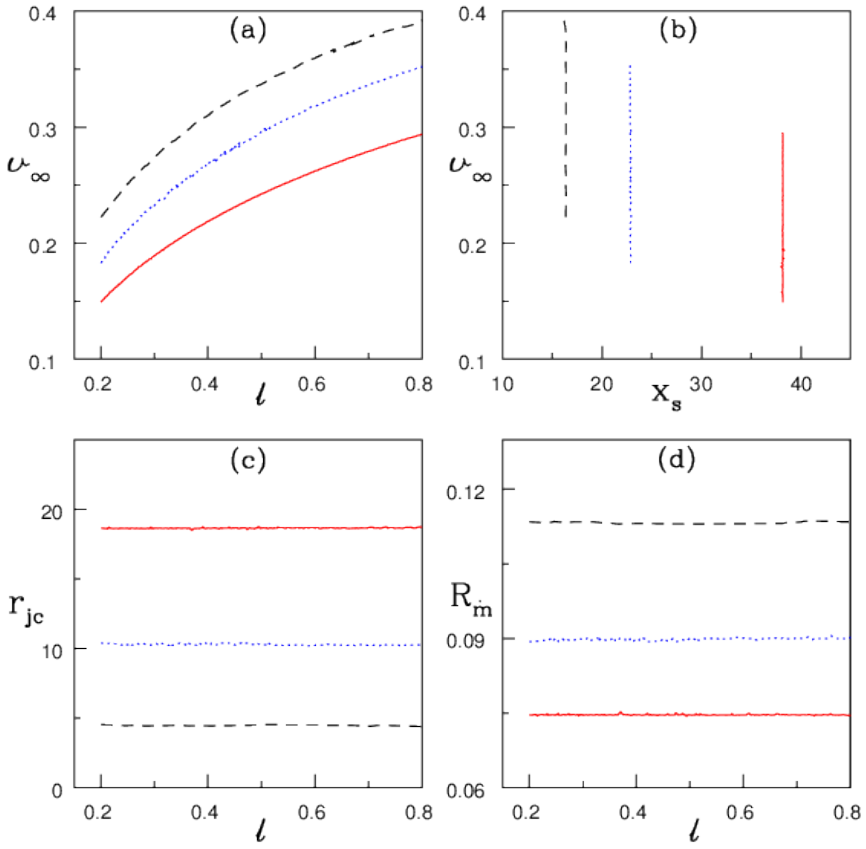

Figure 3.12: Effect of pre-shock luminosity - Terminal jet velocity v_∞ with total disc luminosity ℓ, (b) shock locations x_s, and (c) r_{jc} is plotted with ℓ and (d) $R_{\dot{m}}$ is plotted with ℓ. The disc parameters are $E = 0.001$ and $\lambda_{inj} = 70.6$ at disc outer boundary $x_{inj} = 10^4$. and keeping post-shock luminosity is $\ell_s = 0.2$ but varying pre-shock luminosity(ℓ_{ps}). Each curve are for viscosity parameter $\alpha = 0.04944$ (solid, red), 0.049887 (dotted, blue), and 0.050113 (dashed, black). Kumar et al. (2014).

In Figs. 3.12 a-d, we investigate how ℓ_{ps} affects the jet solutions for a variety of α, but for the same outer boundary condition as in Fig. 3.11 with constant $\ell_s = 0.2$. In Fig. 3.12a, we plot v_∞ as a function of ℓ, where each curve represent disc solutions

with $\alpha = 0.04944$ (solid, red), 0.049887 (dotted, blue), and 0.050113 (dashed, black). In all these plots ℓ_{ps} varies from $0 \rightarrow 0.6$. Due to radiative driving, v_∞ increases with ℓ, and at a given ℓ, it increases with α. As has been explained in connection to the previous figure, increasing α for a fixed outer boundary decreases x_s, which means the jet base energy $\mathcal{E}_b$ increases, resulting in faster jet. However, since the pre-shock disc primarily shines radiation on the supersonic part of the jet, therefore ℓ_{ps} has marginal effect on r_{jc}, and v_{jb}. Therefore, $R_{\dot{m}}$ is almost constant with the change of ℓ_{ps} (Fig. 3.12 d), which in turn keeps x_s almost unchanged (Fig. 3.12 b), and the jet sonic point r_{jc} also remains unchanged (Fig. 3.12 c). In other words, we may conclude, that the radiation from the inner torus of the accretion disc accelerate the jet, and also increases net mass-loss. On the other hand, radiation from pre-shock disc or the outer disc, accelerates the jet appreciably, although, has almost no effect on $R_{\dot{m}}$. Therefore, in the second case we may obtain jets with higher kinetic luminosity. This conclusion is valid for any value of α which admits accretion shock.

3.4.2.3 Radiative driving of jets with computed post-shock and pre-shock radiations

Having investigated the role, the pre-shock and post-shock radiation may have on jets, we actually calculate the ℓ_s from ℓ_{ps}. In appendix (A), we have discussed the different radiation processes in a general radiative transfer model (Chakrabarti & Mandal 2006). From the accretion disc spectrum, we calculate the ratio of post-shock to pre-shock luminosity (ℓ_s/ℓ_{ps}) using the viscous transonic solution. We then use a fitting formula of ℓ_s/ℓ_{ps} (Equation A.1) to calculate the ratio at any given shock location (x_s). In (Fig. A.1 b), a typical ℓ_s/ℓ_{ps} dependence on x_s is obtained where the dots are the data points from model (Chakrabarti & Mandal 2006) and solid line represents the fitting function. We assume that the behaviour of this ratio with shock location is generic. The procedure for calculating ℓ_s is as follows — for a given set of values of E, λ_0, α, the accretion solution shows a shock at x_s and a bipolar outflow with some $R_{\dot{m}}$. We then calculate ℓ_{ps} (Equation 3.27) by supplying $\beta\dot{m}^2$ and the density and temperature distribution between x_{inj} and x_s. We use the fitting formula of ℓ_s/ℓ_{ps} (Equation A.1) to calculate ℓ_s. Using these the jet solution is obtained. All the solutions presented in Figs. (3.8 - 3.12), we have solved the accretion ejection solution with the following fluid parameters E, λ_0 (at the horizon, or equivalently, λ_{inj} at the outer boundary), α, and

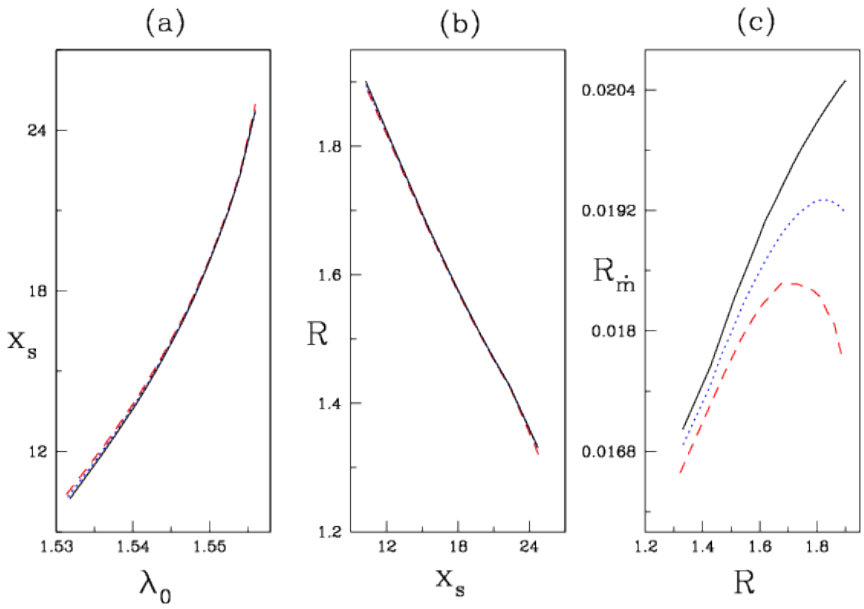

Figure 3.13: Variation of shocks and outflow rate - (a) Shock location x_s is plotted with angular momentum at the horizon (λ_0), (b)Compression ratio R with x_s and (c) mass outflow rate ($R_{\dot{m}}$) versus R are plotted for flows with $E = 0.004$, $\alpha = 0.01$. Various plots represent thermally driven flow (dashed, red), and radiatively driven outflows for $\beta\dot{m}^2 = 0.005$ (dotted, blue) and $\beta\dot{m}^2 = 0.01$ (solid, black). Kumar et al. (2014).

in addition the radiation parameters ℓ_s and $\beta\dot{m}^2$ (equivalently ℓ_{ps}). Now, following the procedures described in appendix (A), we reduce one parameter, namely, ℓ_s. In Fig. 3.13 a, we plot x_s with λ_0, in fig. 3.13 b, we plot the compression ratio R with x_s, and in fig. 3.13c, mass outflow rate $R_{\dot{m}}$ with the compression ratio R. All the plots are for accretion disc parameters $E = 0.004$, $\alpha = 0.01$, and various results has been obtained by varying λ_0. The curves are for thermally driven jet (i.e. $\beta\dot{m}^2 = 0$; dashed, red), and thermal plus radiatively driven jets (i.e. $\beta\dot{m}^2 = 0.005$; dotted blue, and $\beta\dot{m}^2 = 0.01$; solid, black). This shows that as the compression at the shock increases, it forces more matter into the jet channel. Although R increases as x_s decreases, but smaller post-shock region means less matter can be driven as jets, so $R_{\dot{m}}$ maximizes at some intermediate R. It has also been shown earlier (Chakrabarti 1999; Das et al. 2001), that for $R = 1$ i.e. no shock, $R_{\dot{m}} \sim 0$ i.e. for no shock there is no outflow. In Figs. 3.14 a-l, we have plotted accretion and jet solutions for various α and ℓ_{ps}. All the accretion solutions (M with $log(x)$) are for outer boundary parameters E, $\lambda_{inj} = 0.001$, 18.592 at the outer boundary $x_{inj} = 10^4$. The viscosity parameters are $\alpha = 9.115 \times 10^{-3}$ (3.14a), 9.315×10^{-3} (3.14d), 9.626×10^{-3} (3.14g), and 9.875×10^{-3} (3.14j). The vertical jumps show the location of accretion shocks, and they are at $x_s = 125.896$ (3.14 a), 45.9986 (3.14 d), 18.2871 (3.14g), and 8.5741 3.14(j). The jet solutions corresponding to these accretion solutions, are presented by M_j 3.14(b, e, h, k) and v_j 3.14(c, f, i, l). As α increases x_s decreases, therefore increasing the pre-shock disc. Moreover, with decreasing x_s, the post-shock disc becomes smaller and hotter. So as x_s decreases, initially both ℓ_s & ℓ_{ps} will increase, but at around $x_s \sim 100$, further decrease of x_s will reduce ℓ_s/ℓ_{ps} and significantly increase ℓ_{ps} (Fig. A.1 b). In Figs. 3.14 a, d, g, j, increase of α, causes a shift of $x_s = 125.896 \rightarrow 8.5741$. Consequently, ℓ_{ps} increases from $0.0054 \rightarrow 0.2337$. The resulting jets are accelerated and the terminal velocity increases from $v_\infty = 0.0534 \rightarrow 0.3519$ as shock shifts from $x_s = 125.896 \rightarrow 8.5741$, with the corresponding change in luminosity. By considering the relative proportions of post-shock and pre-shock radiations, decrease of x_s with increasing α resembles the disc to move from hard state to hard intermediate state, and simultaneously the jet becomes stronger and faster (both v_∞ and $R_{\dot{m}}$ increases).

In Fig. 3.15a-c, we show the comparison of shock parameter space ($E - \lambda_0$) of the accretion disc without massloss (dotted, red) and with massloss but disc parameter $\beta\dot{m}^2 = 0.001$ (long dashed, black) and $\beta\dot{m}^2 = 0.01$ (dashed, blue), and for various

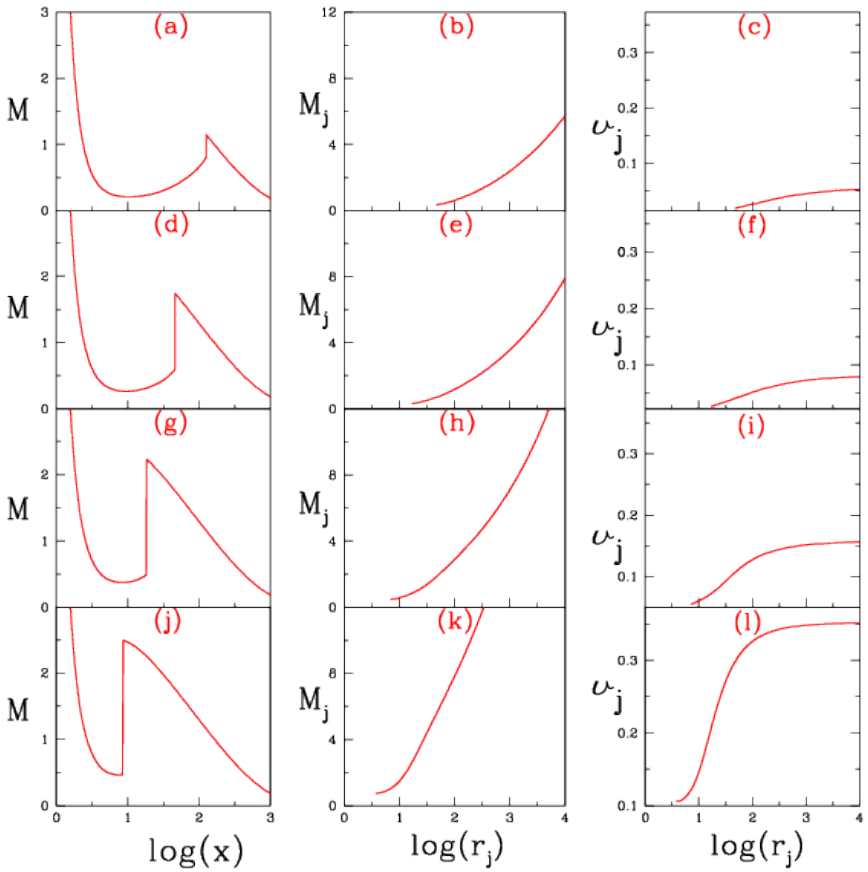

Figure 3.14: Stages of increasing jet strength - Variations of accretion Mach number M (a, d, g, and j) with $log(x)$, M_j (b, e, h, and k), and v_j (c, f, i, and l) with $log(r_j)$.The disc solutions are for parameters $E = 0.001, \lambda_{inj} = 18.592$ at outer boundary $x_{inj} = 10^4$, and for $\alpha = 0.009115$ (a-c), 0.009315 (d-f), 0.009626 (g-i), and 0.009875 (j-l). Plots (a-c) are characterized by (x_s, $R_{\dot{m}}$, ℓ_{ps}, ℓ_s = $125.8964, 0.0091, 0.0054, 0.0346$); for (d-f) ($x_s$, $R_{\dot{m}}$, ℓ_{ps}, ℓ_s = $45.9986, 0.0208, 0.0103, 0.0438$); for (g-i) ($x_s$, $R_{\dot{m}}$, ℓ_{ps}, ℓ_s = $18.2871, 0.0504, 0.0380, 0.0585$); and for (j-l) ($x_s$, $R_{\dot{m}}$, ℓ_{ps}, ℓ_s = $8.5741, 0.0991, 0.2337, 0.0948$), and the jet terminal velocities are v_∞ = $0.0534, 0.0793, 0.1566$ and 0.3519, respectively. Kumar et al. (2014).

viscosity parameter $\alpha = 0$ (Fig. 3.15a), $\alpha = 0.1$ (Fig. 3.15b) and $\alpha = 0.2$ (Fig. 3.15c). It is to be noted, that the bounded regions in $E - \lambda_0$ parameter space, show the parameters for steady state shocks to occur, but non-steady shocks still exist outside the bounded region. The parameter space shrinks when massloss is considered, because with massloss, the post-shock pressure decreases, and the entire range for which steady shock may have existed in absence of jets, will not be able to satisfy the momentum balance across the shock front. Moreover, shocks seem to exist for fairly high viscosity and in presence of massloss too.

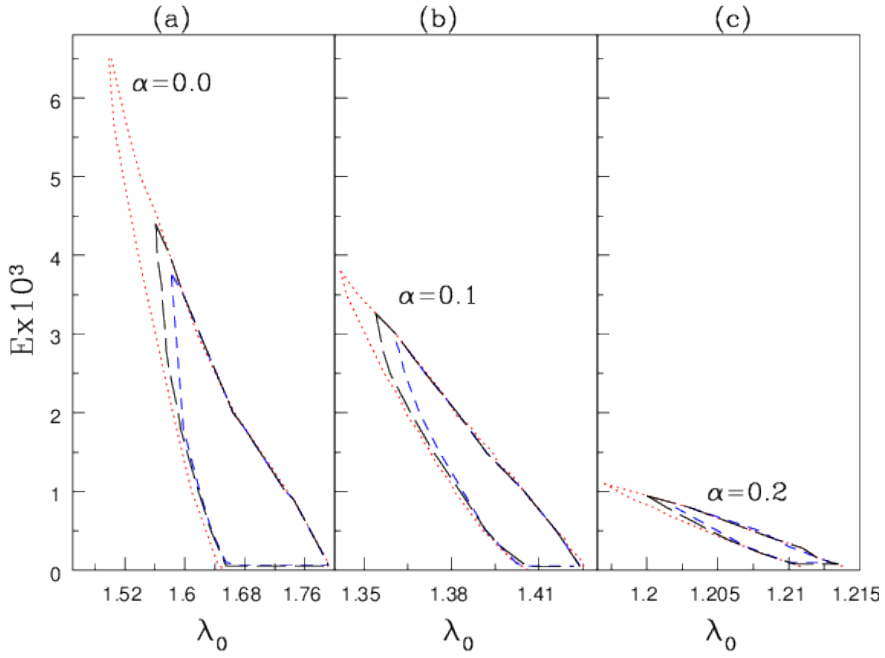

Figure 3.15: Comparison of SPS with and without outflow - Shock parameter space or $E - \lambda_0$ space for accretion, considered without massloss (dotted), and with massloss (dashed), and for $\alpha = 0$ (a), $\alpha = 0.1$ (b), and $\alpha = 0.2$ (c). Kumar et al. (2014).

3.5 Comparison of numerical simulation with analytical solutions

We have done the accretion studies with steady state hydrodynamics and predicted some of observational features. But variation of spectral state and evolution of QPOs are time dependent phenomena. So a time dependent study with the help of numerical simulation is a must. Now comparing the numerical result and the analytical is also important, since it serves two purposes. One, the numerical code needs to be tested with analytical result in order to check for viability of the code. And two,the analytical result is obtained under some simplifying assumptions like hydrostatic equilibrium along the vertical direction, axis-symmetry etc. A good match also validates the assumptions of the analytical solutions as well. In this section, we launch the simulations with the analytical solutions at the outer boundary and check how well the theoretical result agrees the numerical simulation.

In order to do that, we have used an axis-symmetric 2-dimensional cylindrical time-dependent hydrodynamic simulation code (Lee et. al. 2011). This code is based on Lagrangian Total Variation Diminishing (TVD) scheme and remap routine, which has employed to attain the high accuracy of capturing numerical shock, as well as, to handle the angular momentum accurately.

3.5.1 Basic equations

The conserved form of equations of motion (2.1-2.3) for viscous flow in 2-D cylindrical polar coordinates (r, ϕ, z) are written as

Continuity equation,

$$\frac{\partial \rho}{\partial t} + \frac{1}{r}\frac{\partial (r\rho v_r)}{\partial r} + \frac{\partial (\rho v_z)}{\partial z} = 0, \tag{3.33}$$

$x-$ component or radial momentum flux equation,

$$\frac{\partial (\rho v_r)}{\partial t} + \frac{1}{r}\frac{\partial (r\rho v_r^2)}{\partial r} + \frac{\partial (\rho v_r v_z)}{\partial z} + \frac{\partial p}{\partial r} = \rho f_r + \rho \frac{v_\phi^2}{r}, \tag{3.34}$$

$z-$ component or vertical momentum flux equation,

$$\frac{\partial (\rho v_z)}{\partial t} + \frac{1}{r}\frac{\partial (r\rho v_r v_z)}{\partial r} + \frac{\partial (\rho v_z^2)}{\partial z} + \frac{\partial p}{\partial z} = \rho f_z, \tag{3.35}$$

$\phi-$ component or azimuthal momentum flux equation,

$$\frac{\partial(\rho l)}{\partial t}+\frac{1}{r}\frac{\partial(r\rho v_r l)}{\partial r}+\frac{\partial(\rho v_z l)}{\partial z}=\frac{1}{r}\frac{\partial}{\partial r}\left(\mu r^3\frac{\partial}{\partial r}(\frac{l}{r^2})\right)+r\frac{\partial}{\partial z}\left(\mu\frac{\partial}{\partial z}(\frac{l}{r})\right), \tag{3.36}$$

Energy generation equation,

$$\begin{aligned}&\frac{\partial E}{\partial t}+\frac{1}{r}\frac{\partial(rv_rE)}{\partial r}+\frac{1}{r}\frac{\partial(rpv_r)}{\partial r}+\frac{\partial(pv_z)}{\partial z}+\frac{\partial(Ev_z)}{\partial z}\\&\quad=\frac{1}{r}\frac{\partial}{\partial r}\left(\mu r^2v_\phi\frac{\partial}{\partial r}(\frac{l}{r^2})\right)+\frac{\partial}{\partial z}\left(\mu v_\phi\frac{\partial}{\partial z}(\frac{l}{r})\right)-\rho v_rf_r-\rho v_zf_z,\end{aligned} \tag{3.37}$$

where $E=e_t/\rho,\ l,\ f_r=-\partial\phi/\partial r$ and $f_z=-\partial\phi/\partial z$ are total specific energy, specific angular momentum of the flow, psuedo-Newtonian gravitational force in radial direction and in vertical direction, respectively. Other variables are having their usual meaning.

3.5.2 The code

One of the most demanding tasks in carrying out numerical simulations including shock structures is to capture shocks sharply. The upwind finite-difference schemes on an Eulerian grid has been known to achieve the shock capture strictly. However, since the angular momentum of equations (3.33) (3.37) are not treated as a conserved quantity in such Eulerian codes, we built a new code, which is called Lagrangian TVD. The new designed code can preserve the angular momentum completely because Lagrangian concept is used, and it can also guarantee the sharp reproduction of discontinuities because of the TVD scheme (Harten 1983; Ryu et al. 1993) is applied (see, Lee et. al. 2011, for details). The calculation in the viscous angular momentum transfer is updated through an implicit method, assuring it is free from numerical instabilities related to it. But the viscous heating without cooling is updated with a second order explicit method, since it is less subject to numerical instabilities.

3.5.2.1 Hydrodynamic part in multi-dimensional geometry

To begin with, the hydrodynamic part in Lagrangian step and remap, which is consisted of plane parallel and cylindrical geometry, is solved. The conservative form with mass coordinate equations (3.33) (3.37) in the Lagrangian grid can be written as

$$\frac{d\tau}{dt}-\frac{\partial(r^\beta v_r)}{\partial m}=0, \tag{3.38}$$

$$\frac{dv_r}{dt} + r^\beta \frac{\partial p}{\partial m} = 0, \tag{3.39}$$

$$\frac{dl}{dt} = 0, \tag{3.40}$$

$$\frac{dE}{dt} + \frac{\partial (r^\beta v_r p)}{\partial m} = 0 \tag{3.41}$$

where τ and E are the specific volume and the specific total energy, respectively, that are related to the quantities used in equations (3.33) (3.37) as

$$\tau = \frac{1}{\rho}, \qquad E = \epsilon + \frac{v_r^2}{2}. \tag{3.42}$$

The mass coordinate related to the spatial coordinate is

$$dm = \rho(r) r^\beta dr, \tag{3.43}$$

and its position can be followed with

$$\frac{dr}{dt} = v_r(m, t). \tag{3.44}$$

where, the value of β presents the calculation in geometrical geometry, i.e., $\beta = 0$ means the Cartesian coordinate system, while $\beta = 1$ means cylindrical geometry. Since the equations (3.38), (3.39), (3.41) show a hyperbolic system of conservation equation, upwind schemes are applied to build codes that advance the Lagrangian step using the Hartens TVD scheme (Harten 1983). Hence, $\beta = 1$ and 0 are used for the calculation in the left part of equation (3.34) and (3.35), respectively. The detailed explanations of Lagrangian TVD and remap are given in Lee et al. (2011). The centrifugal force, gravity, and viscosity terms are treated separately and the angular momentum in Equation (3.40) does not need to be updated in Lagrangian step since it is preserved in the absence of viscosity. However, the angular momentum transfer in the viscous flow is solved implicitly, while the viscous heating of equation (3.36) is solved explicitly, respectively.

3.5.2.2 Viscosity part

Viscosity plays an important role in transferring the angular momentum outwards and it allows the matter to accrete inwards around a black hole. The angular momentum transfer in equation (3.36) is described by the viscosity parameter given in (Shakura &

Sunyaev 1973).Since the terms for the angular momentum transfer of radial and vertical direction in Equation (3.36) are linear in l, it is possible to solve implicitly. Substitution of $(l^{new} + l^{remap})/2$ for l, Equation (3.36) without the advection term becomes

$$a_i l_{i-1}^{new} + b_i l_i^{new} + c_i l_{i+1}^{new} = -a_i l_{i-1}^{remap} - (b_i - 2) l_i^{remap} - c_i l_{i+1}^{remap}, \tag{3.45}$$

forming a tridiagonal matrix. Here a_i, b_i and c_i are given with ρ, μ and r as well as $\triangle x$ and $\triangle t$. The tridiagonal matrix is solved properly for l^{new} with an appropriate boundary condition (Press et al. 1992). Another role of viscosity is to act as friction resulting in viscous heating. Here, the viscous heating energy is fully saved in the flow and increases entropy, since we ignore the cooling. Our experience with dealing with numerical experiments tells us that the explicit treatment for the calculation of the viscous heating does not cause any numerical problem. So, angular momentum transfer is solved implicitly, while frictional heating energy is solved explicitly.

3.5.3 Results

Here, we have tested for inviscid flows with shock-free and shocked solutions based on the analytical solutions of Kumar & Chattopadhyay (2013). The flows are supplied from the outer boundary and are absorbed at the inner edge of a black hole. The behavior of accreting matter around a black hole depends on the initial parameters of inflows, for instance, its specific energy and specific angular momentum (Chakrabarti 1989; Das et al. 2001; Kumar & Chattopadhyay 2013; Kumar et al. 2013, 2014; Kumar & Chattopadhyay 2014). Large angular momentum in the accretion flow is especially accompanied by shock that travels outward. We first start off with a small amount of specific angular momentum $1.48 r_g c$ and a heat capacity of $\Gamma = 1.4$, which corresponds to a "shock-free solution", and inputs are supplied from Kumar & Chattopadhyay (2013). Figure (3.16) shows the comparison of simulation results with analytical results, which represent sound speed, radial velocity, specific angular momentum, and density along the equatorial plane from top to bottom. As the analytical solution suggests, the results do not show any shock structure in the initial conditions. Figure (3.17) shows the density contour and velocity field, where the flow is very stable. Although the accretion flow hits the effective potential barrier which is called "funnel wall" (Molteni et al. 1996a), a part of the flow does not pile up behind it, and does not interact with

infalling matter because most of all the supplied matter is absorbed by the black hole in this simulation.

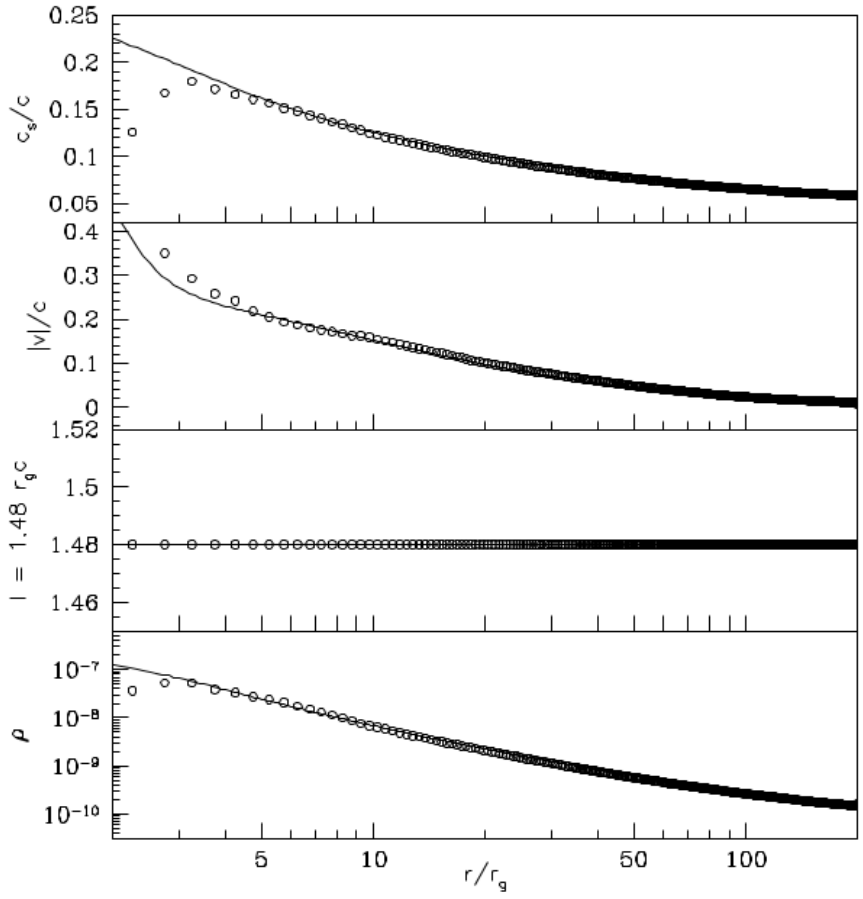

Figure 3.16: Shock free simulation and analytical solution - Test of the shock-free solution with $\Gamma = 1.4$ and $l = 1.48 r_g c$ under the pseudo-Newtonian potential. The solid lines represent the analytical solution, while the dots represent the numerical solution. The adiabatic sound speed c_s , radial velocity v_r , specific angular momentum l, and density ρ along the equatorial plane are shown from top to bottom. The injection radius $r_{inj} = 200 r_g$, and at r_{inj} the radial velocity $v_{bulk}(inj) = 6.9402 \times 10^{-3} c$ and sound speed $c_s(inj) = 5.9198 \times 10^{-2} c$ (Lee et al. to be submit).

However, if the initial conditions are different, for instance, if the specific angular momentum is $1.7 r_g c$, the centrifugal force is larger, and thus the fluid pressure along with the centrifugal force acts as a "brake" for the supersonic flow following it and undergoes a shock transition. Figure (3.18) shows the flow forming a shock along

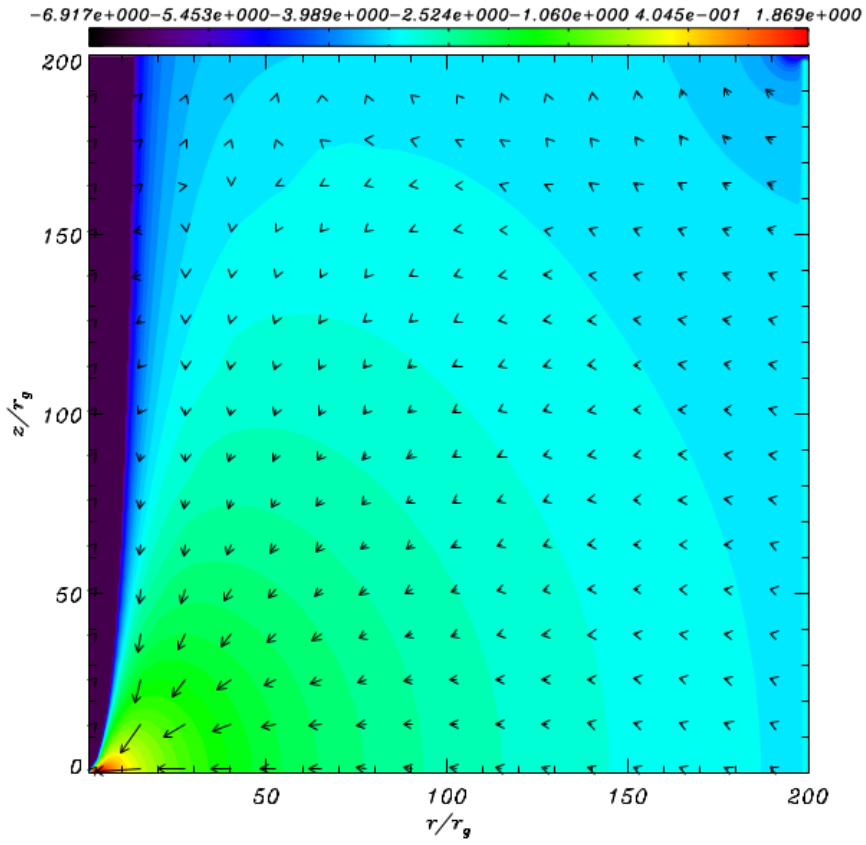

Figure 3.17: Bulk velocity field - Contour map and velocity field of the shock-free solution. The initial conditions are same as in Fig.(3.16) (Lee et al. to be submit).

the equatorial plane. The sound speed, radial velocity, specific angular momentum, and density are ordered from top to bottom, respectively. The solid lines show the analytical solution while the dots show numerical results. To mimic a realistic thin disk, the flow is injected from a radial distance of $200r_g$ and a scale height of $50r_g$ under the pseudo-Newtonian potential. The grid size is $200 \times 200r_g$ in 400×400 cells. The bulk velocity based on the analytical solution is divided into the radial and the vertical velocity in the cylindrical geometry. The mach number is about 4.17 at the outer boundary. The shock location of numerical calculation along the equatorial plane is about $17.25r_g$, while the shock location suggested from analytical solution is $20.18r_g$. The shock location seems to depend on back ground initial conditions in the multi-dimensional geometry. Although the shock location slightly deviates from the analytical solution, however the numerical shock location agrees reasonably well. The reason for the slight disagreement in shock location are many, but most importantly, due to the assumption of vertical equilibrium in the analytical solution, while the simulation is pure 2-dimensional simulation. Figure (3.19) shows the density contour and velocity field in top left and top right panel, respectively. The inflow matter hits the effective potential barrier and is piled up behind the barrier, where an accretion shock is formed. The shock in the bottom panel propagates outward and stops at a position of $17.25r_g$ after the time is about $1 \times 10^4 r_g/c$ (bottom). It is interesting to note that close to the horizon, while, angular momentum distribution agrees perfectly well, but the velocity, sound speed deviates a bit. This is again due to the limiting assumption of vertical equilibrium close to the horizon in the analytical ansatz, where, in reality black hole gravity do not allow such assumption.

In next we have added viscosity parameter (α) in the above inviscid solution. When the viscosity is turned on, the gas pressure increase due to viscous heat dissipation (equation, 3.37) and increases also the centrifugal force due to pile up of angular momentum (equation, 3.36) in the post-shock region and resulting the shock front recedes from $17.25r_g$ to $18.75r_g$ away from the black hole as in detail Fig. (3.20). And analytical solution shows also same result. If we compare with analytical results from Fig. (3.4) for shorter boundary (x_b) and lies in domain '2', shock front increases with increasing α. When x_b lies in the domain '1', the shock front decrease with increasing α. However, over all agreement is fantastic. The simulation code finds steady shock wherever the our analytical analysis predicts one, and the shock location also agrees

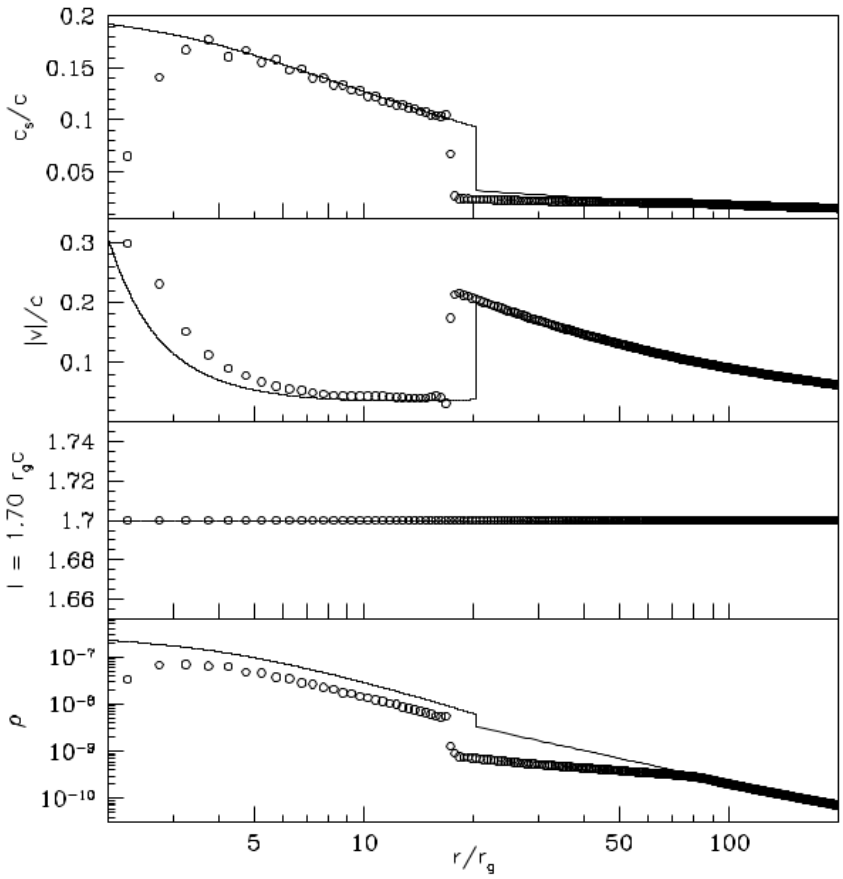

Figure 3.18: Shock simulation and analytical solution - Hydrodynamical accretion shock along the equatorial plane with $\Gamma = 1.4$ and $l = 1.7cr_g$. The sound speed, velocity, specific angular momentum, and density are shown from top to bottom. The solid lines and open circles represent the analytical solutions and the numerical results, respectively. The analytical shock location shows $20.18r_g$, while the numerical results present $17.25r_g$. The injection radius $r_{inj} = 200r_g$, and at r_{inj} the radial velocity $v_{bulk}(inj) = 6.2248 \times 10^{-2}c$ and sound speed $c_s(inj) = 1.4934 \times 10^{-2}c$ (Lee et al. to be submit).

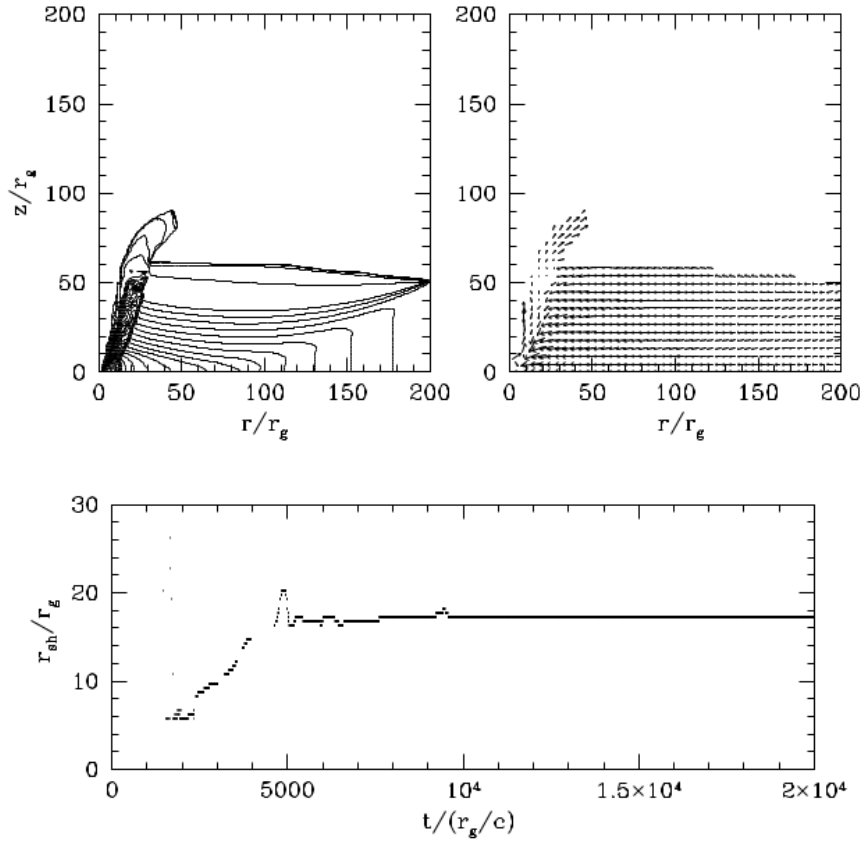

Figure 3.19: Precursor for outflow - Density contour map (top left) and velocity field (top right) of shocked solution. Stable shock loci (bottom) appear after $t = 10^4 r_g/c$. The initial conditions are the same as in Fig.(3.18) (Lee et al. to be submit).

reasonably well. We will use this code to make a time dependent study on jet states and QPO.

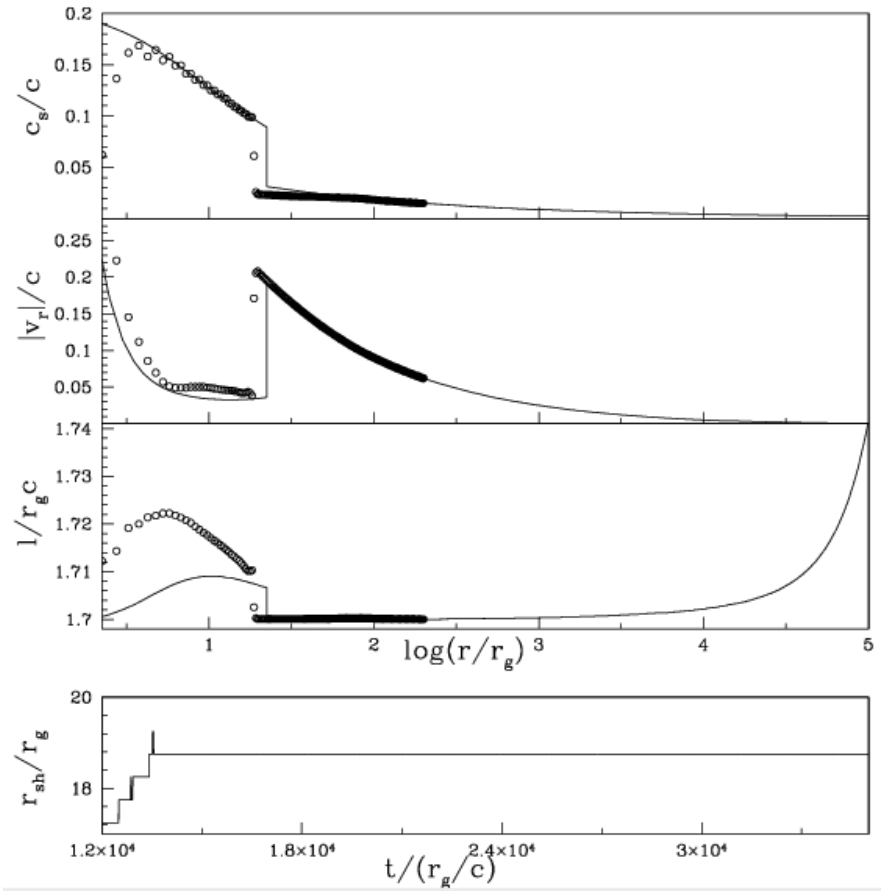

Figure 3.20: Shock simulation and analytical viscous solution - The sound speed, velocity, specific angular momentum, and stable shock loci are shown from top to bottom. The solid lines and open circles represent the analytical solutions and the numerical results, respectively. The analytical shock location shows $22.42r_g$, while the numerical results present $18.75r_g$. The injection radius $r_{inj} = 200r_g$, and at r_{inj} the radial velocity $v_{bulk}(inj) = 6.2248 \times 10^{-2}c$, sound speed $c_s(inj) = 1.4934 \times 10^{-2}c$, specific angular momentum $l_{inj} = 1.7cr_g$ and viscosity parameter $\alpha = 0.002$ (Lee et al. to be submit) .

4

Flow solutions with variable Γ around black holes

Accretion flow at very large distance from the BH is cold, therefore thermally non-relativistic, while close to the horizon, the flow is hot and may become thermally relativistic. In other words, if $\tilde{\Theta} = kT/mc^2$ be the non-dimensional temperature, where, k is Boltzmann constant, m is particle rest mass, then the non-relativistic temperature means $\tilde{\Theta} < 1$ and ultra relativistic temperature means $\tilde{\Theta} >> 1$. Therefore, Γ should vary with temperature from non-relativistic to highly relativistic limit *i.e.,* $5/3 \longrightarrow 4/3$. So, for a more correct study of flow variables and its derived quantities around a compact object, we should consider a relativistic EoS, where the adiabatic index is temperature dependent instead of being fixed value. Therefore, in this chapter, we have studied accretion-ejection flow with variable adiabatic index, multispecies fluid with pseudo-Newtonian potential, as well as, in the full relativistic regime. In the next section, we present solutions of multispecies flow around non-rotating BH, described by PW-potential. The flow is assumed adiabatic. In section (4.2), we have studied dissipative accretion-ejection flow around black holes, described by PW-potential. And in 4.3 section, accretion-ejection solutions are studied in full general relativistic regime.

4.1 Adiabatic flow with PW-potential

Here, we have studied the effect of the flow composition on outflow rates from adiabatic accretion discs around non-rotating BH. Although adiabatic accretion multispecies flow

was first investigated by Chattopadhyay & Chakrabarti (2011), but accretion-ejection solution was first investigated by us in Kumar et al. (2013). We have also investigated the various type of possible shock transitions in the accretion flow and represented them in the $\mathcal{E} - \dot{\mathcal{M}}$ plane. The fluid equations of motion for accretion are described below.

Differential equations: Since in this section we want to study adiabatic flow so we have ignored any dissipative processes in equations of motion. So, we have simplified fluid equations (2.14 - 2.18) with the help of relativistic EoS (2.70) and considering viscosity and radiative cooling terms to be zero. So λ is constant which makes equation (2.15) redundant, and the entropy equation (2.18) takes the form of the generalized adiabatic equation of state (2.74) and we obtain spatial derivatives of v and Θ as,

$$\frac{dv}{dx} = \frac{\mathcal{N}}{\mathcal{D}} = \frac{\frac{a^2}{\Gamma+1}\frac{5x-3}{x(x-1)} + \frac{\lambda^2}{x^3} - \frac{1}{2(x-1)^2}}{v - \frac{a^2}{v}[\frac{2}{\Gamma+1}]}, \tag{4.1}$$

and,

$$\frac{d\Theta}{dx} = -\frac{2\Theta}{2N+1}\left[\frac{1}{v}\frac{dv}{dx} + \frac{5x-3}{2x(x-1)}\right], \tag{4.2}$$

where, a is the adiabatic sound speed and is defined as $a^2 = 2\Gamma\Theta/\tilde{t}$. To find an accretion solution, we have to integrate equations (4.1) and (4.2) with the help of sonic point conditions (Chakrabarti 1989).

Sonic point conditions: The location of sonic point can be found by sonic point conditions, where $dv/dx = \mathcal{N}/\mathcal{D} \longrightarrow 0/0$ and gives two equations, one as $\mathcal{N} = 0$ and other by $\mathcal{D} = 0$, which are

$$M_{\rm c}^2 = \frac{\vartheta_{\rm c}^2}{a_{\rm c}^2} = \frac{2}{\Gamma_{\rm c}+1} \tag{4.3}$$

and

$$a_c^2 = \left(\frac{2}{M_c^2}\right)\left(\frac{5x_c-3}{x_c(x_c-1)}\right)\left(\frac{1}{2(x_c-1)^2} - \frac{\lambda_c^2}{x_c^3}\right), \tag{4.4}$$

where $M_{\rm c}, \vartheta_{\rm c}, a_{\rm c}, \Gamma_{\rm c}, N_{\rm c},$ and $\lambda_{\rm c}$ are the Mach number, the bulk velocity, the sound speed, the adiabatic index, the polytropic index and the specific angular momentum at the critical point $x_{\rm c}$, respectively. The bulk velocity gradient at the critical point is calculated by l′Hospital rule and is given by

$$\left(\frac{d\vartheta}{dx}\right)_{\rm c} = \left(\frac{d\mathcal{N}/dx}{d\mathcal{D}/dx}\right)_{x=x_{\rm c}}. \tag{4.5}$$

Equations (4.3—4.5) give the analytical critical point conditions, which are used to obtain the critical point of the flow. After doing some algebra equation (4.5) can be written in quadratic form,

$$\mathcal{A}\left(\frac{d\vartheta}{dx}\right)^2_{x_c} + \mathcal{B}\left(\frac{d\vartheta}{dx}\right)_{x_c} + \mathcal{C} = 0, \tag{4.6}$$

where, $\mathcal{A} = 2\left[1 + \frac{C_p}{\Gamma_c(2N_c+1)}\right]$, $\mathcal{B} = \frac{2\vartheta_c C_p(5x_c-3)}{\Gamma_c(2N_c+1)x_c(x_c-1)}$,

$$\mathcal{C} = \frac{\vartheta_c^2 C_p(5x_c-3)^2}{2\Gamma_c(2N_c+1)x_c^2(x_c-1)^2} + \frac{\vartheta_c^2(5x_c^2-6x_c+3)}{(2x_c^2(x_c-1)^2)} + \frac{3\lambda_c^2}{x_c^4} - \frac{1}{(x_c-1)^3}$$

and

$$C_p = \Gamma_c + \frac{\Theta_c}{\Gamma_c+1}\left(d\Gamma/d\Theta\right)_c.$$

Since equation (4.6) has two roots, they may be either real or complex conjugates depending on the discriminant $D_r = \mathcal{B}^2 - 4\mathcal{A}\mathcal{C}$ of this equation. This also gives the nature of the critical points. If $D_r < 0$ then the critical point will be spiral or O-type and if $D_r > 0$ then it will either be saddle type (*i.e.,*X-type if $\mathcal{C}/\mathcal{A} < 0$), or nodal type (if $\mathcal{C}/\mathcal{A} > 0$). Depending on the relative strengths of thermal energy and rotational energy of the flow, the accreting flow may have one to three sonic points. Out of the possible three sonic points, only two are physical (in the sense that, the flow actually passes through them) X-type and one is unphysical O-type which forms in between the two X-type sonic points. The sonic point which forms closer to the horizon is called the inner sonic point (x_{ci}), and the one far away is called outer sonic point (x_{co}). For flows with very low angular momentum or λ, generally only x_{co} forms, and flows with very high λ only x_{ci} forms, but for intermediate λ, multiple sonic may form (Liang & Thompson 1980; Fukue 1987; Chakrabarti 1989; Chattopadhyay & Chakrabarti 2011; Kumar & Chattopadhyay 2013). Since, accretion solutions may pass through two critical points, which are inner sonic point (x_{ci}) and outer sonic point (x_{co}). These two critical points are connected through shock transition.

Shock conditions: Since in this section, we have ignored any dissipative processes, so energy parameter ($\mathcal{E}$) is conserved across the shock transition and also the constant of motion. We presented Rankine Hugonit shock conditions

(2.28 - 2.31) in presence of massloss that gives the supersonic branch radial velocity and temperature from the post-shock quantities but the specific angular momentum is same across the shock and vice versa,

$$\vartheta_-^2 - 2(c_1 - h_-) = 0 \qquad \text{and} \qquad \Theta_- = \frac{\tilde{t}}{2}(c_0\vartheta_- - \vartheta_-^2), \tag{4.7}$$

here, $c_0 = (1 - R_{\dot{m}})[2\Theta_+/\tilde{t} + \vartheta_+^2]/\vartheta_+$ and $c_1 = \vartheta_+^2/2 + h_+$. Both the expressions (ϑ_-, Θ_-) in eq. 4.7 are obtained simultaneously in terms of post-shock quantities which gives us the shock location x_s.
In case of dissipative shocks, we use equations (2.27, 2.28, 2.32) to relate post-shock and pre-shock quantities. The relation is,

$$\vartheta_- = \sqrt{2(c_d - h_-(1 + f_e))}, \text{ and, } \Theta_- = \frac{\tilde{t}}{2}(c_0\vartheta_- - \vartheta_-^2), \tag{4.8}$$

where, $c_d = \vartheta_+^2/2 + h_+(1 + f_e)$. For isentropic shocks, we use eqs. (2.27, 2.28, 2.33) to obtain,

$$\vartheta_-\exp(k_{3-})\Theta_-^2(3\Theta_- + 2)^{k_1}(3\Theta_- + 2/\eta)^{k_2} - c_{e0} = 0; \text{ and, } \Theta_- = \frac{\tilde{t}}{2}(c_0\vartheta_- - \vartheta_-^2), \tag{4.9}$$

where, $c_{e0} = \vartheta_+\exp(k_{3+})\Theta_+^2(3\Theta_+ + 2)^{k_1}(3\Theta_+ + 2/\eta)^{k_2}$. The mass outflow rate $R_{\dot{m}}$ has calculated same as in previous chapter 3 and we are using same jet geometry but considering $R_f = 0$.

4.1.1 Solution procedure and Study of multispecies adiabatic flow

For adiabatic flow, solutions are characterized by specific energy or Bernoulli parameter $\mathcal{E}$, which is a constant of motion, specific angular momentum λ, which is also a constant of motion and in absence of particle production/annihilation the composition parameter ξ is also constant. We can find critical point directly from sonic point conditions (4.3 - 4.5) by using parameters ($\mathcal{E}, \lambda$ and ξ) but also can find from general solution procedure (3.2) as explained in previous chapter 3 and by putting ($\alpha = 0$) in their equations. If there is only one sonic point, one integrates equations (4.1, 4.2) inwards and outwards starting from the sonic point and using the sonic point conditions (4.3 - 4.5). In the multiple critical (or sonic) point regime or MCP regime, we may start with either x_{ci} or x_{co} and solve equations (4.1 - 4.5) to obtain the solutions. In case the flow parameters $\mathcal{E}$, λ, ξ fall in the MCP domain, we also check for the shock conditions (2.27 - 2.30) as

we integrate the equations of motion. In the first iteration we assume $R_{\dot{m}} = 0$. If the shock conditions are satisfied, the solution will jump to the supersonic branch through x_{co}. Once the shock is found, we solve jet equations (3.9 - 3.10) to find the jet solutions and the corresponding $R_{\dot{m}}$ (equation 3.23). This value of $R_{\dot{m}}$ is supplied to equation (4.7) and the whole solution procedure is repeated to obtain another shock location. This is repeated till the shock location converges. We will briefly show the three shock transitions in the $\mathcal{E} - \dot{\mathcal{M}}$ parameter space, and the related solutions (see Fig. 4.4). However, in the rest of the solutions, we will concentrate on adiabatic shocks and the resulting mass outflow rate.

4.1.1.1 Nature of critical points and accretion flow solutions

We discuss the properties of the critical points (CP) of the flow around black holes with relativistic equation of state (2.70) and how they are affected by parameters, ξ and λ. We plot $\mathcal{E}_c$ (Fig. 4.1 a), $\dot{\mathcal{M}}_c$ (Fig. 4.1b), Γ_c (Fig. 4.1c) and $log(T_c)$ (Fig. 4.1d) with $log(x_c)$ for $\xi = 1$ or electron-proton flow (hereafter $e^- - p^+$), and for $\lambda = 1.75$ (solid), 1.65 (dotted), 1.55 (dashed), 1.45 (long-dashed), and 1.35825 (dashed-dotted). For low λ (< 1.35825) there is only one sonic point for any value of $\mathcal{E}$, however, the number of sonic points increase with increasing λ. Moreover, Γ_c depend on the location of the sonic point. Lower temperature at the sonic point or T_c implies lower $\mathcal{E}_c$, $\dot{\mathcal{M}}_c$ and higher Γ_c. Since $\Gamma \to 5/3$ means non-relativistic thermal energy and $\Gamma \to 4/3$ implies ultra-relativistic thermal energy, so higher temperature implies lower Γ. The extrema of $\mathcal{E}_c(x_c)$ and $\dot{\mathcal{M}}_c(x_c)$ are joined by the long dashed-dotted curve in the figures which shows the domain of the parameters which supports multiple critical points (MCP).

In order to study the effect of ξ on sonic point properties, we plot $\mathcal{E}_c$ (Fig. 4.2a), $\dot{\mathcal{M}}_c$ (Fig. 4.2b), Γ_c (Fig. 4.2c) and $log(T_c)$ (Fig. 4.2d) with $log(x_c)$, for $\lambda = 1.65$, and $\xi = 1.0$ (solid), 0.75 (dotted), 0.5 (dashed), 0.25 (long-dashed), 0.1 (dashed-dotted) and 0.0 (long dashed-dotted). For flows with $1.0 \geq \xi > 0.0$ a maxima and a minima in $\mathcal{E}_c$ and $\dot{\mathcal{M}}_c$ exist, however for $\xi = 0.0$ there is only a minima and no maxima. Closer inspection reveals that for $\xi = 0$ or pair plasma flow or $e^- - e^+$ flow, the physical X type sonic points are formed closer to the horizon, which means, no matter what the value of λ, only one sonic point will form for $e^- - e^+$ flow, or for any flow described by single species EoS. So, we can say that multiple sonic points can be harboured by

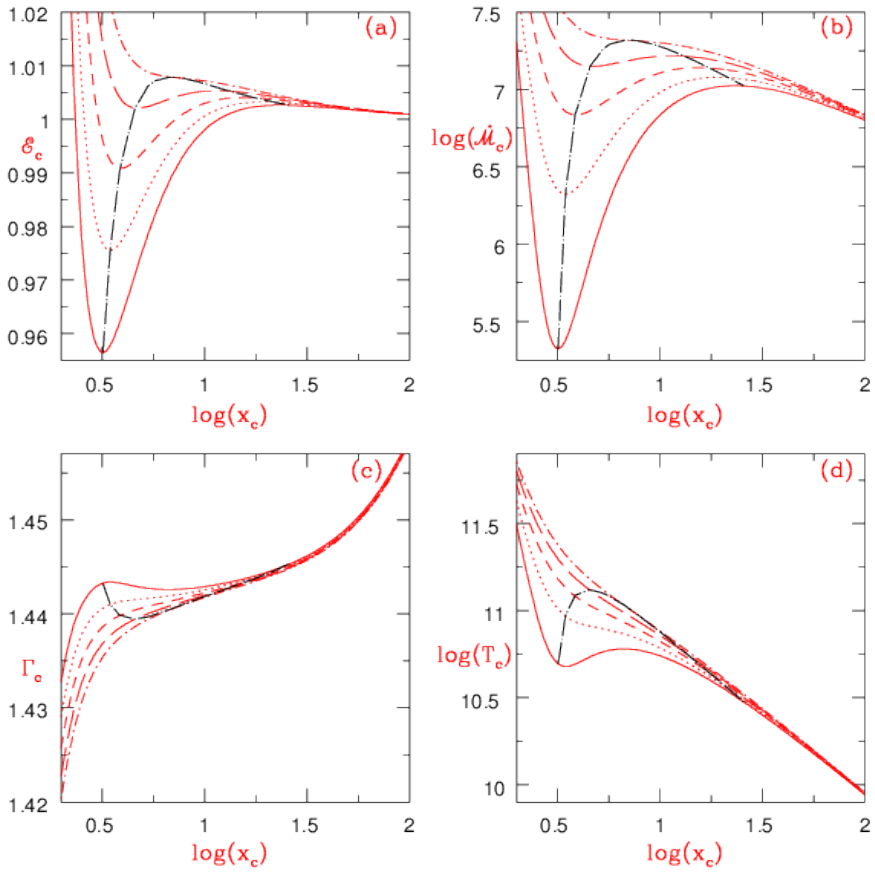

Figure 4.1: Effect of λ on CP - (a) $\mathcal{E}_c$, the specific energy at x_c, (b) entropy accretion rate ($\dot{\mathcal{M}}_c$) at x_c, (c) Γ_c and (d) $log(T_c)$ is plotted with $log(x_c)$ for $\xi = 1$ and for $\lambda = 1.75$ (solid), 1.65 (dotted), 1.55 (dashed), 1.45 (long-dashed), and 1.35825 (dashed-dotted). Long dashed-dotted curve is the loci of maxima and minima of the curves and represents the part of the parameter space which gives multiple critical points(MCP). Kumar et al. (2013).

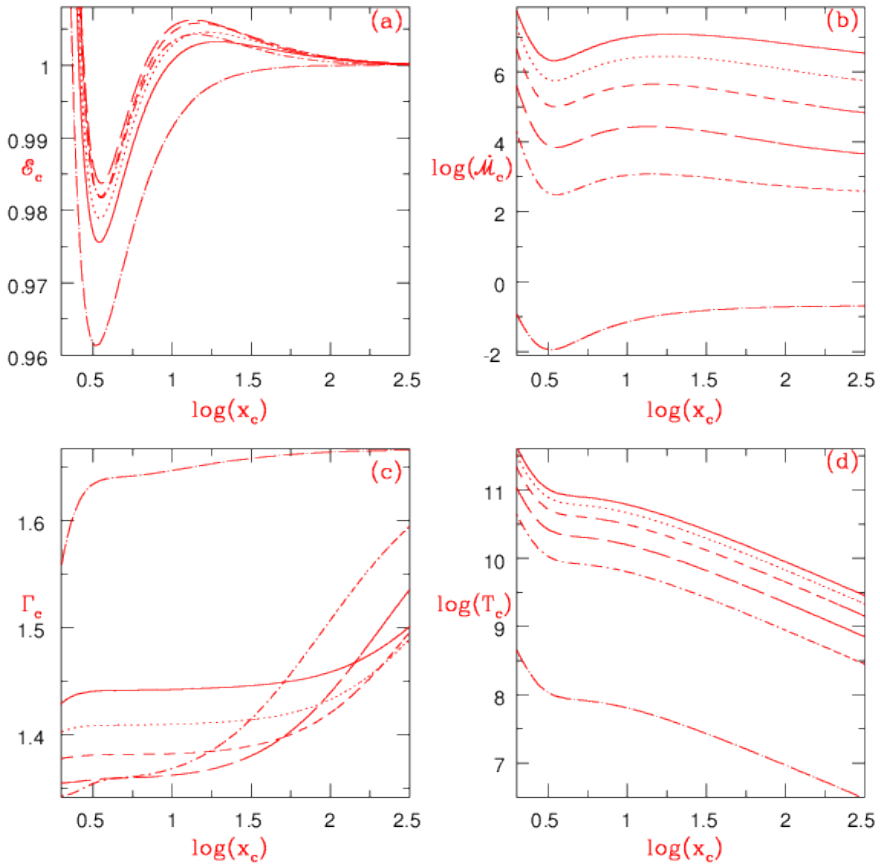

Figure 4.2: Effect of ξ on CP - (a) $\mathcal{E}_c$, the specific energy at x_c, (b) entropy accretion rate ($\dot{\mathcal{M}}_c$) at x_c, (c) Γ_c and (d) $log(T_c)$ is plotted with $log(x_c)$ for $\lambda = 1.65$ and for $\xi = 1.0$ (solid), 0.75 (dotted), 0.5 (dashed), 0.25 (long-dashed), 0.1 (dashed-dotted) and 0.0 (long dashed-dotted). Kumar et al. (2013).

hot flows, and as Fig. 4.2d shows that T_c is lowest for $e^- - e^+$ flow (long dashed-dotted). A flow is thermally relativistic if its thermal energy is comparable to its rest energy *i.e.*,$\Theta = kT/m_e c^2 \gtrsim 1$, and the adiabatic index will be reflected by a value $4/3 \leq \Gamma < 5/3$. Although, $e^- - e^+$ is the lightest flow, its T_c is so low that for most values of x_c, $\Gamma_c \sim 5/3$ (long dashed-dotted in Fig. 4.2c). Therefore, at a large distance away from the black hole, physical sonic points are not formed. Closer to the horizon, the flow is hot enough to produce one physical sonic point. As ξ increases, the rest energy increases but the temperature increases even more, which makes flow with protons much hotter and thermally more relativistic (Fig. 4.2c). Therefore, for a given $\mathcal{E} > 1$, one or more sonic points may form.

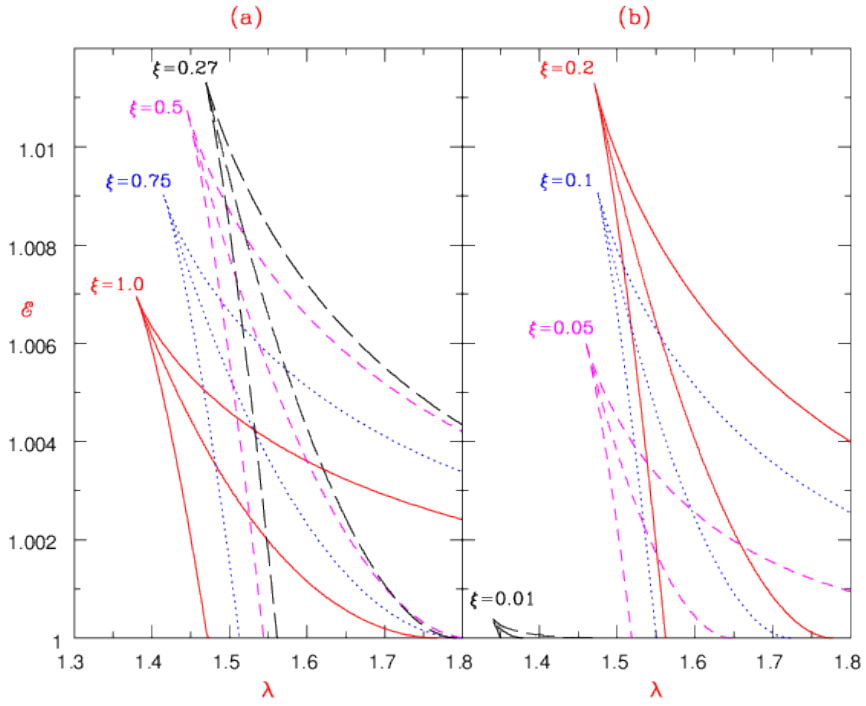

Figure 4.3: MCP space - $\mathcal{E} - \lambda$ parameter space represents multiple critical points (MCP) domain for (a) $\xi = 1.0$ (solid), $\xi = 0.75$ (dotted), $\xi = 0.5$ (dashed) and $\xi = 0.27$ (long-dashed) and (b) $\xi = 0.2$(solid), $\xi = 0.1$ (dotted), $\xi = 0.05$ (dashed) and $\xi = 0.01$ (long-dashed). Kumar et al. (2013).

One may join the maxima and minima of the $\mathcal{E}_c(x_c)$ and the corresponding λ-s for a given ξ as shown in Fig. 4.1, and plot in $\mathcal{E} - \lambda$ plane, the resulting bounded region gives the values of $\mathcal{E}$, λ which supports multiple sonic points, and are abbreviated as MCP region (multiple critical point). In Fig. 4.3a, we plot the MCP for $\xi = 1.0$ or $e^- - p^+$ (solid), $\xi = 0.75$ (dotted), $\xi = 0.5$(dashed) and $\xi = 0.27$(long-dashed), while in Fig. 4.3b, we plot $\xi = 0.2$ (solid), $\xi = 0.1$ (dotted), $\xi = 0.05$ (dashed) and $\xi = 0.01$ (long-dashed). It shows that as ξ is reduced, the reduction of rest energy is making the flow more energetic and relativistic, so the MCP shifts to higher energy, higher angular momentum side. This continues till $\xi = 0.27$. Any further reduction of ξ, reduces the temperature to the extent that simultaneous reduction in rest energy cannot compensate for the lack of thermal energy, and the flow becomes less energetic and less relativistic, compared to flow of $\xi = 0.27$. The MCP shifts to the less energetic and lower angular momentum part of the parameter space, with simultaneous reduction in the area of the MCP, which finally vanishes for $\xi = 0.0$.

The sonic point properties not only tells us about the number of sonic points, but also about the nature of transitions in the solution. In Fig. 4.4, we plot $\mathcal{E}_c$ with $\dot{\mathcal{M}}_c$ for $\lambda = 1.6$ and $\xi = 1.0$. The inner sonic point quantities are plotted along MN, while middle and outer sonic point quantities are NO and OQ, respectively. Adiabatic shocks occur parallel to the $\dot{\mathcal{M}}_c$ axis, *i.e.,* along $S_4 \rightarrow S_1$, the T_1 inset shows the actual Mach number ($M = v/a$) solution of such a transition. The dissipative shock shown by $S_4 \rightarrow S_2$ or T_2 transition. An isentropic shock is parallel to the ordinate represented by eq. 4.9, and by the transition $S_4 \rightarrow S_3$ or T_3 transition. The energy and entropy jumps for the respective transitions are marked in the Figure.

Various flow quantities of the accretion disc (*i.e.,*without allowing for mass loss) are plotted in Figs. 4.5a-l. The flow variables are M (Figs. 4.5a, e, i), T (Figs. 4.5b, f, j), Γ (Figs. 4.5c, g, k) and $\dot{\mathcal{M}}$ (Figs. 4.5e, h, l) as a function of the radial distance $[log(x)]$. From Figs. 4.3a-b, it can be shown that for a particular $\mathcal{E}$ & λ, if one ξ value produces multiple critical points, then another ξ can exhibit only one sonic point. However, for Figs. 4.5a-l, we have chosen a value of $\mathcal{E}$ & λ which admits shock solutions for a wide range of ξ ($= 1 \rightarrow 0.087$). In Figs. 4.5a-l, we consider the same $(\mathcal{E}, \lambda) = (1.0001, 1.68)$, but different compositions: $e^- - p^+$ or $\xi = 1.0$ (in Figs. 4.5a-d), $\xi = 0.5$ (in Figs. 4.5e-h), and $e^- - e^+$ or $\xi = 0.0$ (in Figs. 4.5i-l). The temperature and the entropy is higher for higher ξ, and the shock location is also at a larger distance for flow with

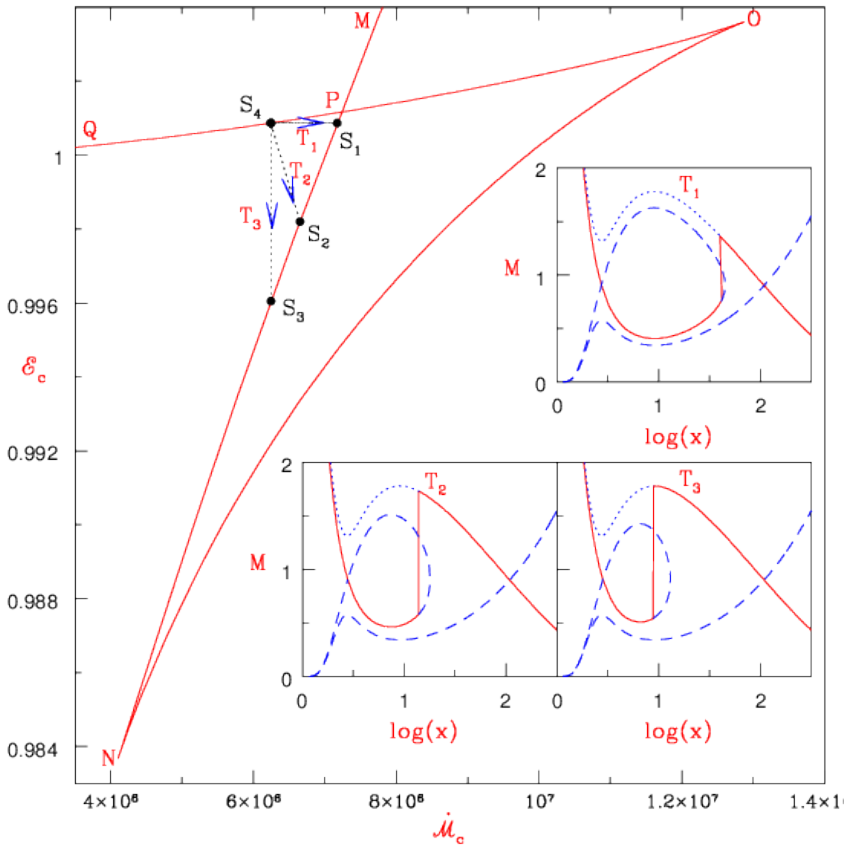

Figure 4.4: Multiple shock transitions - Plot of $\mathcal{E}_c$ with $\dot{\mathcal{M}}_c$ for $\lambda = 1.6$ and $\xi = 1.0$. Branches MN, NO and OQ corresponds to inner, middle and outer critical points of the flow, respectively. The adiabatic shock transition T_1 shown as $S_4 \rightarrow S_1$, the dissipative shock T_2, shown as $S_4 \rightarrow S_2$ and isentropic shock T_3, shown as $S_4 \rightarrow S_3$. The solutions corresponding to transitions T_1, T_2, T_3 are shown in the inset, where solid curves represent accretion flows with shocks. The coordinates of the transitions are $S_1(\mathcal{E} = 1.0087, \dot{\mathcal{M}} = 7.17 \times 10^6), S_2(\mathcal{E} = 0.9982, \dot{\mathcal{M}} = 6.65 \times 10^6)$, $S_3(\mathcal{E} = 0.99605, \dot{\mathcal{M}} = 6.25 \times 10^6)$, and $S_4(\mathcal{E} = 1.0087, \dot{\mathcal{M}} = 6.25 \times 10^6)$. Kumar et al. (2013).

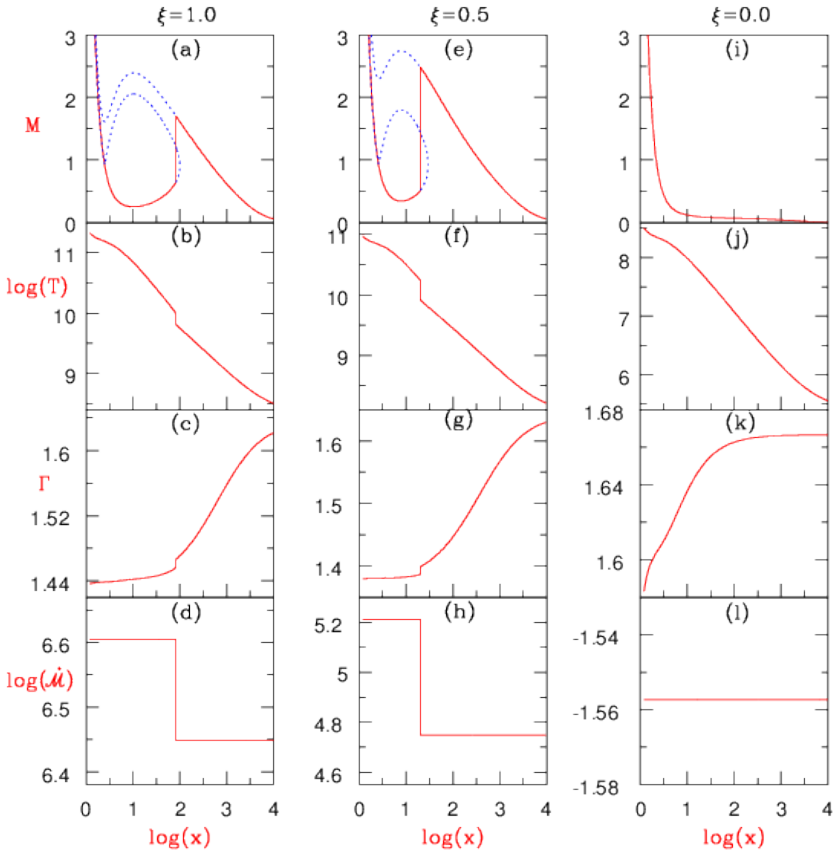

Figure 4.5: Accretion flow quantities - Various accretion flow quantities are plotted with radial distance $[log(x)]$: (a, e, i) Mach number (M), (b, f, j) temperature (T), (c, g, k) adiabatic index (Γ) and (e, h, l) entropy accretion rate $(\dot{\mathcal{M}})$ for the accretion disc parameters, $(\mathcal{E}, \lambda) = (1.0001, 1.68)$ with $\xi = 1.0$ (a-d), 0.5 (e-h) and 0.0 (i-l). Kumar et al. (2013)

higher ξ. Figures 4.5c, g & k, show that Γ is variable for flows with any ξ. At $x \rightarrow$ large, $\Gamma \sim 5/3$, irrespective of the value of ξ. However, since $\xi = 0.0$ flow has very low thermal energy, $\Gamma \sim 5/3$ up to $x \sim 100$. But for flows with $\xi \neq 0.0$, we find $\Gamma_{\xi=0.5} < \Gamma_{\xi=1.0}$ at $x <$few$\times 100$. At $x \sim 1$, $\Gamma_{\xi=0.5} \sim 1.4$, $\Gamma_{\xi=1.0} \sim 1.44$. This means that the flow becomes thermally more relativistic with the reduction of ξ up to a certain value (*i.e.,*around $\xi \sim 0.27$), and then becomes less relativistic with further reduction of ξ. Although $\xi = 0.5$ and $e^- - p^+$ flow for the chosen value of $\mathcal{E}$ & λ harbours shocks, but shock location and other flow parameters are quite different. $e^- - e^+$ being the coldest, slowest and showing only a single sonic point, is significantly different from any flow with $\xi \neq 0.0$.

4.1.1.2 Accretion and ejection solutions

In this subsection, we present self-consistent accretion-ejection solutions. The methodology to obtain simultaneously and self- consistently computation of the accretion-ejection solution has been presented in Section 3.2. In Figs. 4.6a-c, the accretion disc flow quantities like M (a), Γ (b), and $\dot{\mathcal{M}}$ (c) are plotted as a function of radial distance. In Figs. 4.6d-f, the jet flow quantities *e.g.,*M_j (d), Γ_j (e), and $\dot{\mathcal{M}}_j$ (f) are plotted as a function of r_j. The constituent of the flow of the disc-jet system presented in this Figure is $\xi = 1.0$. Other flow parameters are: $\mathcal{E} = 1.001$, $\lambda = 1.56$. The accretion disc solution admits an accretion shock at $x_s = 15.306$ (vertical jump in Figs. 4.6a-c), and launches a thermally driven bipolar jet whose sonic point is at $r_{jc} = 209.139$. The relative mass outflow rate is $R_{\dot{m}} = 0.038$. The jet starts with the Γ value of the post-shock disc but since it is thermally driven and is powered by converting the thermal energy to kinetic energy, Γ approaches non-relativistic values far away from the central object. At the shock, the entropy of the jet jumps up from pre-shock to post-shock value (Fig. 4.6c). Interestingly, the entropy of the jet is also much higher than the pre-shock disc. This entropy condition ensures that although most of the matter flows through the inner sonic point into the black hole, a significant amount of matter also flows out as jet.

Now, we plot x_s with λ (Fig. 4.7a), $R_{\dot{m}}$ with x_s (Fig. 4.7b), compression ratio $R = \Sigma_+/\Sigma_-$ with x_s (Fig. 4.7c), and $R_{\dot{m}}$ with R (Fig. 4.7d), the composition of the flow is given by $\xi = 0.27$. Parameters for each curve is $\mathcal{E} = 1.0002$ (solid), 1.0004 (dotted), and 1.0006 (dashed). For a given value of λ, x_s increases with $\mathcal{E}$. Similarly for a given x_s, $R_{\dot{m}}$ increases with $\mathcal{E}$, but R decreases with the increasing $\mathcal{E}$. This obviously

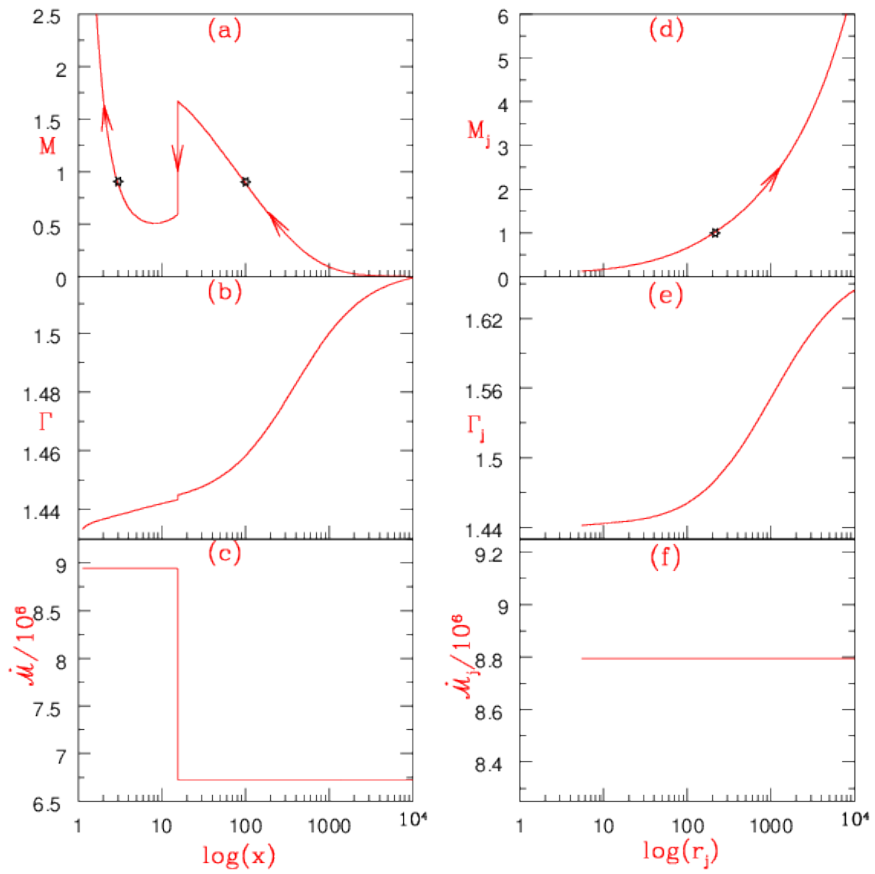

Figure 4.6: Accretion-ejection solutions - Accretion-jet solution for $e^- - p^+$ flow, for $\mathcal{E} = 1.001$, $\lambda = 1.56$. The accretion shock denoted by the vertical jump is at $x_s = 15.306$. The accretion flow variables M (a), Γ (b) and the entropy-accretion rate $\dot{\mathcal{M}}$ (c) are plotted with x. The jet variables $M_j = \vartheta_j/a_j$ (d), Γ_j (e), and $\dot{\mathcal{M}}_j$ (f) plotted with jet radial coordinate r_j. Arrows show the direction of the flow and the stars denote the critical or sonic points of the flow. Kumar et al. (2013).

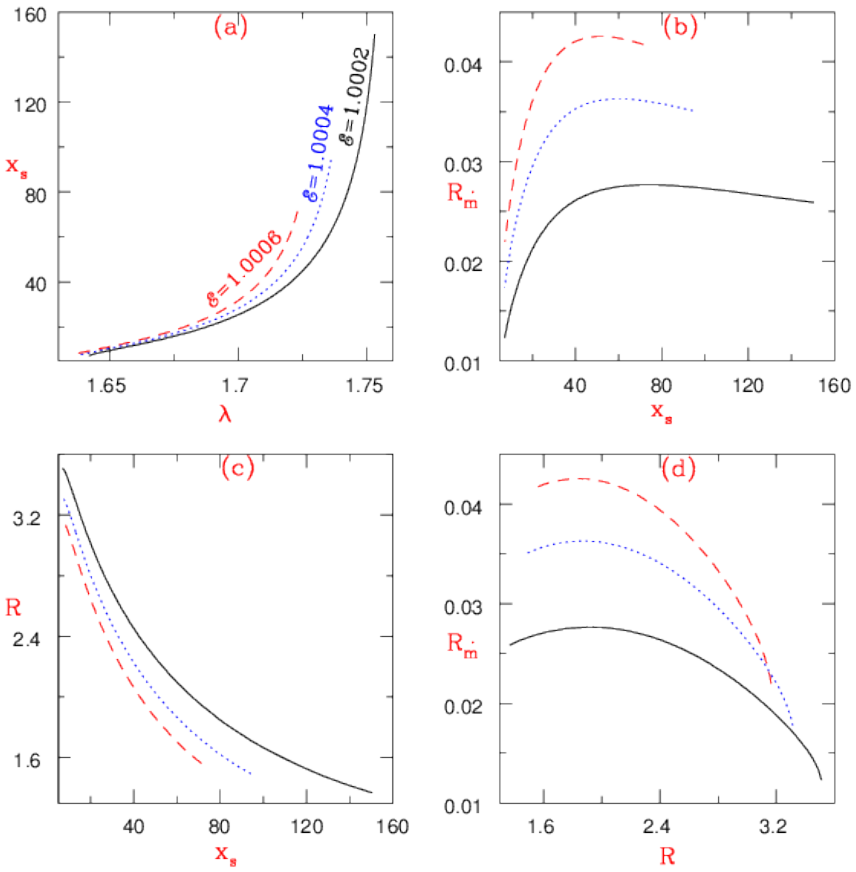

Figure 4.7: Nature of $R_{\dot{m}}$ with $\mathcal{E}, \lambda$ - Plot of (a) x_s with λ, (b) $R_{\dot{m}}$ with x_s, (c) Compression ratio R with x_s and (d) $R_{\dot{m}}$ with R. Each curve corresponds to $\mathcal{E} = 1.0002$ (solid), 1.0004 (dotted), and 1.0006 (dashed). Kumar et al. (2013).

means $R_{\dot{m}}$ increases with $\mathcal{E}$. Interestingly, the dependence of $R_{\dot{m}}$ with R for a given $\mathcal{E}$, qualitatively follows the pattern of Chakrabarti (1999). For a given $\mathcal{E}$, x_s decreases with decreasing λ. This increases the compression, and drives more matter into the jet channel. But with decreasing x_s, the post-shock area decreases too, and that also limits the total amount of matter leaving the disc. Hence $R_{\dot{m}}$ will depend on increasing R, as well as the decreasing total post-shock area, and hence $R_{\dot{m}}$ peaks at some intermediate value of R.

Keeping $\mathcal{E} = 1.0003$, we now vary λ, of flow with following compositions $\xi = 1.0$ (solid), $\xi = 0.635$ (dotted), and $\xi = 0.27$ (dashed). We plot x_s with λ (Fig. 4.8a), $R_{\dot{m}}$ with x_s (Fig. 4.8b), R with x_s (Fig.4.8c), and $R_{\dot{m}}$ with R (Fig. 4.8d). We reconfirm that indeed $R_{\dot{m}}$ increases with the increasing R or decreasing x_s, although decreasing post-shock surface area finally decreases $R_{\dot{m}}$. $R_{\dot{m}}$ is highest for $\xi = 0.27$, compared to flow of other compositions. To ensure this we scan the entire $\mathcal{E}$ & λ parameter space for a given value of ξ, and find out the maximum mass outflow rate possible for that particular ξ. In Fig. 4.9, we plot the maximum mass-outflow rate *i.e.*,$R^m_{\dot{m}} = max(R_{\dot{m}})$, as a function of ξ. It easily shows that maximum outflow is possible for $\xi = 0.27$.

In Figs. 4.10a-b, we show the parameter space where standing shocks form (the so-called 'shock-domain') for various ξ. Similar to the behaviour of MCP domain, the shock domain in $\mathcal{E} - \lambda$ parameter space shifts to the higher energy and angular momentum region as ξ is decreased from its $e^- - p^+$ value up to $\xi = 0.27$. If ξ is decreased further, the flow becomes less energetic and the shock-domain moves towards the lower energy and lower angular momentum corner, with subsequent decrease in the bounded area of the shock space. Finally, the shock domain disappears for $\xi = 0.0$. In Fig. 4.10c, we compare the shock domain for $\xi = 1.0$, of the accretion flow which includes mass loss (solid) and which does not include mass loss (dotted). In Fig. 4.10d, we compare the shock domain for $\xi = 0.25$, of the accretion flow which includes mass loss (solid) and which does not mass loss (dotted). This shows that the reduction of post-shock pressure due to mass loss, reduces the steady shock domain. Flow from that part of the parameter space which admits shock without massloss, actually do not show steady shock when massloss is allowed. So there is a possibility of massloss driven shock oscillation too.

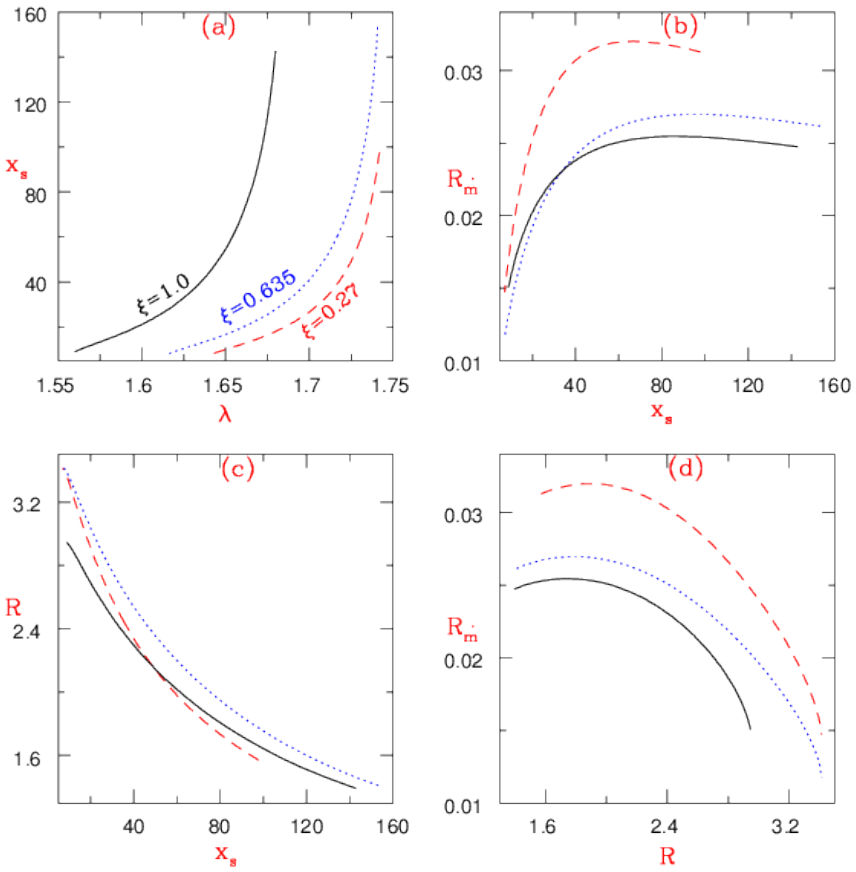

Figure 4.8: Nature of $R_{\dot{m}}$ with ξ, λ - (a) Plot of x_s with λ, (b) $R_{\dot{m}}$ with x_s, (c) R with x_s, and (d) $R_{\dot{m}}$ with R for $\mathcal{E} = 1.0003$. Each curve corresponds to $\xi = 1.0$ (solid), 0.635 (dotted), and 0.27 (dashed). Kumar et al. (2013).

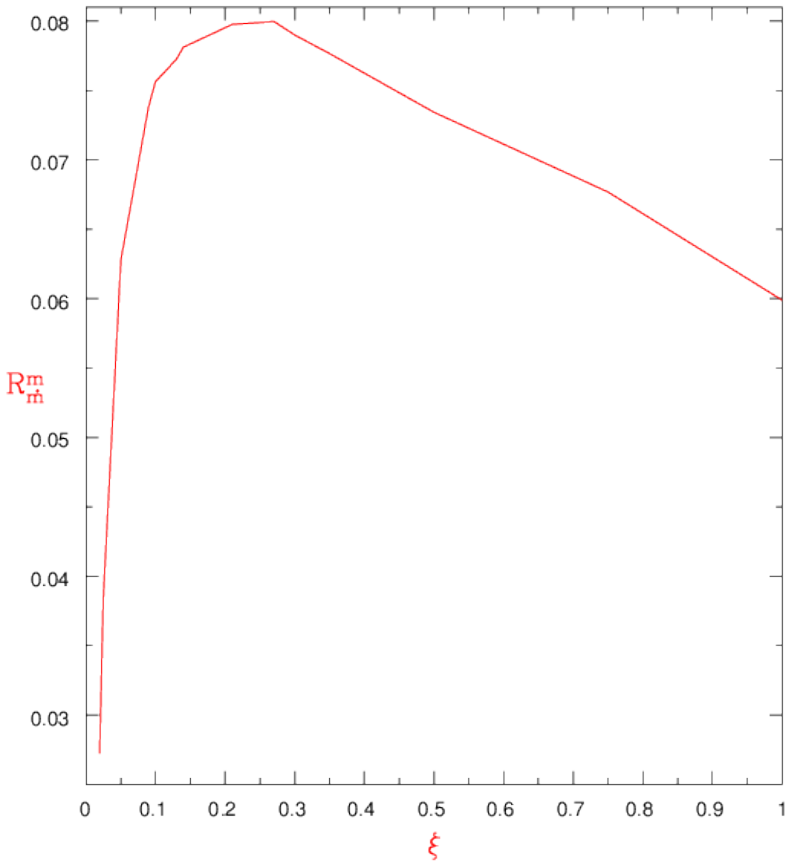

Figure 4.9: $R^m_{\dot{m}}$ **with** ξ - The plot of maximum mass outflow rate $R^m_{\dot{m}}$ with the composition parameter ξ. Kumar et al. (2013).

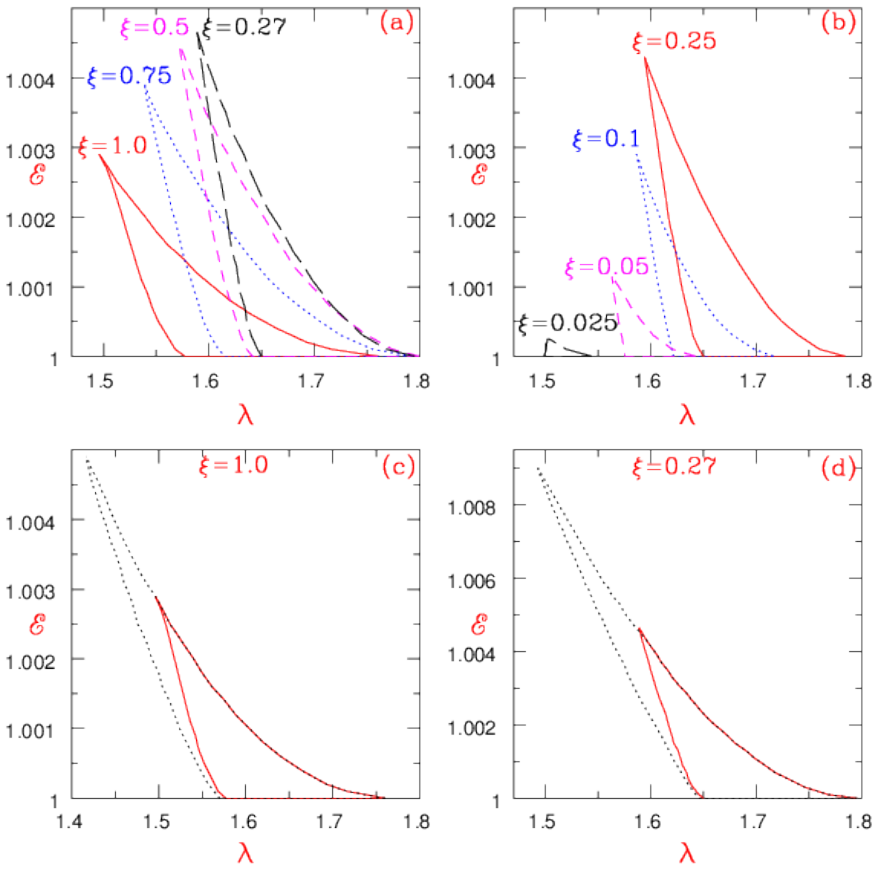

Figure 4.10: Shock -domains with ξ - Shock-domain in the $\mathcal{E}-\lambda$ parameter space with mass loss. Flow composition ξ is marked. (a) Parameter space for $\xi = 1.0 \rightarrow 0.27$ and (b) for $\xi = 0.25 \rightarrow 0.025$. (c) Comparison of the domains in $\mathcal{E} - \lambda$ space with mass loss (solid) and without mass loss (dotted) for $\xi = 1.0$ and (d) Comparison of the 'shock-domain' with mass loss (solid) and without mass loss (dotted) for $\xi = 0.27$. Kumar et al. (2013).

4.2 General fluid flow with PW-potential

Here, we are considering dissipative flow, which has viscosity and radiative cooling around the BHs. We obtained the generalized Bernoulli parameter (ε), which is constant of motion in presence of viscosity and radiative cooling. We have studied the all possible transonic accretion solutions for variety of boundary conditions, viscosity parameters and accretion rates. We have also calculated the accretion disc luminosities for given flow parameters. For the study of dissipative flow used fluid equations of motion in form of differential equations are presented below.

Differential equations: We have simplified fluid equations (2.14 - 2.18) with the help of relativistic EoS (2.70) and considering both viscous and radiative cooling process, we obtained spatial derivatives of v, Θ and λ:

$$\frac{dv}{dx} = \frac{a^2[\frac{2}{\Gamma+1}\frac{5x-3}{2x(x-1)}] + \frac{\nu x^2}{vN(\Gamma+1)}\left(\frac{d\Omega}{dx}\right)^2 - \frac{f(x_s)}{vN(\Gamma+1)}[Q_{\rm S}^- + Q_{\rm B}^-] + \frac{\lambda^2}{x^3} - \frac{1}{2(x-1)^2}}{v - \frac{a^2}{v}[\frac{2}{\Gamma+1}]}, \tag{4.10}$$

derivative of temperature,

$$\frac{d\Theta}{dx} = -\frac{2\Theta}{2N+1}\left[\frac{1}{v}\frac{dv}{dx} + \frac{5x-3}{2x(x-1)}\right] - \frac{\nu x^2 \tilde{t}}{(2N+1)v}\left(\frac{d\Omega}{dx}\right)^2 + \frac{\tilde{t} f(x_s)}{(2N+1)v}[Q_{\rm S}^- + Q_{\rm B}^-], \tag{4.11}$$

and derivative of specific angular momentum,

$$\frac{d\lambda}{dx} = 2x\Omega + x^2\frac{d\Omega}{dx}, \tag{4.12}$$

$$\text{where,} \quad \frac{d\Omega}{dx} = -\frac{\Gamma u \Omega_k(\lambda - \lambda_0)}{\alpha a^2 x^2} \tag{4.13}$$

here Γ varies with distance. The cooling term is defined as $Q^- = \Lambda^-/\Sigma = \chi f(x_s)(Q_{\rm S}^- + Q_{\rm B}^-)$, where χ is the cooling parameter, such that the radiative cooling will be turned off by putting $\chi = 0$, or will be turned on if $\chi = 1$. Here, $f(x_s)$ is a polynomial function (A.1) and called as Comptonization parameter (Kumar et al. 2014), which is assumed to be generic and has been presented in details in appendix (A). It is computed once the accretion shock is present in the flow, otherwise, for shock free solution, $f(x_s) = 1$. The cooling term also contains synchrotron emissivity, or, $\Lambda_{\rm S}^-$ (Shapiro & Teukolsky 1983), and bremsstrahlung emissivity, or, $\Lambda_{\rm B}^-$ (Rybicki & Lightman 1979; Svensson

1982)and are defined as

$$Q_{\rm S}^{-}=\Lambda_{\rm S}^{-}/\Sigma=\frac{S_0\Theta_{\rm e}^3}{v\sqrt{\Theta x^3}(x-1)}\ \text{ and }\ Q_{\rm B}^{-}=\Lambda_{\rm B}^{-}/\Sigma=\frac{B_0\sqrt{\Theta_{\rm e}}}{v\sqrt{\Theta x^3}(x-1)},\quad(4.14)$$

where,

$$S_0=\frac{16\times1.44\times10^{17}}{3}\frac{e^4\beta\dot{m}}{m_{\rm e}^3c^3K^{3/2}}\frac{1}{GM_\odot}$$

and

$$B_0=\frac{1.44\times10^{17}K_{\rm ep}\xi(2-\xi)\dot{m}}{16\pi m_{\rm e}^2K^{3/2}}\frac{1}{GM_\odot c^2},$$

where, $K_{\rm ep}=32m_{\rm e}c^3r_{\rm e}^2\alpha_{\rm f}\sqrt{(2/\pi)}/3=1.2135\times10^{-22}$, $\dot{m}=\dot{M}/\dot{M}_{\rm Edd}$ is the accretion rate in units of Eddington rate, the fine structure constant is given by $\alpha_{\rm f}=1/137.036$ and classical electron radius $r_{\rm e}=2.81794\times10^{-13}$cm. Here we have considered $\dot{M}_{\rm Edd}=1.44\times10^{17}M_B/M_\odot$. The magnetic field ($B$) is stochastic and is assumed to be in total or partial equipartition with the gas pressure. The ratio between magnetic and gas pressure is $\beta=B^2/(8\pi p)$, such that $0\leq\beta\leq1$. To find an accretion solution, we have to integrate equations (4.10)-(4.12). Since, accretion solutions are necessarily transonic in nature but for dissipative flow the location of sonic point (x_c) or number of sonic points are not known a priori.

Sonic point conditions: The sonic point conditions are mathematically represented as $dv/dx=\mathcal{N}/\mathcal{D}\longrightarrow0/0$ and gives two equations, one by $\mathcal{N}=0$ and other by $\mathcal{D}=0$. Which are

$$M_{\rm c}^2=\frac{\vartheta_{\rm c}^2}{a_{\rm c}^2}=\frac{2}{\Gamma_{\rm c}+1}\quad(4.15)$$

and

$$\frac{(5x_{\rm c}-3)M_{\rm c}^2}{2x_{\rm c}(x_{\rm c}-1)}a_{\rm c}^2+\frac{\Gamma_{\rm c}M_{\rm c}\Omega_{\rm K}(\lambda_c-\lambda_0)^2}{\alpha a_{\rm c}x_{\rm c}^2(2N_{\rm c}+1)}-\frac{\mathscr{F}(x_{\rm s})[Q_{\rm Sc}^{-}+Q_{\rm Bc}^{-}]}{\vartheta_{\rm c}(2N_{\rm c}+1)}+\frac{\lambda_{\rm c}^2}{x_{\rm c}^3}-\frac{1}{2(x_{\rm c}-1)^2}=0.\quad(4.16)$$

The bulk velocity gradient at the critical point is calculated by l'Hospital rule and is given by

$$\left(\frac{d\vartheta}{dx}\right)_{\rm c}=\left(\frac{d\mathcal{N}/dx}{d\mathcal{D}/dx}\right)_{x=x_{\rm c}}.\quad(4.17)$$

Equations (4.15—4.17) give the critical point conditions, which are used to obtain the location of critical point and value of the flow variables of the flow.

since, accretion solutions may pass through two critical points, which are inner sonic point (x_{ci}) and outer sonic point (x_{co}). These two critical points are connected through shock transition.

Shock conditions: The explicit form of the shock conditions (2.27 - 2.30) in a compact form for accretion solution are,

$$\vartheta_-^2 - 2\left(c_1 - h_- + \frac{\lambda_-^2}{2x_{\rm s}^2} - \frac{\lambda_-\lambda_0}{x_{\rm s}^2} + \zeta_-\right) = 0, \quad \Theta_- = \frac{\tilde{t}}{2}\left(c_0\vartheta_- - \vartheta_-^2\right)$$
$$\text{and} \qquad \lambda_- = \lambda_0 + \frac{c_2 a_-^2}{\Gamma_-\vartheta_-}, \tag{4.18}$$

where $c_0 = [2\Theta_+/\tilde{t} + \vartheta_+^2]/\vartheta_+$, $c_1 = \vartheta_+^2/2 + h_+ - \lambda_+^2/(2x_{\rm s}^2) + \lambda_+\lambda_0/x_{\rm s}^2 - \zeta_+$, $\zeta_+ = \zeta_{\rm S+} + \zeta_{\rm B+}$, $c_2 = \Gamma_+\vartheta_+(\lambda_+ - \lambda_0)/(a_+^2)$ and $\zeta_- = (f_{\Theta_{\rm e}}^3\zeta_{S+} + f_{\Theta_{\rm e}}^{1/2}\zeta_{\rm B+})/(f_\vartheta^2 f_\Theta^{1/2})$. Moreover, $f_{\Theta_{\rm e}} = \Theta_{\rm e-}/\Theta_{\rm e+}$, $f_\vartheta = \vartheta_-/\vartheta_+$ and $f_\Theta = \Theta_-/\Theta_+$. All three quantities ($\vartheta_-, \Theta_-$ and λ_-) in equation 4.18 are obtained simultaneously in terms of post-shock quantities which eventually gives us the shock location $x_{\rm s}$.

If $\alpha \neq 0, \chi \neq 0$ and conserving E equation (2.23) instead of ε, it gives dissipative shock in presence of viscosity and cooling. Putting, $\zeta_- = \zeta_+ = 0$ in equation (4.18), then we get dissipative shock and energy dissipation at shock front can be calculated as $\triangle\varepsilon = \varepsilon_- - \varepsilon_+$.

4.2.1 Solution procedure

We have solved equations (4.10)-(4.17), by using set of flow parameters, $\varepsilon, \lambda_0, \alpha, \xi$ and in presence of radiative cooling ($\dot{m}, \beta$). Since, the sonic point for dissipative flow is not known a priori, so as the first step to find complete solutions, one need to find a method to compute the location of the sonic point. For the calculation of critical point, we have used same mathematical techniques as before in chapter 3 but in solving asymptotic values of flow variables near the horizon, we use the conservation equations judiciously and do not need to make an explicit assumption of free fall close to the horizon. So, we have get values of exponents (τ and $\mathcal{B}$) of equation (3.13) are different from as calculated in section (3.2), which are

$$\tau = 2 \qquad \text{and} \qquad \mathcal{B} = 4\alpha\lambda r_{\rm g}^2 \frac{\sqrt{2\Theta}}{\Gamma\sqrt{K}\dot{\mathcal{M}}} \exp(k_3)\Theta^{3/2}(3\Theta+2)^{k_1}(3\Theta+2/\eta)^{k_2}a^2.$$

And remaining computational techniques are same as in previous chapter 3, to find sonic point. Once we find the sonic point then we can integrate equations (4.10, 4.11 and

4.12) to and fro from sonic point then we get complete solutions for given parameters. When integrating equations of motion outward from sonic point, also checking for shock conditions. we calculate the supersonic branch quantities ϑ_-, Θ_-, and λ_- at the tentative jump radius $\bar{x}_{\rm s}$. Using these variables and $\bar{x}_{\rm s}$ as the starting point, we solve the equations of motion to find out the outer sonic point of $x_{\rm co}$ by checking the sonic point conditions (4.15-4.17) iteratively. Once $x_{\rm co}$ is determined, then the corresponding $\bar{x}_{\rm s}$ is the tentative shock location. Now supplying $\bar{x}_s$ in equation (A.1), we find the Comptonization factor $\mathscr{F}(\bar{x}_{\rm s})$ and update Q^-. With this new cooling, we again recalculate the shock location by recalculating the sonic point and checking shock conditions (4.18). Once the shock location converges to a value $x_{\rm s}$, we have a self consistent shocked accretion solution.

Here, the accretion solutions are characterized by the following flow parameters: the generalized Bernoulli parameter ε, and $\dot{m}$ which are constants of motion. Furthermore, λ_0 or the angular momentum on the horizon is a constant of integration, and viscosity parameter α are the two more parameters. On the top of that, ξ the composition fraction determines the flow composition and therefore the EoS, and β controls the synchrotron emission, by estimating the magnetic energy. It is to be understood that the equations of motion (equations 2.27-2.30) are not over determined, because $\dot{m}$ and β together controls the cooling processes. It is to be remembered that supplying the inner boundary condition ($\varepsilon,\ \lambda_0,\ \dot{m}$) to determine the sonic points in presence of α, ξ and β is equivalent to, supplying the outer boundary condition ($\varepsilon,\ \lambda_{\rm inj},\ \dot{m}$), where $\lambda_{\rm inj}$ is the specific angular momentum at the outer boundary. The outer boundary of the disc is symbolized by $x_{\rm inj}$. Following equation (4.14), the total surface luminosity of the disc is given by

$$\mathscr{L}_{\rm t} = 4\pi \int \mathscr{F}(x_{\rm s})(Q^-_{\rm S} + Q^-_{\rm B})\Sigma x {\rm d}x, \quad \text{and } \ell = \mathscr{L}_{\rm t}/L_{\rm Edd}, \tag{4.19}$$

where $\mathscr{L}_t$ is the total luminosity and ℓ is the dimensionless luminosity in units of $L_{\rm Edd} \approx 1.3 \times 10^{38}(M_B/M_\odot)$. The relation between Eddington accretion rate and Eddington limit is $\dot{M}_{\rm Edd} = L_{\rm Edd}/c^2$.

4.2.2 All possible transonic accretion solutions for $e^- - p^+$ flow

In Fig. 4.11, we present the full $\varepsilon - \lambda_0$ parameter space, and all possible accretion solutions, corresponding to $\xi = 1.0$ or $e^- - p^+$ flow, $\alpha = 0.05,\ \beta = 0.01$ and $\dot{m} = 0.1$.

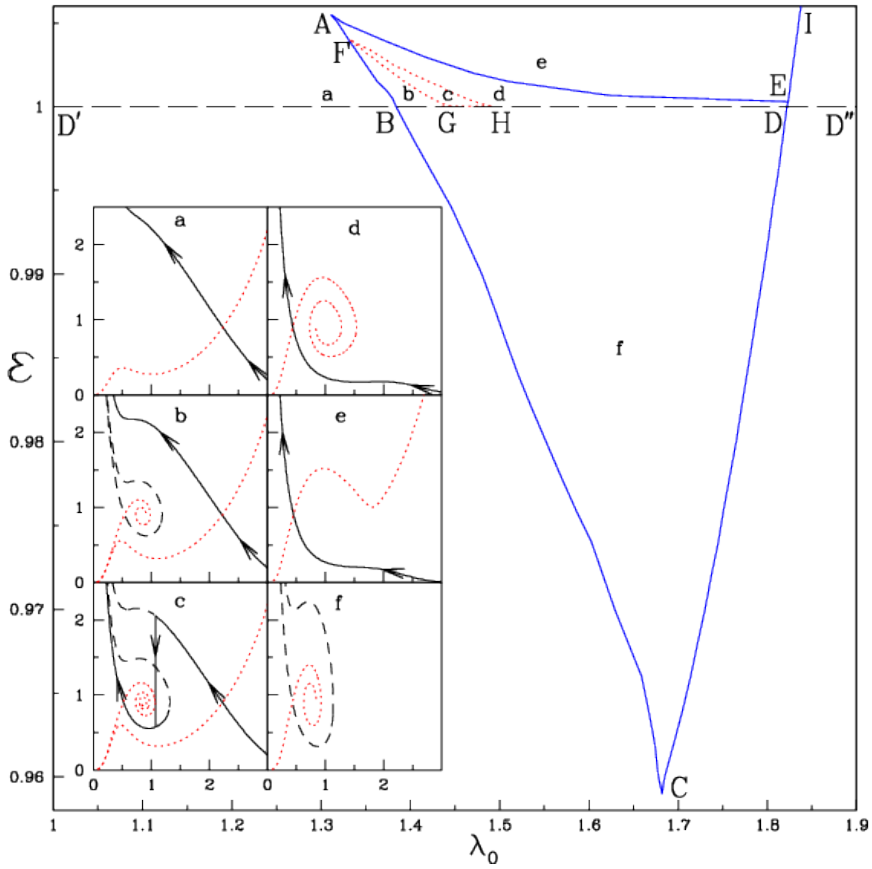

Figure 4.11: Division of parameter space - Division of the parameter space in $\varepsilon - \lambda_0$ according to number of critical points and representative accretion solutions. Area ABDEA and BCDB has three and two critical points, respectively. Area outside the bounded region D′BAEI and $\varepsilon > 1$ has single critical point, but for regions outside D′BCDEI and $\varepsilon < 1$ no critical points exit. Inset panels labelled as a, b, c, d, e, and f present Mach number $M = \vartheta/a$ versus $\log(x)$, corresponding to the ε, λ_0 values at the locations marked in the parameter space. The dotted region FGHF is the shock parameter space, and in panel (c) the vertical jump shows the position of the shock. Accretion solutions are represented by solid curve. This parameter space and the associated solutions are for $\alpha = 0.05$, $\beta = 0.01$ and $\dot{m} = 0.1$. Kumar & Chattopadhyay (2014).

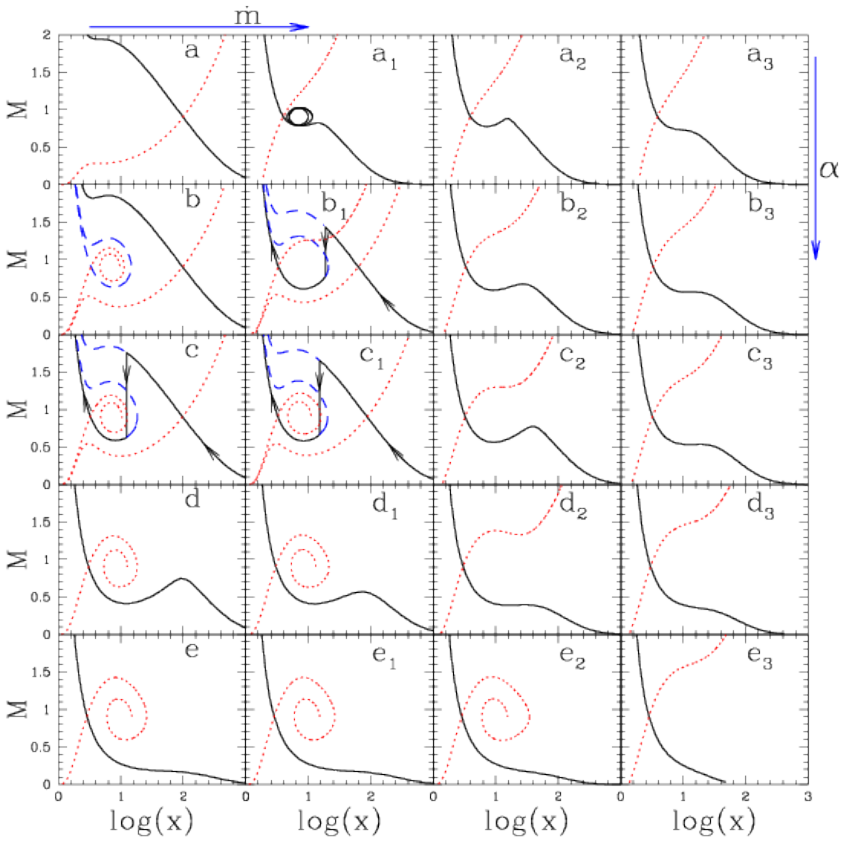

Figure 4.12: Effect of α and $\dot{m}$ - Effect of accretion rate and the viscosity parameter on shock-free inviscid flow. The Mach number M are plotted with $\log(x)$ in all the panels, for parameters $\varepsilon = 1.001$, $\lambda_0 = 1.46$, $\beta = 0.1$ and $\xi = 1.0$. (a) Shock free solution with only $x_{\rm co}$ in the inviscid limit. Vertically down $\downarrow$ viscosity increases *e.g.,*(a - e), $\alpha = 0.0,\ 0.025,\ 0.03,\ 0.048$ and 0.065, respectively, and $\chi = 0.0$. Left to right, $\dot{m}$ increases. For panels $a_1 - a_3$, we have cooling *i.e.,*$\chi = 1.0$ and the accretion rates are $\dot{m} = 3.5, 4.0$ and 5.0. For panels $b_1 - b_3$, $\chi = 1.0$ and $\dot{m} = 0.7,\ 1.4$ and 2.1. For panels $c_1 - c_3$, $\chi = 1.0$ and $\dot{m} = 0.2,\ 0.8$ and 1.6. For panels $d_1 - d_3$, $\chi = 1.0$ and $\dot{m} = 0.1,\ 0.5$ and 1.0. For panels $e_1 - e_3$, $\chi = 1.0$ and $\dot{m} = 0.01, 0.1$ and 1.0. Wind type solutions are plotted as dotted curve and dashed part of the transonic solution which is not followed by the flow. Kumar & Chattopadhyay (2014).

The solutions or the Mach number distributions M $(= \vartheta/a)$ for various parameters are plotted in the inset. In Fig. 4.11, the inset panel labelled 'a' presents M versus $\log(x)$, corresponding to location 'a' in the energy-angular momentum parameter space for coordinates $(\varepsilon, \lambda_0 = 1.0005, 1.3)$. Increasing λ_0, we move to locations 'b' $(\varepsilon, \lambda_0 = 1.0005, 1.41)$, 'c' $(\varepsilon, \lambda_0 = 1.0005, 1.425)$ and 'd' $(\varepsilon, \lambda_0 = 1.0005, 1.52)$. And then for higher ε, solution of panel 'e' represents solution corresponding to location 'e' $(\varepsilon, \lambda_0 = 1.003, 1.55)$, and panel 'f' corresponds to solution for $(\varepsilon, \lambda_0 = 0.985, 1.6)$. The global transonic accretion solutions in the inset are represented by solid curve (black), and solutions which represent wind-type solutions are represented by the dotted curve (red). The dashed curve represents the transonic solution through which matter may pass. Accretion flows with any value of ε and λ_0 in the bounded region ABDEA has three sonic points, and have a combination of closed and global solutions (*e.g.,*Figs. 4.11b - e). In the domain of multiple sonic points, if the steady shock solution cannot be obtained, and in addition, the solution through $x_{\rm co}$ does not connect the horizon and infinity, then the solutions through $x_{\rm co}$ cannot be determined exactly, and so, only solutions through inner sonic point are shown for Fig. 4.11d. The rough location of $x_{\rm co}$ can be ascertained for Fig. 4.11d, at the location where global solution through $x_{\rm ci}$ (solid, black), shows a maximum. An ADAF-type solution, *i.e.,*monotonic M distribution through $r_{\rm ci}$, is shown in Fig. 4.11e. On the other hand, flows with ε and λ_0 in the region BCDB have two critical points, and produces only closed topologies and therefore no global transonic solution (Fig. 4.11f). Within ABDEA, the bounded region FGHF produces steady, non-dissipative shocked solutions (*e.g.,*Fig. 4.11c), which are obtained from equations (2.27)-(2.30). The region outside BAEI and $\varepsilon \geq 1$, there is only one sonic point (*e.g.,*Figs. 4.11a & f). Figure 4.11a, has low angular momentum and therefore produces a Bondi-type solution characterized by a single sonic point far away from the horizon, even in presence of dissipation. Figure 4.11e, on the other hand, produces a solution which is mostly subsonic and becomes transonic close to the horizon, and is similar to ADAF-type solutions. Regions outside D′BCD and $\varepsilon < 1$ and right of the curve DI, there exists no critical point, and consequently steady state black hole accretion is not allowed for such inner boundary conditions. The coordinates of the important points which represents the multiple sonic point domain in the energy-angular momentum parameter space are A $(1.0055, 1.311)$, B $(1.0, 1.385)$, C $(0.959, 1.682)$, D $(1.0, 1.822)$ and E $(1.0003, 1.824)$.

We have shown that how solutions of electron-proton flow depend on ε and λ_0 for given values of α, β and $\dot{m}$, we now present dependence of advective solutions on α and $\dot{m}$ for given values of ε and λ_0. We choose flow parameters $(\varepsilon,\ \lambda_0) = (1.001, 1.46)$ which produces shock-free solution with a single $x_{\rm co}$-type sonic point in the inviscid limit, *i.e.,*for $\alpha = \chi = 0$ (Fig. 4.12a). Panels on the left, Figs. 4.12(a) - (e), represent solutions without cooling *i.e.,*$\chi = 0.0$, but increasing viscosity $\alpha = 0.025$ (Fig. 4.12b), $\alpha = 0.03$ (Fig. 4.12c), $\alpha = 0.048$ (Fig. 4.12d), $\alpha = 0.065$ (Fig. 4.12e). We show that a shock-free solution through a single $x_{\rm co}$ in the inviscid limit (Fig. 4.12a), enters into multi-critical point domain (Fig. 4.12b), and eventually generates shock (Fig. 4.12c) as α is increased for the same inner boundary condition *i.e.,*$\varepsilon - \lambda_0$. Further increase of α removes steady shock while still being in the multi-critical point domain (Fig. 4.12d), and eventually produces a monotonic shock-free solution through $x_{\rm ci}$ or ADAF type solution. In Figs. 4.12(a)-(a_3), the solutions are inviscid, but $\dot{m}$ is increased step by step to values 3.5 (Fig. 4.12a_1), 4.0 (Fig. 4.12a_2), and 5.0 (Fig. 4.12a_3). For Figs. 4.12 (b_1)-(b_3), $\alpha = 0.025$ (same as Fig. 4.12b), $\dot{m}$ varies from 0.7, 1.4 and 2.1, respectively. For Figs. 4.12(c_1)-(c_3), α is same as in Fig. 4.12c, but $\dot{m}$ varies as 0.2, 0.8 and 1.6, respectively. The accretion rate $\dot{m}$ increases from 0.1 in Fig. 4.12d_1, to 0.5 in Fig. 4.12d_2 and then up to 1.0 in Fig. 4.12d_3, and has the same α as Fig. 4.12d. On the other hand, α of Fig. 4.12e is used for Figs. 4.12(e_1)-($2e_3$), but accretion rates are $\dot{m} = 0.01$ (Fig. 4.12e_1), $\dot{m} = 0.1$ (Fig. 4.12e_2) and $\dot{m} = 1.0$ (Fig. 4.12e_3). Therefore, it is clear that the very inner boundary condition (read $\varepsilon\ -\ \lambda_0$) which produces a shock-free, monotonic solution with only one $x_{\rm co}$ sonic point in the inviscid limit, for different α and $\dot{m}$ will produce such varied λ and Θ distributions that would generate solutions comprising multiple-sonic points, shocks, or monotonic ADAF-type solutions.

In Figs. 4.13 (a)-(h), we compare accretion solutions by varying α, χ or $\dot{m}$ but for either same inner boundary condition (IBC) or same outer boundary condition (OBC). In Figs. 4.13 (a)-(d) we plot M, and in Figs. 4.13 (e)-(h) we plot $\log(\lambda)$ with $\log(x)$. Each pair of horizontal panels show the Mach number and angular momentum distribution of flows with same boundary condition. For example, Figs. 4.13 (a) and (e) presents M and $\log(\lambda)$ distribution of accretion flows with same inner boundary condition, *i.e.,*$\varepsilon = 1.0001$, and $\lambda_0 = 1.577$, where each curve represents $\alpha = 0.0,\ \chi = 0.0$ (solid, black), $\alpha = 0.01,\ \chi = 0.0$ (dotted, red) and $\alpha = 0.01,\ \chi = 1.0$ (dashed, blue).

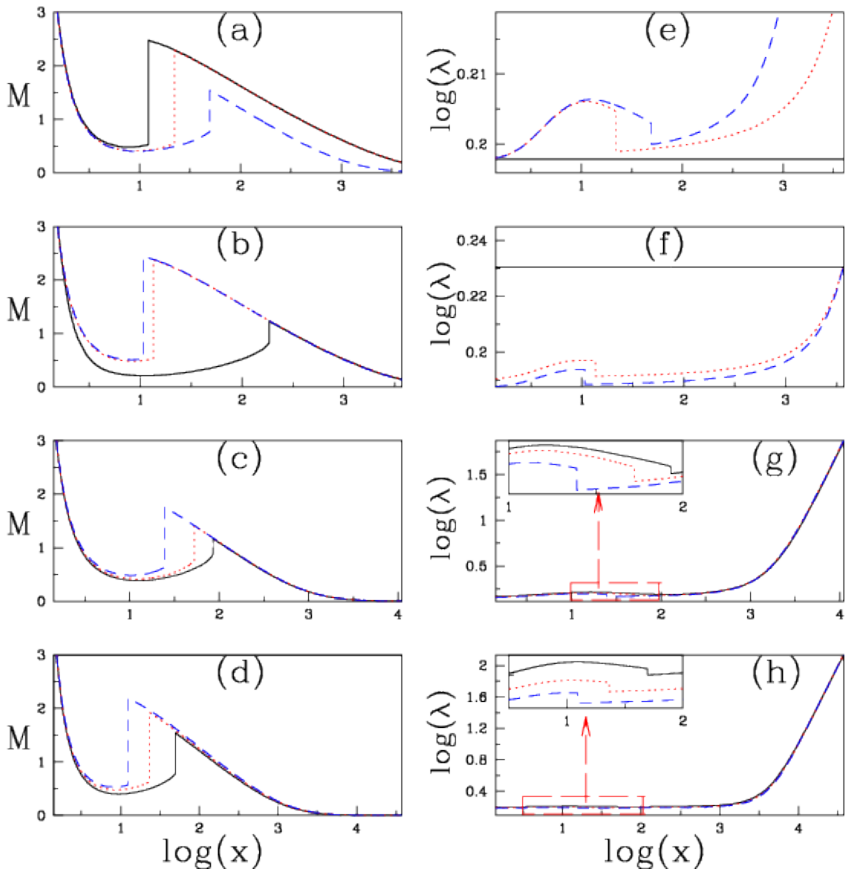

Figure 4.13: Effect of α and $\dot{m}$ with fixed either OBC or IBC - Variation of M (a-d) and corresponding $\log(\lambda)$ (e-h) with $\log(x)$, for $e^- - p^+$ flow. Solutions (a and e) are plotted for same $\varepsilon = 1.0001,\ \lambda_0 = 1.577$. Each curve corresponds to $\alpha = 0.0,\ \chi = 0.0$ and a shock at $x_s = 12.2236$ (solid, black), $\alpha = 0.01,\ \chi = 0.0$ and a shock at $x_s = 22.1412$ (dotted, red) and $\alpha = 0.01,\ \chi = 1.0$ and a shock at $x_s = 49.4872$ (dashed, blue). Each curve in (b and f) is generated for $\alpha = 0.0,\ \chi = 0.0$ with $x_s = 183.9687$ (solid, black), $\alpha = 0.01,\ \chi = 0.0$ with $x_s = 13.5259$ (dotted, red) and $\alpha = 0.01,\ \chi = 1.0$ with $x_s = 10.6728$ (dashed blue), but for same outer boundary conditions $\lambda_{inj} = 1.7,\ \Theta_{inj} = 9.811 \times 10^{-2}$ and $\vartheta_{inj} = 1.928 \times 10^{-3}$, at $x_{inj} = 3686.02$. Plots a and e, b and f have common parameters, $\beta = 0.1$ and $\dot{m} = 0.1$. Each curve in (c and g) is plotted with $\alpha = 0.0494$ and produces a shock at $x_s = 85.1545$ (solid, black), $\alpha = 0.0534$ and $x_s = 52.3582$ (dotted, red), $\alpha = 0.0545$ and $x_s = 24.5147$ (dashed, blue) and $\chi = 1.0$ but keeping other parameters, $\lambda_{inj} = \lambda_K(x_{inj}) = 74.12, \Theta_{inj} = 0.3999$ and $\vartheta_{inj} = 4.3568 \times 10^{-5}$ fixed at the outer boundary $x_{inj} = 10986.38$ with $\beta = 0.01,\ \dot{m} = 0.1$. Each curve in (d) and (h) are plotted with different accretion rates $\dot{m} = 0.1$ (solid, black), 0.3 (dotted, red) and 0.5 (dashed, blue) and $\alpha = 0.01, \beta = 0.1$ are fixed. We keep $\lambda_{inj} = \lambda_K(x_{inj}) = 136.67, \Theta_{inj} = 3.554$ and $\vartheta_{inj} = 1.1571 \times 10^{-5}$ are fixed at the outer boundary $x_{inj} = 37354.32$. The shocks are at $x_s = 49.4872$, 23.13107 and 12.3237, respectively. Kumar & Chattopadhyay (2014).

Clearly, $\lambda = \lambda_0$ is a constant of motion for inviscid and adiabatic solution. Evidently, the shock recedes as viscosity is turned on ($x_{\rm s} = 12.2236 \rightarrow 22.1412$), and then further recedes to $x_{\rm s} = 49.4872$ as the cooling is turned on over and above the viscous dissipation. Since the effect of viscosity is to reduce angular momentum inwards, and the effect of cooling is to reduce temperature inwards, therefore, keeping same inner boundary and increasing viscosity and cooling implies both angular momentum and temperature increases outwards. Higher temperature and angular momentum means the shock front is shifted outwards. In Figs. 4.13 (b) and (f), we again compare inviscid flow (solid, black), with flow in presence of viscosity, *i.e.,*$\alpha = 0.01$, and $\chi = 0.0$ (dotted, red), and viscous flow in presence of cooling ,*i.e.,*$\alpha = 0.01$, $\chi = 1.0$ (dashed, blue), but now the flows are launched with the same outer boundary condition, *i.e.,*$\lambda_{\rm inj} = 1.7$, $\Theta_{\rm inj} = 9.811 \times 10^{-2}$ and $\vartheta_{\rm inj} = 1.928 \times 10^{-3}$, at the injection radius $x_{\rm inj} = 3686.02$. The accretion rate is $\dot{m} = 0.1$ and $\beta = 0.1$ for the flow with $\chi = 1$. Since in this case we start with the same temperature, angular momentum and velocity at the outer boundary, viscosity and cooling processes decrease both λ and Θ inwards. Therefore, for flows starting with same outer boundary condition, the net effect of increasing viscosity and cooling is to reduce both the centrifugal force and the pressure, so the shock front shifts closer to the horizon for viscous fluid with and without cooling, compared to the inviscid flow. In Figs. 4.13c & g, we compare viscous flows in presence of cooling ($\beta = 0.01$, $\dot{m} = 0.1$ and $\chi = 1.$), and starting with the same outer boundary condition ($\lambda_{\rm inj} = \lambda_{\rm K}(x_{\rm inj}) = 74.12, \Theta_{\rm inj} = 0.3999$ and $\vartheta_{\rm inj} = 4.3568 \times 10^{-5}$ at $x_{\rm inj} = 10986.38$), but now for different viscosity parameters, namely, $\alpha = 0.0494$ (solid, black), 0.0534 (dotted, red), 0.0545 (dashed, blue). In the previous panel, the solution started with sub-Keplerian flow at the outer boundary. In this figure we compare flows with different α, but in presence of same cooling parameters, and starting with Keplerian angular momentum (indicated by suffix K) at the outer boundary. Increase of α shows that the reduction of λ causes the shock to shift inward (see inset), even in presence of cooling. This shows that $x_{\rm s}$ reduces with increasing α for flows starting with same outer boundary condition. In the next pair of panels Figs. 4.13 (d) and (h), we compare accretion solutions starting with the same outer boundary condition ($\lambda_{\rm inj} = \lambda_{\rm K}(x_{\rm inj}) = 136.67, \Theta_{\rm inj} = 3.554$ and $\vartheta_{\rm inj} = 1.1571 \times 10^{-5}$ at $x_{\rm inj} = 37354.32$), and same $\alpha = 0.01$, but different $\dot{m} = 0.1$ (solid, black), $\dot{m} = 0.3$ (dotted, red) and $\dot{m} = 0.5$ (dashed, blue), in other words, we study the effect of

cooling in a viscous flow starting with the same outer boundary condition. In this case, although cooling does not directly affect the angular momentum equation (3.3), but it affects the entropy equation and therefore the thermal energy, which reduces the post-shock pressure. As a result shock moves inwards with the increase of cooling. Since kinematic viscosity parameter (*i.e.*,ν, defined in equation 2.15) depends on both α and a^2, so cooling processes will affect a and thereby in an indirect way cooling processes will affect the angular distribution too, as is shown in Fig. 4.13h.

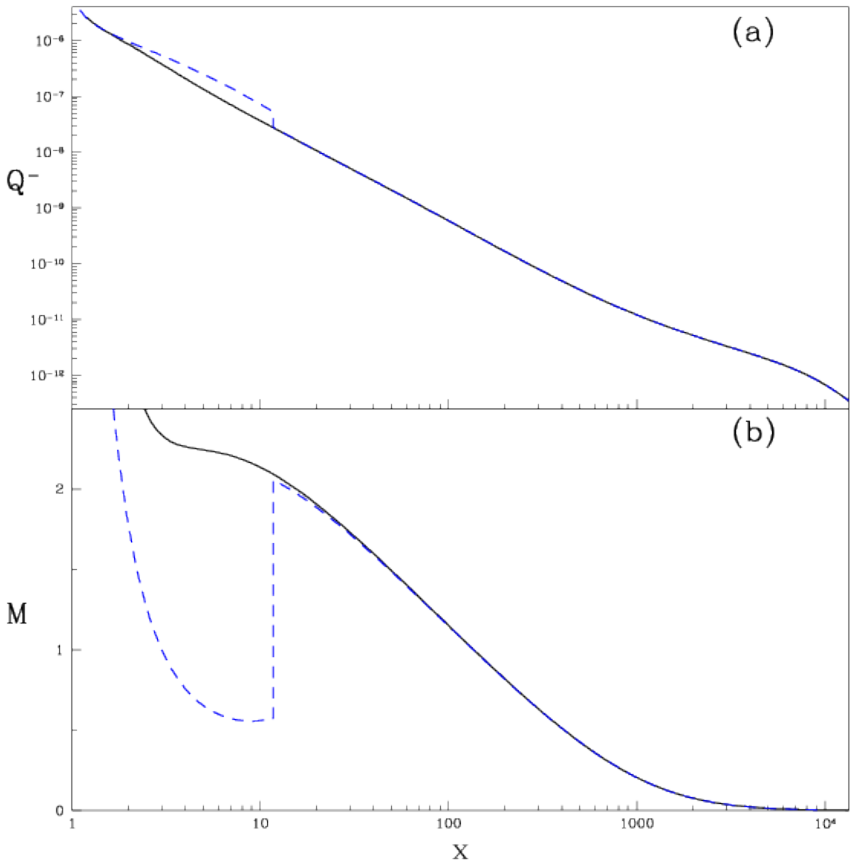

Figure 4.14: Variation of emissivity - Variation of emissivity per unit mass Q^- (a) and M (b) with x. Each curve represents a shock free (solid, black) and shocked accretion solution (dashed, blue) generated with the same $\lambda_{\rm inj} = \lambda_K(x_{\rm inj}) = 82.51$ at $x_{\rm inj} = 13614.44$, $\varepsilon = 1.0005$, $\beta = 0.01$ and $\dot{m} = 0.1$. The shocked solution is generated with $\alpha = 0.05$ and the shock free for $\alpha = 0.0505$. Both the solutions are for $e^- - p^+$ flow. Luminosities for shock free and shocked solutions are $\ell = 1.40 \times 10^{-4}$ and 1.67×10^{-4}, respectively. Kumar & Chattopadhyay (2014).

We compare the emissivity per unit mass *i.e.,*Q^- (Fig. 4.14a) and the Mach number M (Fig. 4.14b) between a shock free (solid, black) and a shocked (dashed, blue) accretion solution, starting with the same outer boundary condition $\varepsilon = 1.0005$, $\beta = 0.01$ and $\dot{m} = 0.1$ and $\lambda_{\rm inj} = \lambda_{\rm K}(x_{\rm inj}) = 82.51$ at $x_{\rm inj} = 13614.44$. The shocked solution is generated with $\alpha = 0.05$ and the shock-free for $\alpha = 0.0505$. Although the radiative output is almost similar in the outer regions, but the post shock flow is more luminous. The over all luminosity of shocked solution is more compared to the shock free solution, even for flow with same composition, outer boundary condition and $\dot{m}$. Although we can choose to compare even hotter shock free and shocked solutions, but the greater Comptonization efficiency of shocked solution will in general be more luminous and will also produce a harder spectrum.

In Fig. 4.15a, we plot the non-dissipative shock parameter space (SPS) $\varepsilon - \lambda_0$ of accretion flow in presence of cooling ($\chi = 1$, $\beta = 0.01$, and $\dot{m} = 0.1$), but for different viscosity parameters $\alpha = 0.01$ (solid, black), 0.05 (dotted, red), 0.1(dashed, blue), 0.2 (long-dashed, cyan), and 0.3 (dotted-dashed, magenta). One can obtain steady shocks at $\alpha > 0.3$ in presence of cooling too. In Fig. 4.15b, we plot shock parameter space $\varepsilon - \lambda_0$ of accretion flow for a particular $\alpha = 0.01$ but for different accretion rate $\dot{m} = 0.1$ (solid, black), 1.0 (dotted, red), 10.0(dashed, blue) and 20.0 (long-dashed, cyan), however, with synchrotron processes ignored, *i.e.,*$\beta = 0$. It is interesting to note that shocked accretion solution can be obtained for fairly high α and $\dot{m}$.

4.2.2.1 Dissipative shock in accretion flow

All shocked solutions presented in the preceding subsection have been examples of non-dissipative shocks ($f_e = 0$) obtained by solving equation (4.18). However, we have also discussed, if the energy flux is not conserved and still there is a shock, then that would be considered as a dissipative shock ($f_e = 0$) but conserving E instead of ε in presence of cooling($\chi \neq 0$). The dissipative and non-dissipative shock solutions are presented Fig.4.16. In this figures, we compare accretion solutions starting with the same outer boundary condition [$\varepsilon = 1.000021, \lambda_{\rm inj} = \lambda_K(x_{\rm inj}) = 109.19$ at $x_{\rm inj} = 23842.73$], same $\alpha = 0.01$, $\beta = 0.01$ and $\dot{m} = 1$, but one solution harbours dissipative shock (solid black) and the other solution harbours non-dissipative shock (dashed blue). We compare M (Fig. 4.16a), $log(\lambda)$ (Fig. 4.16b), ε (Fig. 4.16c) and E (Fig. 4.16d) as a

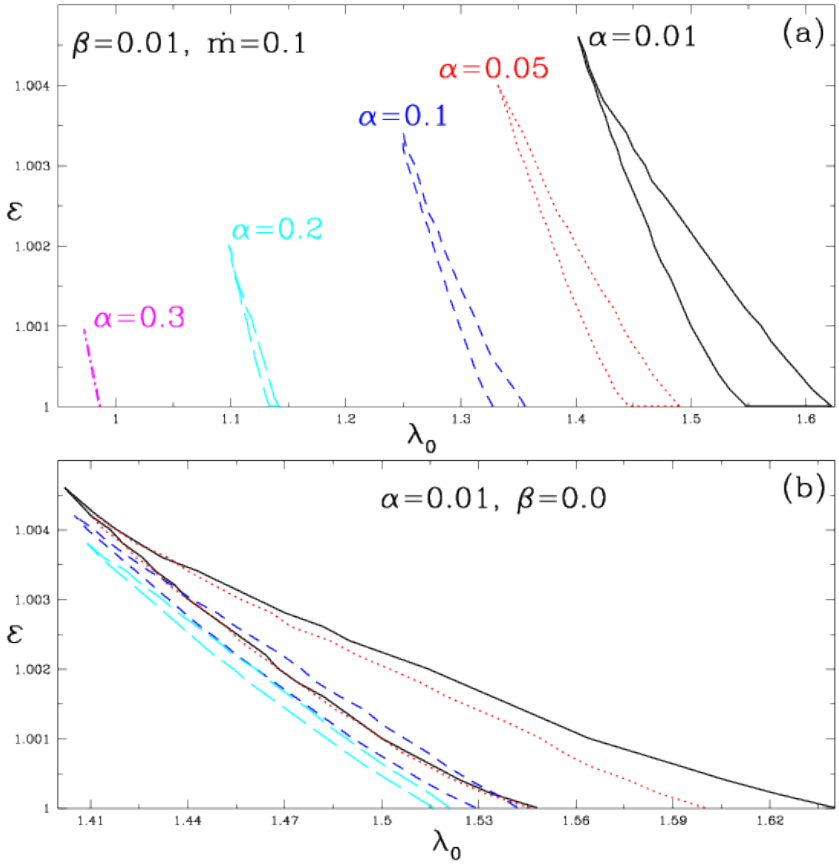

Figure 4.15: Non-dissipative SPS - (a) Non-dissipative shock parameter space (SPS) with general Bernoulli parameter (ε) versus specific angular momentum (λ_0) for $\alpha = 0.01$ (solid, black), 0.05 (dotted, red), 0.1 (dashed, blue), 0.2 (long-dashed, cyan) and 0.3 (dotted-dashed, magenta) and with constant cooling parameters, $\dot{m} = 0.1$ and $\beta = 0.01$. (b) ε-λ_0 parameter space for non-dissipative shock for different $\dot{m} = 0.1$ (solid, black), 1.0 (dotted, red), 10.0 (dashed, blue) and 20.0(long-dashed, cyan) and keeping $\alpha = 0.01$ and $\beta = 0.0$ fixed. Both the plots are for $e^- - p^+$ flow. Kumar & Chattopadhyay (2014).

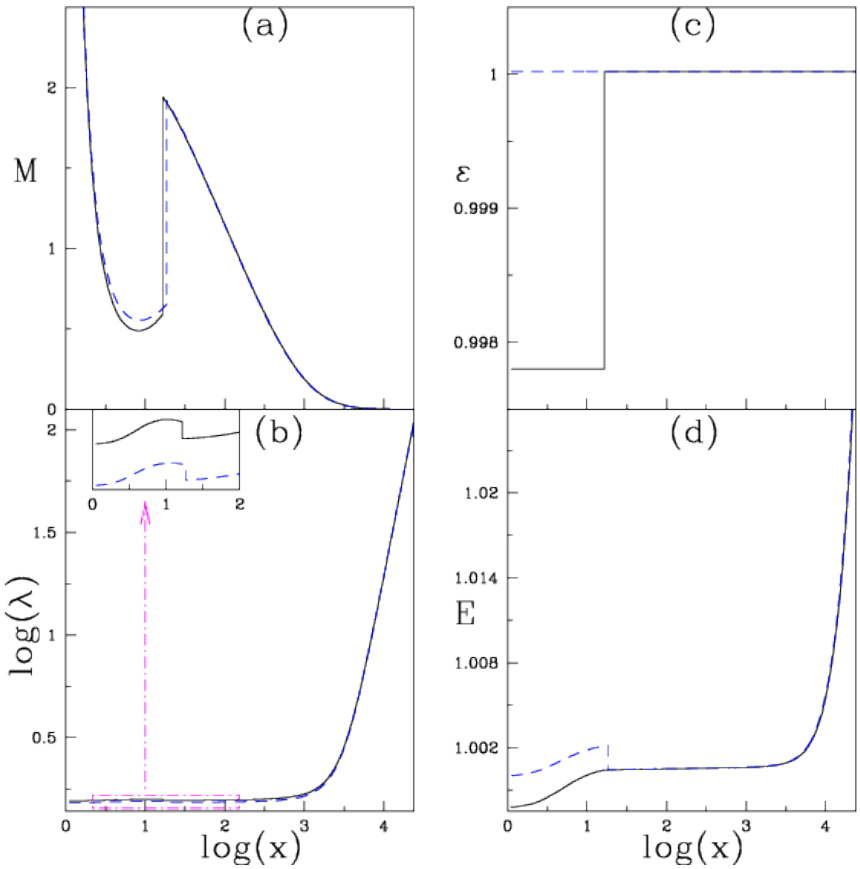

Figure 4.16: Comparison of non-dissipative and dissipative shocks - Variation of various physical quantities of the accretion flow such as Mach number M in plot (a), specific angular momentum λ in plot (b), general Bernoulli parameter ε in plot (c), and grand specific energy E in plot (d) are plotted with radial distance $log(x)$. In all plots solid (black) curves represent dissipative shock and dashed (blue) curves represent non-dissipative shock solutions and having shock locations at 16.61 and 18.51, respectively. The solutions are generated for $\alpha = 0.01$, $\beta = 0.01$, and $\dot{m} = 1$. Outer boundary condition is $\varepsilon = 1.000021, \lambda_{\rm inj} = \lambda_K(x_{\rm inj}) = 109.19$ at $x_{\rm inj} = 23842.73$. For dissipative shock, the energy dissipated at the shock is $\Delta\varepsilon = 0.00221$. Kumar & Chattopadhyay (2014).

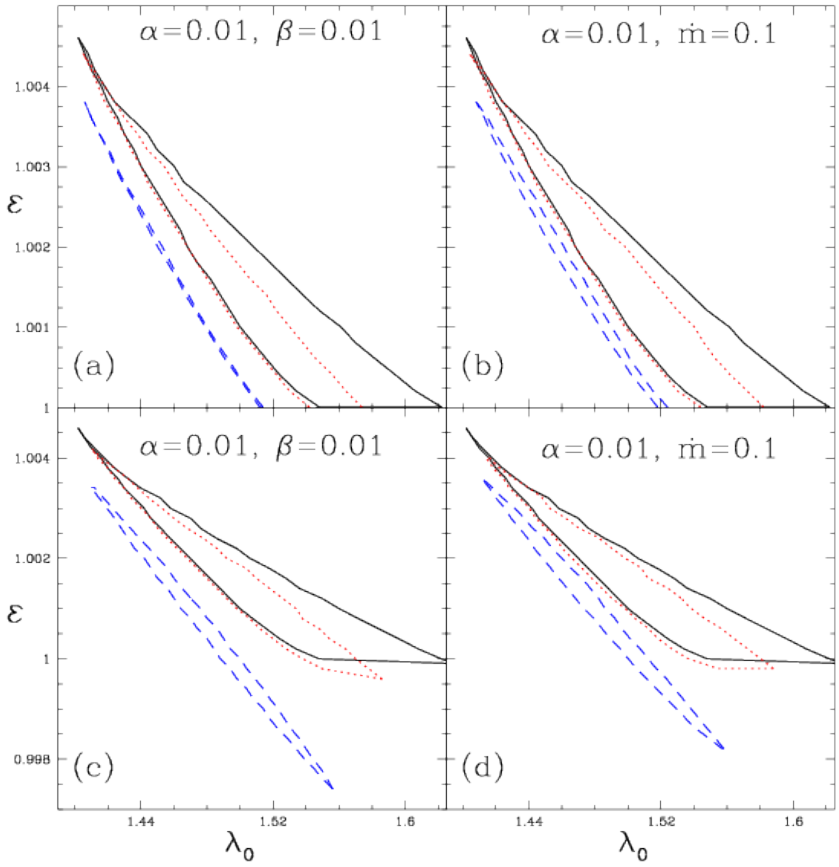

Figure 4.17: SPS for non-dissipative and dissipative shocks - $\varepsilon - \lambda_0$ parameter space for non-dissipative (a and b) and dissipative (c and d) shocks in the flow. Bounded regions in (a, c) are plotted with different accretion rates, $\dot{m} = 0.1$ (solid line), 1.0 (dotted line) and 10.0 (dashed line) but keeping $\beta = 0.01$ fixed, and regions in (b, d) are plotted with different $\beta = 0.01$ (solid line), 0.1 (dotted line) and 1.0 (dashed line) but keeping $\dot{m} = 0.1$ fixed. All plots are for the same viscosity parameter, $\alpha = 0.01$. Kumar & Chattopadhyay (2014).

function of $log(x)$. Conservation of E across the shock is equivalent to a discontinuous decrement in ε across the shock (solid curve in Fig. 4.16c), corresponding to an energy dissipation of $\Delta\varepsilon = 0.00221$. Compared to the non-dissipative shock, the dissipative shock forms closer to the horizon because of $\Delta\varepsilon$ released at the dissipative shock. It is also clear from Figs. 4.16c and d, that ε is a constant of motion in presence of viscous dissipation and cooling processes, and E is not. In Figs. 4.17a-d, we plot the $\varepsilon - \lambda_0$ shock parameter space for non-dissipative shock (Figs. 4.17a and b) and dissipative shocks (Figs. 4.17c & d). In Figs. 4.17a and c, the steady shock parameter space are bounded regions for $\dot{m} = 0.1$ (solid, black), $\dot{m} = 1$ (dotted, red), and $\dot{m} = 10$ (dashed, blue), all the plots are generated for given values of $\alpha = 0.01$ and $\beta = 0.01$. In Figs. 4.17b and d, the shock parameter space are the bounded regions characterized by $\beta =$ 0.01 (solid line), 0.1 (dotted line) and 1.0 (dashed line) but keeping $\alpha = 0.01$, and $\dot{m} =$ 0.1 fixed. So in Figs. 4.17a and c, we compare non-dissipative and dissipative shocks for same proportion of synchrotron losses but different mass supply, and in Figs 4.17b and d, we compare non-dissipative and dissipative shocks for same mass supply but different synchrotron losses. We kept the viscosity parameter same to see the effect of $\dot{m}$ and β. Clearly the parameter ranges for dissipative steady shock is larger. Evidently, the combined parameter space for both non-dissipative and dissipative shocks is quite significant. From Figs. 4.15a-b and 4.17a-d, it is clear that steady shock may exist for fairly extreme flow parameters like super Eddington accretions rates, $\alpha \gtrsim 0.3$, and fairly high magnetic energy.

4.2.2.2 Hyper-accretion rate

In Figs. 4.18a and c, we plot shock parameter spaces *i.e.,*bounded region of $\dot{m} - \lambda_0$ and the corresponding $\ell - \lambda_0$ for a viscosity parameter $\alpha = 0.01$, and in Figs. 4.18b and d, the $\dot{m} - \lambda_0$ and $\ell - \lambda_0$ shock parameter spaces for $\alpha = 0.05$. Each curve are plotted for $\varepsilon = 1.0001$ (solid, black) and $\varepsilon = 1.001$ (dotted, red). For all the plots $\chi = 1$ and $\beta = 0.01$. It is interesting to note that a steady shock can form in accretion flow even for super Eddington accretion rate, and can also radiate on or above Eddington luminosity. The efficiency of conversion of accretion power to radiation also varies, for example we consider two accretion solutions corresponding to $\varepsilon = 1.0001$ and $\alpha = 0.01$, and $\lambda_0 = 1.57$ (S_1) and $\lambda_0 = 1.515$ (S_2). The dimensionless temperature Θ of the two solutions are plotted with x in log-log scale and are presented in the inset of Fig.

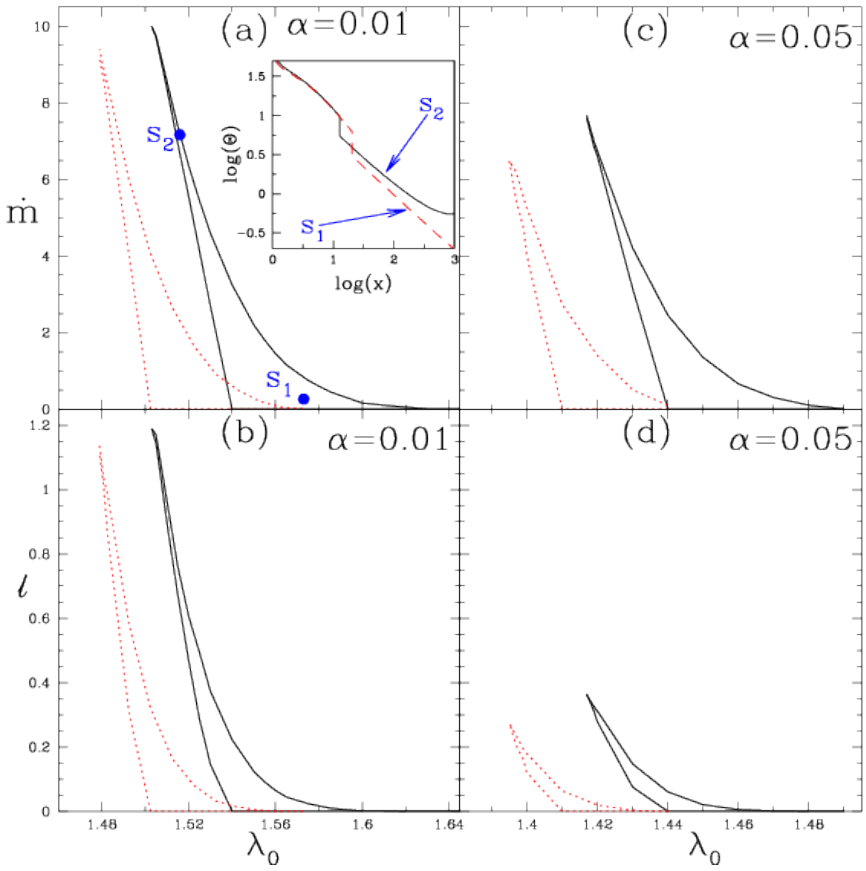

Figure 4.18: SPS and luminosities - Shock parameter space $\dot{m} - \lambda_0$ in panels (a and c) and corresponding luminosities ℓ in panels (b and d). Plots (a and b) are generated for viscosity parameter, $\alpha = 0.01$ and plots (c and d) are generated for $\alpha = 0.05$. Each curve corresponds to, $\varepsilon = 1.0001$ (solid line) and 1.001 (dotted line). We keep $\beta = 0.01$ same for all the plots. Inset in (a), Θ as a function of $x$in log-log scale. Solution S_1 (shown in $\dot{m} - \lambda_0$ space) $\varepsilon = 1.0001$, $\lambda_0 = 1.57$, $\alpha = 0.01$, $\beta = 0.01$, $\dot{m} = 0.1$, $x_s = 20.02547$ and disc luminosity $\ell = 2.766 \times 10^{-4}$. Solution S_2 (shown in $\dot{m} - \lambda_0$ space) is for $\varepsilon = 1.0001$, $\lambda_0 = 1.515$, $\alpha = 0.01$, $\beta = 0.01$, $\dot{m} = 7.0$, $x_s = 12.73524$ and disc luminosity $\ell = 0.677$. All the plots are for $e^- - p^+$ flow. Kumar & Chattopadhyay (2014).

4.18a. S_1 corresponds to $\dot{m} = 0.1$ and $\ell = 2.766 \times 10^{-4}$ and S_2 corresponds to $\dot{m} = 7$ and $\ell = 0.677$. The radiative efficiency defined as $\ell/\dot{m}$ of S_1 is $\lesssim 10^{-3}$, while for S_2 the efficiency is ~ 0.1. Therefore, the range of radiative efficiency obtained from our solutions, spans from radiatively inefficient advective flow to radiatively luminous regime, and solely depends on the outer boundary conditions. So the cycle of low luminosity to luminous but intermediate hard states in micro-quasars can be addressed if all the solutions in the advective regime be considered.

4.2.3 Accretion-ejection in dissipative flow

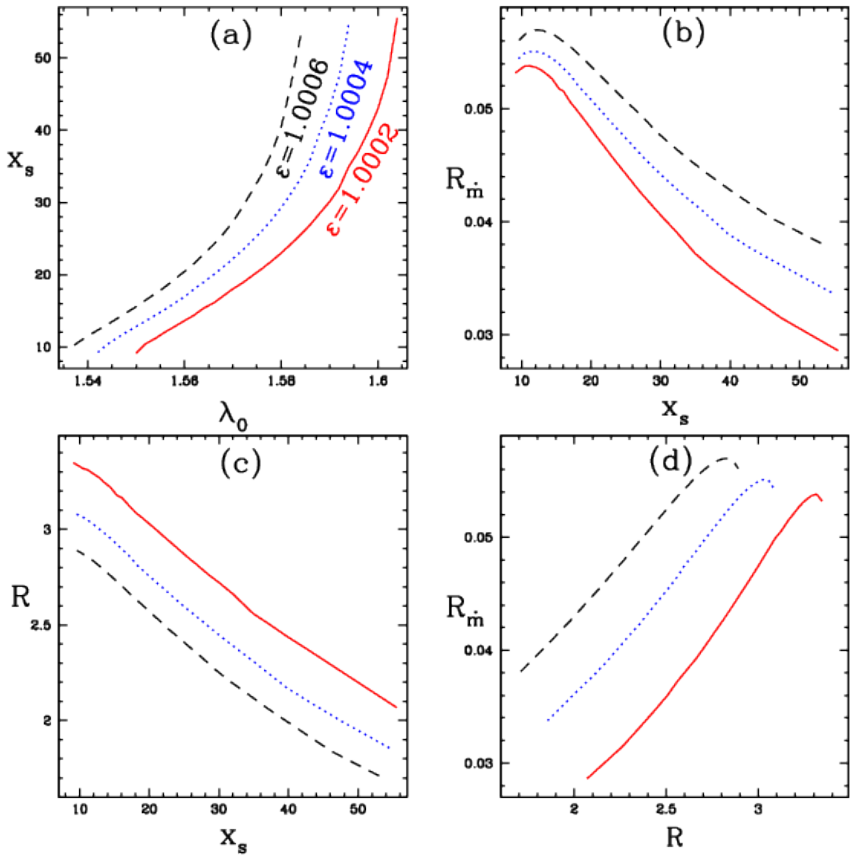

Figure 4.19: Mass outflow rate in dissipative disc - Plot (a) Shock location, x_s versus λ_0, (b) outflow rate $R_{\dot{m}}$ with x_s, (c) compression ratio, $R = v_-/v_+$ with x_s and (d) $R_{\dot{m}}$ with R. Each curve corresponds to constant general Bernoulli parameters, $\varepsilon = 1.0002$ (solid line), 1.0004 (dotted line) and 1.0006 (dashed line) and other parameters, $\alpha = 0.01, \xi = 1.0, \beta = 0.01$ and $\dot{m} = 0.1$.

Here accretion-ejection solutions and outflow rate (3.23) are calculated by a method similar to that of the previous section (4.1). In fig. (4.19), we have plotted x_s with λ_0 in plot (4.19a), $R_{\dot{m}}$ with x_s in (4.19b), R with x_s in (4.19c) and $R_{\dot{m}}$ with R for composition parameter $\xi = 1.0$ and each curve plotted for different ε. In plot (4.19a), x_s increases with ε for a given λ_0 and similarly for a given x_s, $R_{\dot{m}}$ increases in plot (4.19b) but R decreases in plot (4.19c) with increasing ε. This means $R_{\dot{m}}$ increases with ε. $R_{\dot{m}}$ initially increases with increasing R, but maximizes at some value and then start to decrease (Fig.4.19d). Very small R means the shock is located at large distance, obviously the thermal driving would be less since the average post shock temperature is lower for large x_s. As R increases, *i.e.,*x_s decreases, the flow gets hotter and hotter post-shock disc can drive larger fraction of accreting matter as jets so $R_{\dot{m}}$ increases. However decreasing x_s means smaller post-disc. So till some optimal value of x_s, the thermal driving maximizes and dominates the decreasing volume of the post-shock disc, beyond that, $R_{\dot{m}}$ decreases with increasing R. So, dissipative flow qualitatively follow the same trend in $R_{\dot{m}}$ as in adiabatic flow, shown in Kumar et al. (2013).

4.3 Study of advective accretion disc in General relativistic approach:

Up till now, we have studied the black hole accretion ejection system with the help of a pseudo potential obtained by Paczyńsky & Wiita (1980). For micro-quasars, observations by Fender et al. (2010) showed very little evidence of the role of black hole spin in driving jets via Blandford-Znajek mechanism (Blandford & Znajek 1977). Although the same has not been shown for AGN or quasar jets, but the morphological similarity of micro-quasar and quasar jets prompts the community to expect similar properties for jets around larger black holes too. This in effect means that the formation of jets has more to do with the plasma physics in strong gravity, rather than the properties of the space-time only. Therefore, we are quite justified to consider non-rotating black hole, so that we can focus on the plasma physics part and not digress on the characteristics of the space time. However, what is not justified, is to draw definitive conclusions only on the basis of it, since PW potential itself violates the basic tenets of relativity close to the horizon. It is because of these problems that we attempted to study the accretion-ejection system in pure general relativity. However, the problem is compounded by the

lack of a thorough investigations of advective, transonic dissipative solutions in general relativity, and therefore makes the problem more challenging.

In this section, we present rotating, steady-state, viscous accretion disc in vertically hydro-static equilibrium around Schwarzschild black holes with relativistic multispecies EoS (Chattopadhyay 2008; Chattopadhyay & Ryu 2009). The relativistic fluid equations (2.48 - 2.47) are simplified with the help of viscous shear rate equation (2.53), assuming $Q^- = 0$ and EoS (2.70). Here we have chosen geometrical unit system as $G = M_B = c = 1$. We present spatial derivative of flow variables v, l and Θ, and chronologically they are

$$\frac{dv}{dr} = \frac{\mathcal{N}}{\mathcal{D}}, \tag{4.20}$$

where, $\mathcal{N} = -\frac{1}{r(r-2)} + (\frac{r-3}{r-2})\frac{l^2}{r^3\gamma_v^2} + \frac{2a^2}{\Gamma+1}\left[\frac{\widetilde{t}u^r(L-L_0)^2}{8\nu r(r-2)(N+1)\Theta} + \frac{5r-8}{2r(r-2)} - \frac{l^2}{r^2\gamma^2}(\frac{1}{l}\frac{dl}{dr} - \frac{1}{r})\right]$,
$\mathcal{D} = \gamma_v^2[v - \frac{2a^2}{\Gamma+1}(\frac{l^2}{r^2\gamma^2}v + \frac{1}{v})]$ and sound speed defined as $a^2 = (\Gamma p)/(e+p) = (2\Gamma\Theta)/(f + 2\Theta)$.

spatial derivative of angular velocity (l),

$$\frac{dl}{dr} = \left[-\frac{u^r(L-L_0)}{\nu(1-\frac{2}{r})} + \frac{2l}{r}\right](1-v^2) \tag{4.21}$$

and spatial derivative of temperature (Θ),

$$\frac{d\Theta}{dr} = -\frac{\widetilde{t}u^r(L-L_0)^2}{2\nu r(r-2)(2N+1)} - \frac{2\Theta}{2N+1} \times \left[\frac{5r-8}{2r(r-2)} + \gamma_v^2\left(\frac{1}{v} + v\frac{l^2}{r^2\gamma^2}\right)\frac{dv}{dr} - \frac{l^2}{r^2\gamma^2}\left\{\frac{1}{l}\frac{dl}{dr} - \frac{1}{r}\right\}\right]. \tag{4.22}$$

These differential equations are again solved by using critical point conditions and L′hospital rule at critical point.

Sonic point conditions: Mathematical form of critical point equation is $dv/dr = 0/0$, which gives two equations as,

$$\mathcal{D}_c = 0 \quad \Longrightarrow \quad \left[1 - \frac{2}{\Gamma_c + 1}\left(\frac{a_c^2 l_c^2}{r_c^2\gamma_c^2} + \frac{a_c^2}{v_c^2}\right)\right] = 0 \tag{4.23}$$

and,

$$\mathcal{N}_c = 0 \quad \Longrightarrow \quad -\frac{1}{r_c(r_c-2)} + \left(\frac{r_c-3}{r_c-2}\right)\frac{l_c^2}{r_c^3\gamma_{v_c}^2} + \frac{2a_c^2}{\Gamma_c+1} \times \left[\frac{\widetilde{t}u_c^r(L_c-L_0)^2}{8\nu_c r_c(r_c-2)N_c\Gamma_c\Theta_c} + \frac{5r_c-8}{2r_c(r_c-2)} + \frac{l_c^2}{r_c\gamma_c^2}\left(\frac{u_c^r(L_c-L_0)}{\nu_c l_c\gamma_{v_c}^2(r_c-2)} - \frac{1-2v_c^2}{r_c^2}\right)\right] = 0. \tag{4.24}$$

where, radial four velocity $u_c^r = \sqrt{(1-2/r_c)}\ v_c\gamma_{v_c}$, total Lorentz factor $\gamma_c = \gamma_{v_c}\gamma_{\phi_c} = \sqrt{\gamma_{v_c}^2 + l_c^2/r_c^2}$, bulk velocity Lorentz factor $\gamma_{v_c} = 1/\sqrt{1-v_c^2}$ and angular Lorentz factor $\gamma_{\phi_c} = 1/\sqrt{1-v_{\phi_c}^2}$. Here, $v_{\phi_c} = \sqrt{\lambda_c\Omega_c} = l_c/(r_c\gamma_c)$ and subscript 'c' denotes the physical quantities at the location of critical point.

Shock conditions: The relativistic shock conditions are same as described in subsection (2.1.2) of chapter 2. So, relativistic shock conditions in presence of mass loss is written as,

$$\dot{M}_+ = \dot{M}_- - \dot{M}_{out};\ [\dot{J}] = 0;\ [\Sigma h u^{r2} + g^{rr}\mathrm{W}] = 0 \ \text{ and } \ [\dot{E}] = 0, \tag{4.25}$$

where, $\dot{J} = \dot{M}L_0 = \dot{M}(L - 2\nu\sigma_\phi^r/u^r)$, $\dot{E} = \dot{M}E$, $\Sigma = 2\rho H$ and $\mathrm{W} = 2pH$. We have solved four shock conditions (4.25) simultaneously, then we get relation between pre-shock and post-shock flow variables and are,

$$L_+ = L_-;\ h'_-u_-^2 - \mathrm{k}_1 u_- + 2\Theta_- = 0;\ \mathrm{k}_2 - \exp(X_{f\_})h'_-\gamma_{v-} = 0, \tag{4.26}$$

where, $\mathrm{k}_1 = (1-R_{\dot{m}})(h'_+u_+^2 + 2\Theta_+)/u_+$, $\mathrm{k}_2 = \exp(X_{f\_+})h'_+\gamma_{v+}$, $h' = (f + 2\Theta)$ and $u = v\gamma_v$. Here, $X_{f\_} = (f_l/f_\gamma)^2 X_{l+} + f_u f_L^2 X_{L+}/(f_\nu f_h)$, $X_{l+} = \int(\frac{r-3}{r-2})\frac{l_+^2}{r^3\gamma_{v+}^2}dr$, $X_{L+} = -\int\frac{u_+^r(L_+-L_0)^2}{2\nu_+h_+r(r-2)}dr$, $f_l = l_-/l_+$, $f_\gamma = \gamma_{v-}/\gamma_{v+}$, $f_u = u_-^r/u_+^r$, $f_L = (L_- - L_0)/(L_+ - L_0)$, $f_\nu = \nu_-/\nu_+$, $f_h = h_-/h_+$, and $X_{f\_+} = X_{l+} + X_{L+}$.

Spherical Outflow geometry :- For simplicity, we have assumed non-rotating and spherical outflow from the disc, so the relativistic fluid equations in spherical polar coordinate is written as, radial momentum equation,

$$u_j^r\frac{du_j^r}{dr_j} + \frac{1}{r_j^2} + \left(1 - \frac{2}{r_j} + u_j^r u_j^r\right)\frac{1}{e_j + p_j}\frac{dp_j}{dr_j} = 0, \tag{4.27}$$

The integrated from of continuity equation,

$$\dot{M}_{out} = 4\pi\rho_j u_j^r r_j^2(1 - cos(\theta_j)), \tag{4.28}$$

and entropy equation,

$$\frac{de_j}{dr_j} - h_j\frac{d\rho_j}{dr_j} = 0, \tag{4.29}$$

where, all the symbols have usual means but subscript 'j' represents flow variable for jet. Now mass outflow rate defined as,

$$R_{\dot{m}} = \frac{\dot{M}_{out}}{\dot{M}_-} = \frac{1}{[\Sigma_+ u_-^r r_s/(2R\rho_j u_{jb}^r r_{jb}^2(1 - cos(\theta_j))) + 1]}, \tag{4.30}$$

where, $\rho_j = \rho_e exp(-r_b/H_b), u^r_{bj}, r_{bj} = (r_c + r_s)/3$ and θ_j are jet base density, radial four-velocity at jet base, jet base radius and angle from vertical axis.

4.3.1 Solution procedure

Accretion solutions of dissipative flow in full general relativity is mathematically and technically very challenging, than those obtained by using the simplified pseudo-Newtonian potential. As in the case of PW potential, in general relativity too we do not know the location of the sonic point a priori. However, the major problem in general relativity is that the shear tensor itself do not go to zero on the horizon. Moreover, the shear tensor is far more complicated. The $r-\phi$ component of the shear tensor is not simply proportional to $d\Omega/dr$, but contains terms with radial four velocities and its derivatives, as well as, terms containing the angular speed Ω and u_ϕ and their derivatives. The other feature is the dependence of the angular momentum equation on the local enthalpy of the flow. In short all the equations are highly non-linear and solving them is non-trivial.

Since, close to the horizon gravity dominates all other physical process, so the infall timescale of matter will be smaller than viscous time scale or any other time scales. In other words, very close to the horizon matter is freely falling therefore, $E \simeq \mathcal{E}$. It may be remembered from chapter 2, that E is the generalized Bernoulli parameter (also known as grand specific energy parameter) in presence of viscosity and $\mathcal{E}$ is the canonical relativistic Bernoulli parameter. In steady state, for inviscid flow $\mathcal{E}$ is a constant of motion and for viscous flow E is a constant of motion. In addition, on the horizon matter is almost falling freely, therefore we assume that matter velocity is close to free fall velocity, i.e ., at a distance $r_{\rm in} \rightarrow r_g$, $v_{\rm in} = \delta\sqrt{2/r_{\rm in}}$. Here, $r_g = 2r_s = 2GM_B/c^2$, $r_{\rm in} = 2.001r_s$ and $\delta < 1$ is determine by iteration method and eventually satisfying critical point equations (4.23 and 4.24). These assumptions are helpful in finding correct asymptotic values of flow variables very close to the horizon, which are bulk velocity $v_{\rm in}$ and flow temperature $\Theta_{\rm in}$ and also bulk angular momentum (L_0) at the horizon by providing four flow parameters, constant of motion E, viscosity parameter α, composition parameter ξ and specific angular momentum $\lambda_{\rm in}$ at $r_{\rm in}$.

4.3.1.1 Method to find L_0 and Θ_{in}

We have provided four flow parameters (E, ξ, α and λ_{in} or L_{in}) and by using v_{in}, we can calculate Θ_{in} from relativistic Bernoulli equation $\mathcal{E} = -hu_t$. Since we know u_t $[= -\sqrt{(1-2/r)}\ \gamma]$ from v_{in}, λ_{in} and $E = \mathcal{E}$ at $r = r_{in} = 2.001r_s$, so enthalpy (h) can be expressed as cubic equation in Θ from enthalpy equation (2.71), which is

$$X_3\Theta^3 + X_2\Theta^2 + X_1\Theta + X_0 = 0, \tag{4.31}$$

where, $X_3 = 72\eta,\ X_2 = 3[16(\eta+1) - 3\eta\tilde{t}X_c],\ X_1 = 2[10 - 3\tilde{t}(X_c-1)(\eta+1)],\ X_0 = -4\tilde{t}(X_c-1)$ and $X_c = -\mathcal{E}/u_t$. Equation (4.31) gives three real roots but two are negative and only one is positive number, so we used positive root because negative temperature is unphysical and symbolized as Θ_{in}. Now, L_0 can be calculated from equation (2.57) by assuming $E = \mathcal{E}$ at r_{in}. Therefore, equation (2.57) can be written as,

$$E = \frac{\mathcal{E}}{\gamma_\phi \exp(X_f)}, \tag{4.32}$$

where, $\mathcal{E} = -hu_t$. Since, we assumed at very close to the horizon $E = \mathcal{E}$, so equation (4.32) must satisfy the relation, $\gamma_\phi \exp(X_f) = 1$. This condition written as,

$$-\frac{1}{\gamma_\phi}\frac{d\gamma_\phi}{dr} = \left[\left(\frac{r-3}{r-2}\right)\frac{l^2}{r^3\gamma_v^2} - \frac{u^r(L-L_0)^2}{2\nu hr(r-2)}\right]. \tag{4.33}$$

Now, simplifying just above equation with the help of equations (4.20) and (4.21), we get quadratic in L_0 equation. Which is

$$b_2L_0^2 + b_1L_0 + b_0 = 0, \tag{4.34}$$

where, $b_2 = u^r[\tilde{t}vv_\phi^2 d/(4\Theta DN\Gamma) + 1/h]/[2\nu r(r-2)]$, $b_1 = -2Lb_2 - a_1$ and $b_0 = b_2L^2 + a_1L + a_0$. Here, $a_1 = [u^r v_\phi^2(v - d/v)]/[\nu\gamma_v^2 l(1-2/r)D]$, $a_0 = vv_\phi^2[-1 + (5r-8)d/2 + (r-3)\gamma_\phi^2 d(v_\phi^2 + 1/v^2) + (r-2)(1-d/v^2)(1-2/\gamma_\phi^2)]/[r(r-2)D]$, $d = 2a^2/(\Gamma+1)$ and $D = [v - d(v_\phi^2 v + 1/v)]$. Equation (4.34) gives two real roots, one is greater than L_{in} and other less than $L_{\rm in}$, since viscosity transported angular momentum outward, so we have chosen second root, which is less than $L_{\rm in}$ in our study.

Now, we have $v_{\rm in},\ \Theta_{\rm in},\ L_{\rm in}$ at $r_{\rm in} = 2.001$ and L_0 or λ_0 at horizon by using four flow parameters, E, ξ, α and $\lambda_{\rm in}$, so we can integrate equations (4.20 - 4.22) simultaneously outward from $r_{\rm in}$.

4.3.1.2 Method to find sonic point and shock

For a particular set of input parameters, we have flow variables, $v_{\rm in}$ for a choice of $\delta < 1$, $\Theta_{\rm in}$ from equation (4.31) and L_0 from equation (4.34) at $r_{\rm in}$. Now we can integrate equations (4.20 - 4.22) from $r_{\rm in}$ outward and also check for critical point conditions (4.23 - 4.24), if these conditions are not satisfied, we have to change the choice of δ and again go for the next iteration. We have repeated this integration process until the critical point conditions are satisfied with change in δ. When these conditions are satisfied then we have location of critical point (r_{ci}) corresponding to a unique L_0 at the horizon and other flow variables at r_{ci} such as $L_c, \mathcal{E}_c, \Theta_c$ and v_c. Once we know the location of critical point for a particular set of parameters, we can integrate differential equations (4.20 - 4.22) inward and outward from the r_c and have full accretion solutions. These accretion solution may passes through more than one critical points, so to find such kind of solutions then we have to check for the shock transition. Therefore, when we integrate outward from critical point, we check for the shock conditions (4.25), using which we compute the pre-shock quantities (4.26). With these pre-shock quantities, we integrate outwards but now check for critical point conditions (4.23 - 4.24) to locate the outer critical point (r_{co}). Once we have obtained r_{co}, then the corresponding location of the shock jump is the shock location r_s. From r_{co} we can integrate outwards till the outer edge of the disc. And in such cases we have a complete shocked viscous accretion solution in general relativity, with all the flow variable obtained from very close to the horizon, through the inner sonic point r_{ci}, shock location r_s, through the outer sonic point r_{co} and finally to the outer edge of the accretion disc. Of course the accretion solution might just pass through either of the sonic points, but no shock may be obtained, which we term as shock-free solutions.

4.3.2 All possible accretion solutions

In this subsection we have generated all possible accretion solutions from the choice of set of accretion parameters (E, ξ, α and λ_{in}). In Figs. 4.20, we have drawn various flow variables for a shock solution, for the same set of parameters, $E = 1.0001, \alpha = 0.01, \xi = 1.0$ and $\lambda_{in} = 2.99$. In Fig. 4.20a, we have shown variation of accretion Mach number($M = v/a$) with radial distance ($log(r)$). Far away from the BH, flow has very small Mach number i.e., very low bulk velocity and low but finite temperature

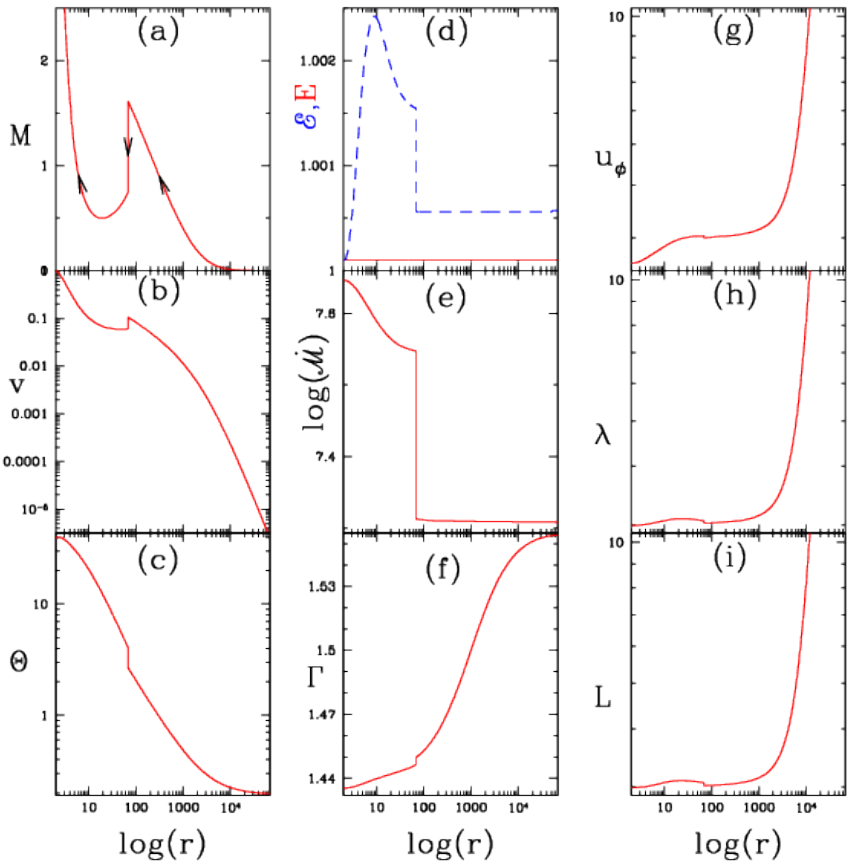

Figure 4.20: Variation of accretion flow variables - In plots (a-i), we have plotted variation of flow variables, Mach number (M), matter velocity (v), temperature (Θ), constant of motion (E) and relativistic Bernoulli parameter ($\mathcal{E}$), relativistic entropy accretion rate ($\dot{\mathcal{M}}$), adiabatic index (Γ), angular velocity ($u_\phi = l$), specific angular momentum (λ) and bulk angular momentum (L) with radial distance ($log(r)$), respectively. This accretion solution are generated for set of flow parameters, $E = 1.0001, \xi = 1.0, \alpha = 0.01$ and $\lambda_{in} = 2.99$. Chattopadhyay & Kumar to be submitted.

(see, for example $r \rightarrow$ large in Figs. 4.20b, c). Sudden vertical jumps in the curve of flow variables represent shock transition. In Fig. 4.20d, we have plotted variation of Bernoulli parameter ($\mathcal{E}$) with dashed line (blue) and grand specific energy parameter (E) with solid line (red) for viscous accretion disc and E is constant throughout the flow, similar to that shown by Kumar & Chattopadhyay (2013) in pseudo-Newtonian regime. The variation of entropy accretion rate ($\dot{\mathcal{M}}$), specific angular momentum (λ) and bulk angular momentum (L) shown in Fig. 4.20(e, h, i), respectively. They can be shown to be constant in inviscid accretion flow. One more defining difference between relativity and Newtonian regime is in the concept of angular momentum. In the Newtonian regime, the definition of angular-momentum for particles is not different from that in fluid. However, since in relativity any form energy may respond to gravity, the definition of specific angular momentum is different for particles and fluids in relativity. For particles the definition of specific angular momentum is u_ϕ or l, but for fluid the definition is u_ϕ/u_t or λ. So in conservative system for example a rotating particle in free fall in gravity, l is constant of motion, but for an adiabatic and inviscid fluid λ is a constant of motion and l varies in space. In Fig. 4.20g, we show how $u_\phi = l$ varies with r for viscous flow. Variation of adiabatic index Γ has been plotted in Fig. 4.20f. It shows, values of Γ is large at larger distance from the BH, which implies that the flow is non-relativistic and of lower temperature, while very close to the BH value of Γ is less and represents high temperature of the flow.

In Fig. 4.21, we present the full $E - L_0$ parameter space, and all possible accretion solutions, corresponding to $\xi = 1.0$ or $e^- - p^+$ flow, $\alpha = 0.01$. The solutions or the Mach number distributions M $(= v/a)$ for various parameters are plotted in the inset. In Fig. 4.21, the inset panel labelled 'a' presents M versus $\log(r)$, corresponding to location 'a' in the energy-angular momentum parameter space for coordinates $(E, L_0 = 1.0005, 2.701)$. Increasing L_0, we move to location 'b' $(E, L_0 = 1.0005, 2.851)$, 'c' $(E, L_0 = 1.0005, 2.951)$ and 'd' $(E, L_0 = 1.0005, 3.051)$. And then for higher E, solution of panel 'e' represents solution corresponding to location 'e' $(E, L_0 = 1.0015, 3.054)$, and panel 'f' corresponds to solution for $(E, L_0 = 0.9995, 2.948)$. The global transonic accretion solutions in the inset are represented by solid curve (black), and solutions which represent wind-type solutions are represented by the dotted curve (red). The dashed curve represents the transonic solution through which matter may pass. Accretion flows with any value of E and L_0 in the bounded region ABDEA has three sonic

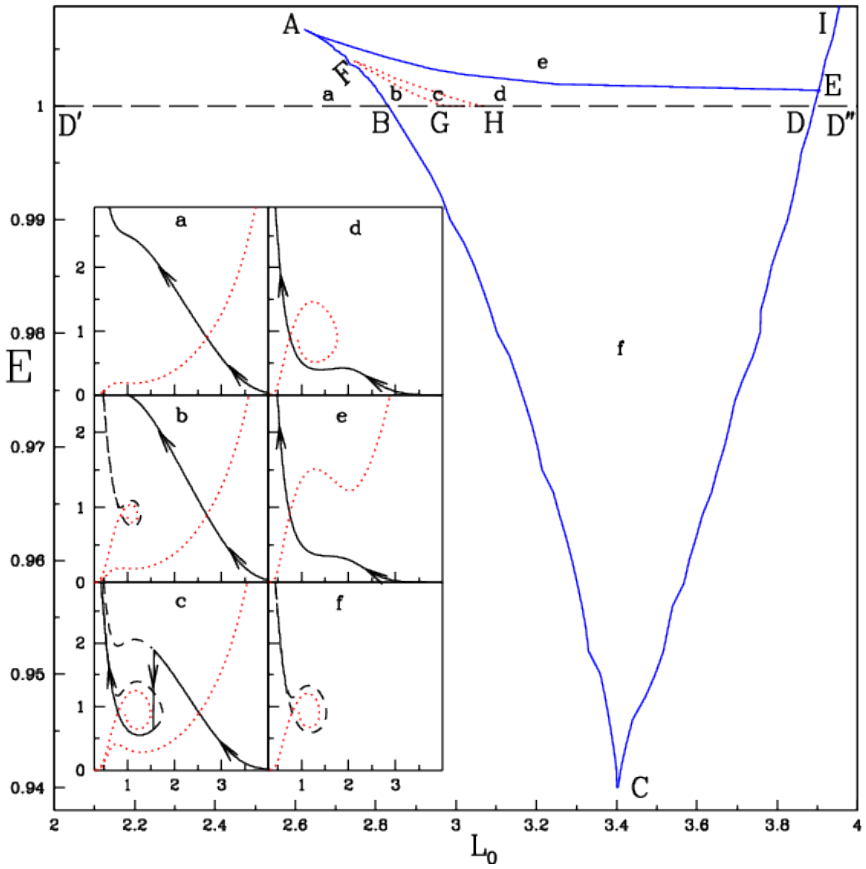

Figure 4.21: Division of parameter space - Division of the parameter space in $E - L_0$ according to number of critical points and representative accretion solutions. Area ABDEA and BCDB has three and two critical points, respectively. Area outside the bounded region D′BAEI and $E > 1$ has single critical point, but for regions outside D′BCDEI and $\varepsilon < 1$ no critical points exit. Inset panels labelled as a, b, c, d, e, and f present Mach number $M = v/a$ versus $\log(r)$, corresponding to the E, L_0 values at the locations marked in the parameter space. The dotted region FGHF is the shock parameter space, and in panel (c) the vertical jump shows the position of the shock. Accretion solutions are represented by solid (black) curve. This parameter space and the associated solutions are for $\xi = 1.0$ and $\alpha = 0.01$. Chattopadhyay & Kumar to be submitted.

points, and have a combination of closed and global solutions (*e.g.,*Figs. 4.21b - e). In the domain of multiple sonic points, if the steady shock solution cannot be obtained, and in addition, the solution through $x_{\rm co}$ does not connect the horizon and infinity, then the solutions through $x_{\rm co}$ cannot be determined exactly, and so, only solutions through inner sonic point are shown for Fig. 4.21d. The rough location of $x_{\rm co}$ can be ascertained for Fig. 4.21d, at the location where global solution through $x_{\rm ci}$ (solid, black), shows a maximum. An ADAF-type solution, *i.e.,* monotonic M distribution through $r_{\rm ci}$, is shown in Fig. 4.21e. On the other hand, flows with E and L_0 in the region BCDB have two critical points, and produces only closed topologies and therefore no global transonic solution (Fig. 4.21f). Within ABDEA, the bounded region FGHF produces steady, non-dissipative shocked solutions (*e.g.,*Fig. 4.21c), which are obtained from equations (2.27)-(2.30). The region outside BAEI and $E \geq 1$, there is only one sonic point (*e.g.,*Figs. 4.21a & f). Figure 4.21a, has low angular momentum and therefore produces a Bondi-type solution characterized by a single sonic point far away from the horizon, even in presence of dissipation. Figure 4.21e, on the other hand, produces a solution which is mostly subsonic and becomes transonic close to the horizon, and is similar to ADAF-type solutions. Regions outside D′BCD and $\varepsilon < 1$ and right of the curve DI, there exists no critical point, and consequently steady state black hole accretion is not allowed for such inner boundary conditions. As far as we know, investigation of viscous accretion disc in full GR with multi-species equation of state has not been done before. We have investigated full parameter space having accretion solutions for given viscosity parameter and plotted all type of possible accretion solutions. The coordinates of the important points which represents the multiple sonic point domain in the energy-angular momentum parameter space are A $(1.0066, 2.629)$, B $(1.0, 2.832)$, C $(0.940, 3.403)$, D $(1.0, 3.892)$ and E $(1.0014, 3.908)$.

4.3.3 Accretion-ejection solutions

In Fig. 4.22a, we have represented accretion Mach number M (dotted line) and jet Mach number M_j (solid line) with radial distances $log(r)$ and $log(r_j)$, respectively. Other plots in fig. 4.22(b-f) represents variation of jet flow variables, v_j (jet velocity), $\mathcal{E}_j$ (jet Bernoulli parameter or jet specific energy), Θ_j (jet temperature), Γ_j (jet adiabatic index) and $\dot{\mathcal{M}}_j$ (jet entropy accretion rate) with radial distance, respectively. This accretion- ejection solution correspond to four input parameters, which

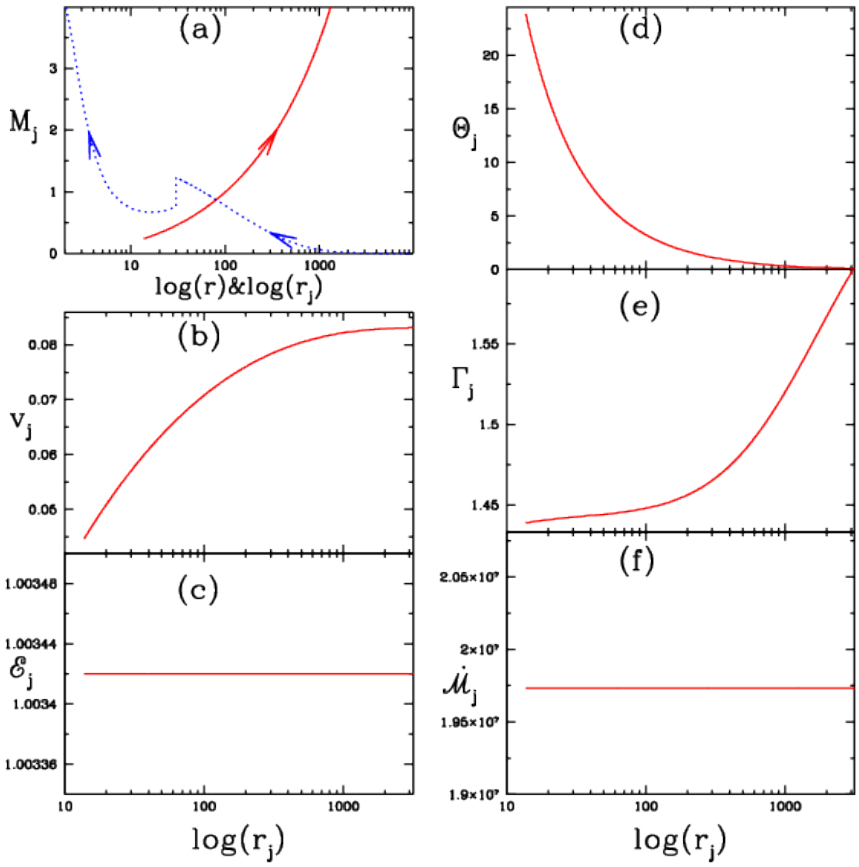

Figure 4.22: Jet flow variables - Represented the jet flow variables, $M_j, v_j, \mathcal{E}_j, \Theta_j, \Gamma_j$ and $\dot{\mathcal{M}}_j$ and accretion Mach number, M with radial distances $log(r_j)$ and $log(r)$. Here suffix 'j' represents flow variable with jet quantities. This jet solution associated with accretion disc parameters are $E = 1.002, L_0 = 2.8557, \xi = 1.0$ and $\alpha = 0.01$ and it generates shock at $x_s = 30.15$ and mass outflow $R_{\dot{m}} = 0.015$. Chattopadhyay & Kumar to be submitted.

are $E = 1.002, L_0 = 2.8557, \xi = 1.0$ and $\alpha = 0.01$. This produces shock location at $r_s = 30.15$ and mass outflow rate, $R_{\dot{m}} = 0.015$.

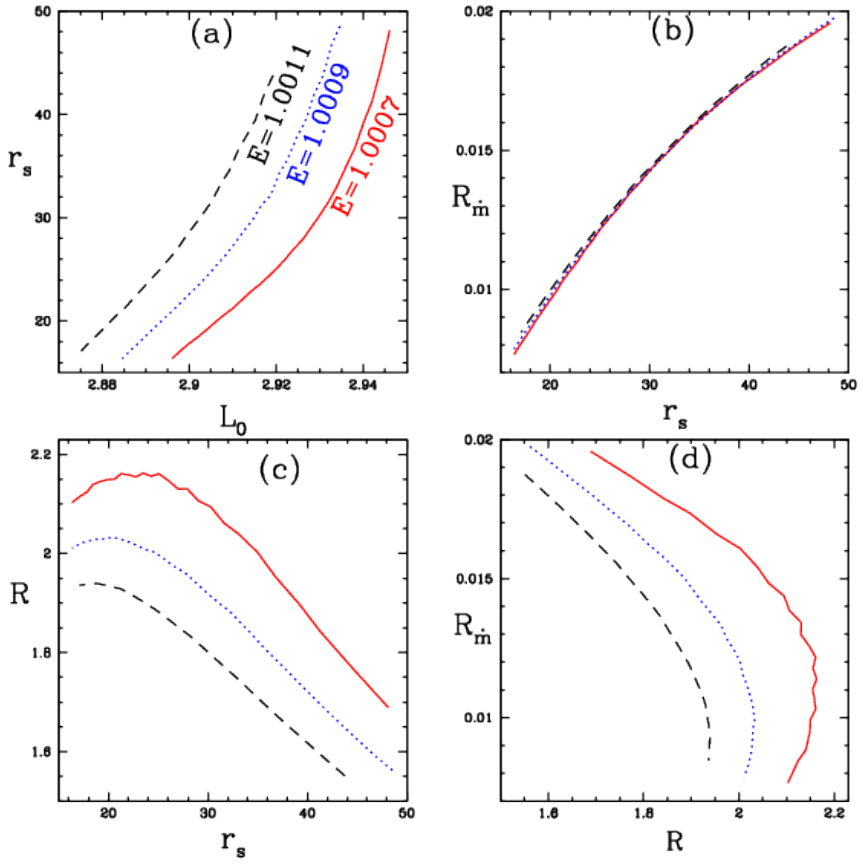

Figure 4.23: Mass outflow rate - Plot (a) variation of shock location (r_s) with bulk angular momentum (L_0 at horizon). Plot (c) variation of compression ratio (R) with r_s. Plot (b) and (d) variation of mass outflow rate $R_{\dot{m}}$ with r_s and R. Solid line, dotted line and dashed line curves are corresponding to energy constant $E = 1.0007, 1.0009$ and 1.0011, respectively and viscosity parameter, $\alpha = 0.01$ with composition parameter, $\xi = 1.0$. Chattopadhyay & Kumar to be submitted.

In fig. (4.23) we have shown variation of r_s with L_0 in plot (a), $R_{\dot{m}}$ with r_s in plot (b), R with r_s in plot (c) and $R_{\dot{m}}$ with R in plot (d) for $\alpha = 0.01, \xi = 1.0$. Each curve correspond to different energy, $E = 1.0007$ (solid-line), 1.0009 (dotted-line) and 1.0011 (dashed-line). For a given value of L_0 shock location(r_s) increases with E, but compression ratio $R = v_-/v_+$ decreases. So mass outflow rate $R_{\dot{m}}$ increases but only by a small amount because increase in energy is almost compensated by decrease in R. But $R_{\dot{m}}$ increases

with r_s means increase in post shock region, which drives the jet due to shock generated extra thermal energy in it.

It is very clear that the mass outflow rate is lesser than that in PW potential regime. This is because close to the horizon the solutions with PW potential is hotter than the solutions in general relativity, therefore the thermal driving in the post-shock general relativistic flow is lesser by almost 50% than that due to the PW potential. The compression ratio R increases as the shock location moves closer to the horizon, but if r_s moves within a range, R actually decreases. The $R_{\dot{m}}$ vs R plot is also multivalued (red, solid) unlike that due in the PW regime. These show a marked difference in the results obtained in pure general relativity than those obtained in PW potential, justifying our contention that ultimately all the solutions are to obtained using the general relativity for a better understanding of the physics around black holes.

5

Discussion and conclusion

Here, we discuss the conclusions of my thesis that are presented in different chapters. Quasars and microquasars may show strong jets, and microquasar jets are correlated with the spectral state of the objects. These jets and spectra are generated from fluid accretion discs. So, in this thesis we have studied the accretion disc, origin of the outflows or jets and change in jet strength with spectral index by changing disc parameter and effect on outflows with composition of the fluid. We started with a formalism which was comparatively a bit easy to implement and slowly added more and more physics. In that endeavour, we started with Newtonian fluids under the influence of gravity described by pseudo potential and Newtonian equation of state of the fluid, then progressed to relativistic equation of state and then into relativistic equations of motion and relativistic EoS of the fluid. In the following, we discuss the salient points presented in various chapters.

5.1 Discussion with chapters

In chapter 2, we presented the general fluid equations in pseudo-Newtonian regime, as well as, in full general relativistic regime. We have also discussed the general shock conditions for the accretion solutions and jet geometry for the rotating outflows. We have presented the form of the constant of motion for the general flow with appropriate assumptions. The form of Newtonian and relativistic EoS has also been presented in this chapter. The aim of this chapter is to present all the equations in systematic manner and to reduce repetition.

As has been pointed above, in chapter 3 we consider Newtonian fluid equations with non-relativistic EoS (read fixed Γ) of the fluid, but use a a form of viscosity which is proportional to the shear ($d\Omega/dx$) of the fluid. It is indeed elementary to show from the first principles, that a purely $x-\phi$ component of shear in axisymmetry is proportional to $d\Omega/dx$. All though many studies have been conducted on viscous fluid, but there has not been a thorough study of accretion-ejection system with this particular form of viscosity. Most of the work done earlier, suffers from the assumptions that either the viscous stress is proportional to gas pressure or total pressure. Little bit of work that has been conducted with this form of viscosity do not either study all possible accretion solution, or do not consider all possible shock solutions. So all those works are limited by their choice of assumptions. We on the other hand studied all possible accretion solution. In section (3.3), we have investigated all possible accretion solutions with this shear viscosity. While doing so, we have compared solutions with same inner and outer boundary conditions with change in viscosity, and have shown that these differences produce a significant difference in interpreting the results. Solutions with same inner boundary conditions (i.e., Fig. 3.2a), we found two critical viscosity parameters, the first one being the onset of shock (α_{cl}), and other being the one above which offset the standing shock (α_{cu}) and generates shock free global solution which is wholly subsonic except close to the horizon or ADAF-type solution. If inviscid solution is having shock (Fig. 3.2b) then only α_{cu} will exist, while if inviscid solution is I or $W-$ type then neither α_{cl} nor α_{cu} exists. For solutions with the same outer boundary condition, i.e., flow starting with same $E, \lambda_{inj} = \lambda_k(x_{inj})$ at some injection radius x_{inj} (e.g., Figs. 3.3), there would be an additional critical viscosity parameter α_1, which would allow a global solution, when $\alpha \geq \alpha_1$. We have also confirmed that fluids in such cases (e.g. Fig. 3.4), x_s, would decrease or increase with the increase in α and it depends on the chosen OBC. The decrease in x_s with the increase in α is interesting. Chakrabarti & Titarchuk (1995) for the first time argued that the post-shock disc is the elusive Compton cloud, which inverse-Comptonizes the pre-shock soft photons to produce power law tail. If the shock remains strong then we have the canonical hard state and when the shock becomes weak or disappear we have the canonical soft state. Moreover, Molteni et al. (1996a) showed that if the shock oscillates, it does with a frequency $\omega \sim x_s^{-\beta}$, where $\beta = 1 \ \rightarrow 3/2$. If the shock oscillates then the hard radiation from it would oscillate with the same frequency and could explain the mHz to few tens of Hz QPO observed

in stellar mass black hole candidates. Outburst phase in microquasars starts with low frequency QPOs in hard state, but as the source moves to intermediate states the QPO frequency increases to a maximum and then goes down in the declining phase, a fact well explained by approaching oscillating x_s with the increase of viscosity (Chakrabarti et al. 2009). Our steady state model also shows that if every other conditions at the outer boundary is same, then x_s decreases with the increase of α (Fig. A.1a), so we expect with the increase of viscosity the shock oscillation too will increase, and therefore the shock oscillation model of QPO seems to follow observations.

In section (3.4), we have studied radiatively and thermally driven self-consistent bipolar outflows. We can conclude that radiations from the pre and post shock disc participate in multistage acceleration of the jets (Figs. 3.7, 3.9 & 3.11). Since radiation from the post-shock disc affect the jet base, mass outflow and jet critical point, it is effective in acceleration at the subsonic part (Figs 3.10), but pre-shock disc radiation only affect and accelerate in the supersonic part of the jet and generates jets with high terminal speed (Figs 3.12). In Appendix (A), we have estimated $\ell_s/\ell_{ps}(x_s)$ from radiative losses from a set of solutions of advective disc. We used this relation to estimate ℓ_s, for given values of ℓ_{ps} and x_s. It has been observationally established that steady jets are observed from BH candidates, when the spectrum of the disc is in the hard state (Gallo et al. 2003). In our model, the presence of strong shock is similar to the hard state. We have shown that with increase of α for the disc solutions starting with same E, λ_{inj} at x_{inj} and calculated simultaneously disc-jet solutions, x_s decreases and the disc moved from low-intensity to brighter-intensity disc, then simultaneously the jet becomes stronger (outflow rate increases) and faster as shown in Fig. (3.14). This resembles qualitatively the transition of the disc from hard to intermediate-hard states with associated strengthening of the jets from slow jets to faster and stronger jet, as has been reported in observations. Since, x_s decreases with increase in α so, we may conjecture about evolution of $QPOs$ frequency as $\omega \sim x_s^{-\beta}, \beta = 1 \longrightarrow 3/2$ (Molteni et al. 1996a). We are still to include a few more physical processes in our disc-jet model, but our results qualitatively shows the correlation of disc spectral states and the jet states, as are observed in microquasars. Moreover, our result also indicates that, with multi-stage acceleration mechanism, truly relativistic jets from accretion disc are a distinct possibility.

In last section of this chapter, we have studied time-dependent hydrodynamic viscous

accretion flow in 2-D cylindrical geometry around Schwarzschild BHs. This simulation work is based on the Lagrangian Total Variation Diminishing (TVD) scheme and remap routine (Lee et al. 2011). TVD scheme strictly conserve all fluxes and was employed to capture the shock accurately, and Lagrangian method was employed to handle the angular momentum accurately. Here we have again investigated the shock-free and shock solution for inviscid and viscous flow. We found that simulation achieves steady state and matches with our analytical solutions quite accurately. This points at two important issue, one, the veracity of our analytical solutions, secondly the quality of the code. As the viscosity parameter is increased, the steady shock became unstable and produced quasi periodic oscillation. In simulations, shock solution produced bipolar outflows automatically. If one employ the methodology of Kumar et al. (2014) on to these numerical codes we can then study the relation between QPOs and jets too.

In the first section of chapter 4, we have studied effect of composition on accretion solutions and outflows with adiabatic fluid flow. This was the first work, which combined relativistic EoS with the dynamics of PW-potential. The first time, integral form of the entropy equation for adiabatic relativistic fluid was also obtained (equation 2.74) and is coined as relativistic adiabatic EoS. Using this, we redefined the entropy-accretion rate for the multi-species, variable Γ flow (Equation 2.75). Here we have shown that $e^- - e^+$ flow is thermally least relativistic and $e^- - p^+$ flow is also not most relativistic flow, which is consistent with the previous studies (Chattopadhyay 2008; Chattopadhyay & Ryu 2009 and Chattopadhyay & Chakrabarti 2011). Pure $e^- - e^+$ flow is not hot enough, It shows only one critical point for $\mathcal{E} < 1.0$ (Figs 4.2), very near to the BH, so no shocks and no bipolar outflows could be obtained. However, the flow with some amount of proton shows formation of multiple critical points and shocks (Figs 4.3). So, we can conclude that purely $e^- - e^+$ fluid jets are not found, although lepton-dominated jets are possible. But, we found that thermally the most relativistic flow is for $\xi = 0.27$, and consequently the maximum outflow rates can be obtained from a disc for such values of ξ (Fig.4.9). In Figs. (4.4) we show, a part from standing adiabatic shock other dissipative and isentropic shock can also form in the accretion flow.

In section 4.2 of chapter 4, we have investigated accretion onto black holes in presence of viscosity and cooling. As far as we know, such an effort has also not been undertaken before in the context of BH accretion. We obtained for the first time the expression of generalized Bernoulli parameter (equation 2.22), which is a constant of motion in

presence of viscosity and cooling in the accretion flow. In this section we have also discussed the general non-dissipative shock conditions, which are laid down from first principles by Landau & Liftshifz (1959), which we used in dissipative accretion flow. In Figs. (4.11), we presented the entire $\varepsilon - \lambda_0$ parameter space and identified the positions of various type of accretion solutions in the parameter space. We obtained again all possible transonic accretion solutions for a variety of boundary conditions, viscosity parameters and accretion rates in figs. (4.12). We also showed that increasing viscosity or cooling the shock moves closer to the horizon, provided flow is launched with same outer boundary (Figs. 4.13), this we have also showed with fixed Γ EoS. We have considered bremsstrahlung and synchrotron processes as the dominant cooling processes. The inverse Comptonization process has been taken into consideration through a fitting function presented in appendix (A), where the fitted function is the Compton efficiency for all kind of seed photons (equation A.1). We have considered this fitted function as generic, as an obvious effort to simplify things related to Comptonization but nonetheless to incorporate some effects of it in the solution. Since the post shock disc has a jump in temperature and density, it is puffed up, and can hence intercept additional photons from the post shock disc and Comptonize it. A shock free disc has smooth solutions and therefore will not be able to intercept additional photons, reducing the Comptonization efficiency. As a result we found that the shocked disc is more luminous than the shock free disc, even when they start with the same outer boundary condition (Figs. 4.14). We have shown that shock solutions can be found for high enough viscosity, as well as, very high accretion rates (Figs. 4.15, 4.17 & 4.18). We have compared the shock parameter space for both non-dissipative shocks and dissipative shocks, and if the total shocked domain in the $\varepsilon - \lambda_0$ parameter space is considered then it is indeed quite significant. Furthermore, Fig. (4.18) shows a very interesting phenomena in which, for high accretion rate and moderate viscosity parameter values, luminosities of up to and over Eddington limit is possible. This is very interesting, because Fig. (4.18) show that the radiative efficiency also depends on the accretion rate and other disc parameters, and both radiatively inefficient flow and efficient flow is possible by tuning the matter supply at the outer boundary. Figure 4.18, further show that luminosities up to $\ell \sim 10^{39}$erg s^{-1} for BHCs of $M \sim 10 M_{\odot}$ i.e., stellar mass black holes, and $\ell \sim 10^{46}$erg s^{-1} for BHCs of $M \sim 10^{8} M_{\odot}$ for super massive black holes can be achieved in advective and shocked accretion domain even when only non-rotating

black holes are assumed. This means higher luminosities may be achieved for shocked accretion flow if Kerr black holes are considered. The luminosities are similar to ULX luminosities. Furthermore, since super-Eddington accretion is possible, then the growth of the central mass also comes into the ambit of future study. Simple minded estimates show, that a black hole of $10M_{\odot}$ will increase its mass by 10 % in about 5 Myr, if it continues to accrete at $10\dot{M}_{\rm Edd}$. Here, we have again estimated mass outflow rate for general dissipative flow (Figs. 4.19), and we have found same type of variations as in adiabatic flow.

In section 4.3 of chapter 4, we have presented viscous accretion solutions with full relativistic regimes. There are few efforts to study viscous accretion flows (Peitz & Appl 1997; Gammie & Popham 1998; Takahashi 2007). However, an inflow outflow solution has not been attempted before. While Peitz & Appl (1997) solved general relativistic viscous equations of motion for the first time, but he considered fixed Γ EoS. Gammie & Popham (1998) used variable Γ EoS in Kerr metric, while Takahashi solved viscous equations of motion also with variable Γ but in Kerr-Schild metric. And none of them estimated mass loss. Here, we have perfected a general methodology for the calculation of critical point r_c and critical bulk angular momentum L_c for a given values of λ_{in} at r_{in} and constant of motion E. We have also defined new general Bernoulli parameter in equation (2.57) for viscous flow and which is also a constant of motion (Fig. 4.20d, solid line). Here, we also investigated all possible accretion solutions and division of parameter space in general relativity (Figs 4.21) as in pseudo-Newtonian geometry and estimated the outflow rate from shocked accretion solutions. All type of possible accretion solutions and outflow from a general relativistic shocked disc qualitatively matches with solutions of PW-potential around BH. But few things are different from the solutions with PW- potential and they are (I) general relativity fully satisfied the inner boundary condition of the horizon but PW-potential is not good very close to the horizon, (II) GR shows the maximum in the compression ratio (R) of shock solutions (Figs. 4.23), which is not found in PW-potential solutions (Fig. 4.19). Since BHs are relativistic objects. So, accretion flow must be investigated with full general relativistic fluid around BHs.

5.2 Thesis summary and Future prospects

We have generated outflow self-consistently from the shock accretion disc solutions without using any external systematic forces. It is ejected due to generated extra thermal force in the post-shock region and this outflow matter propagated along the two funnel walls (Fig. 2.1). Interesting thing is that this outflow has entropy values in between the entropy of pre-shock and post-shock flow. So, this naturally explains the automatic generation of outflow from the shocked disc. We have shown that as jets originate from post-shock disc becomes stronger as the spectral state moves from LS to IS as observed in microquasars. Since post shock disc is the seat of hard radiation, so inward motion of shock location with increase in viscosity could explain the evolution of the QPOs. Since generated outflow due to extra thermal energy in the strong shock solutions are weak jets and having jet velocity $\lesssim 0.1c$. So, it require acceleration and we have accelerated it by using pre and post shock radiations as a form of multistage acceleration. We get mildly relativistic jets as observed in IS of microquasars. Keeping the idea of multistage acceleration, in future we will extend this by using Keplerian component of the disc and magnetic field component. Regarding magnetic field component we will proceed to magneto-hydrodynamic (MHD) formalism for accretion disc in future. Moreover, since shock location moves inward when increasing disc accretion rates, while keeping outer boundary fixed as shown in section (4.2) of chapter 4, we can also conclude that the relation between outflow, spectral states and evolution of QPOs can also be shown by changing only accretion rate. We expect that, with the increase of viscosity parameter the decrease in the mean shock location would increase the QPO, and would continue to increase, as long as, the post-disc is not disrupted. Since we showed that the disc becomes luminous and the jet strength increases, so our result corroborates exactly the observations that, in the out bursting phase the microquasar would move from low-hard state to intermediate states accompanied by the increase in QPO and jet strength, but with the disruption of the post-shock disc the QPO and the jet will disappear, only to repeat the entire sequence as the microquasar achieves right outer boundary condition. With the study of relativistic EoS, we can conclude that pure leptonic jets are unlikely to form in nature around the black holes. We got maximum outflow rate around corresponding maximally relativistic flow composition around $\xi = 0.27$. We got disc total luminosity range from 0.001 to 1.2

times the Eddington luminosity. Which could explain the radiatively inefficient and efficient disc flow and moreover disc radiative efficiency increases with increasing accretion rate. Since in LS source is radiatively inefficient and as it moves from LS to IS radiative efficiency increases, so increasing efficiency due to increase in accretion rate seems to follow observations. This high accretion rate can explain the hyper accreting ultra luminous $X-$ray source with higher than 10% radiative efficiency. Since radiative efficiency also increases with Kerr parameter, so, in future we will extend this study to rotating metric and that can help in understanding of generation of highly relativistic and collimated jets in a better way around BHs and highly luminous $X-$ ray source.

Appendix A

Estimation of post-shock luminosity from pre-shock radiations

We consider a general radiative transfer model (Chakrabarti & Mandal 2006) which consists of two components, a Keplerian disc on the equatorial plane and a sub-Keplerian component on the top of the Keplerian disc. The Keplerian disc supplies the multi-colour black body photons and a fraction of that photons are inverse-Comptonized by post-shock region. The pre-shock sub-Keplerian disc emits radiation via bremsstrahlung and synchrotron process whereas the post-shock region produces the same as in pre-shock along with the Comptonization of the local and intercepted soft photons. We calculate the radiation spectrum of accretion disc using the viscous transonic shocked solution for a given outer boundary condition $E = 0.001, \lambda_{inj} = 18.592$ at $x_{inj} = 10^4$. For a given value of α, a shock is formed at x_s. The frequency integrated pre-shock and post-shock luminosity is then calculated. It has been shown in Kumar & Chattopadhyay (2013) that for the same set of boundary conditions, x_s decreases if α is increased. In our case for a range of $0.0091 \leq \alpha \leq 0.01$, for flows starting with the same injection values mentioned above, the shock location changes from $x_s = 131 \rightarrow 7.8$ (Fig. A.1). We calculate the ratio of post-shock to pre-shock luminosity ℓ_s/ℓ_{ps} for different values of x_s in the range mentioned above and it has been plotted by dots in Fig. (A.1b). In Fig. A.1c we plot the associated variation in photon index, which shows the spectra softens as shock moves inward. The ratio

(ℓ_s/ℓ_{ps}) increases initially as the shock move inward, reaching a maximum value and then decreases sharply. This behaviour is due to fact that initially as shock moves inward both post-shock temperature and density increases and hence post-shock luminosity increases but as shock reaches closer to central object the pre-shock luminosity ℓ_{ps} increases and the increased supply of pre-shock photons cools down the post-shock flow, and therefore the ratio would decrease too. We have fitted a polynomial through the model data points and this general behaviour of ℓ_s/ℓ_{ps} with x_s is used to calculate ℓ_s for given value of ℓ_{ps}. The fitted polynomial for the relation between post-shock and pre-shock disc luminosity is,

$$f(x_s) = -0.659234 + 0.127851\ x_s - 0.00043\ x_s^2 - 1.13 \times 10^{-6}\ x_s^3, \qquad \text{(A.1)}$$

where, $f(x_s)$ is the fitted function for ℓ_s/ℓ_{ps}.

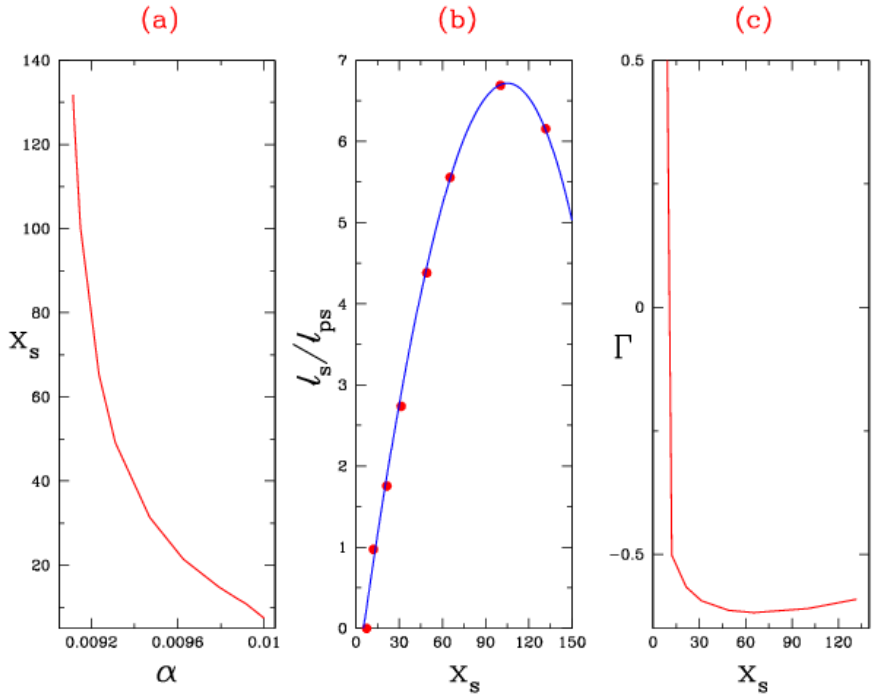

Figure A.1: Variation of shock location and photon index - Variation of (a) shock location(x_s) with disc viscosity parameter(α), and (b) ratio of ℓ_s/ℓ_{ps} with shock locations, and (c) the photon index Γ for the same injection values $E = 0.001, \lambda_{inj} = 18.592$ at disc outer boundary, $x_{inj} = 10^4$ but varying viscosity parameter(α) from 0.0091 to 0.01. In plot (b) dot points are actual data points and solid line is the fitted polynomial.Kumar et al. (2014).

Bibliography

Becker P. A., Das S., Le T., 2008, ApJL, 677, L93 9, 19, 39

Becker P. A., Le T., 2003, ApJ, 588, 408 32, 33

Biretta J. A., Meisenheimer K., 1993, in Jets in Extragalactic Radio Sources, edited by H.-J. Röser, K. Meisenheimer, vol. 421 of Lecture Notes in Physics, Berlin Springer Verlag, 159 5

Blandford R. D., Znajek R. L., 1977, MNRAS, 179, 433 111

Bondi H., 1952, MNRAS, 112, 195 7, 32

Bowyer S., Byram E. T., Chubb T. A., Friedman H., 1965, Science, 147, 394 3

Castro-Tirado A. J., Brandt S., Lund N., 1992, IAUCirc, 5590, 2 4

Chakrabarti S., Titarchuk L. G., 1995, ApJ, 455, 623 126

Chakrabarti S. K., 1989, ApJ, 347, 365 9, 19, 37, 68, 76, 77

Chakrabarti S. K., 1990, Theory of transonic astrophysical flows 9, 32

Chakrabarti S. K., 1996, ApJ, 464, 664 9, 19

Chakrabarti S. K., 1999, A&A, 351, 185 89

Chakrabarti S. K., Mandal S., 2006, ApJL, 642, L49 54, 60, 133

Chandrasekhar S., 1939, An introduction to the study of stellar structure 26

Chattopadhyay I., 2005, MNRAS, 356, 145 51

Chattopadhyay I., 2008, in American Institute of Physics Conference Series, edited by S. K. Chakrabarti, A. S. Majumdar, vol. 1053 of American Institute of Physics Conference Series, 353–356 25, 26, 112

Chattopadhyay I., Chakrabarti S. K., 2000, ArXiv Astrophysics e-prints 51

Chattopadhyay I., Chakrabarti S. K., 2002, MNRAS, 333, 454 31, 51

Chattopadhyay I., Chakrabarti S. K., 2011, International Journal of Modern Physics D, 20, 1597 76, 77

Chattopadhyay I., Das S., 2007, NewA, 12, 454 9, 19, 21, 43

Chattopadhyay I., Das S., Chakrabarti S. K., 2004, MNRAS, 348, 846 51

Chattopadhyay I., Kumar R., 2013, in Astronomical Society of India Conference Series, edited by S. Das, A. Nandi, I. Chattopadhyay, vol. 8 of Astronomical Society of India Conference Series, 19–25 17, 27

Chattopadhyay I., Ryu D., 2009, ApJ, 694, 492 25, 26, 112

Chen X., Abramowicz M. A., Lasota J.-P., 1997, ApJ, 476, 61 9

Choudhuri A. R., 1998, The physics of fluids and plasmas : an introduction for astrophysicists / 13

Colbert E. J. M., Ptak A. F., 2002, ApJS, 143, 25 1

Das S., 2007, MNRAS, 376, 1659 19

Das S., Becker P. A., Le T., 2009, ApJ, 702, 649 9, 39, 46

Das S., Chattopadhyay I., 2008, NewA, 13, 549 9, 19

Das S., Chattopadhyay I., Chakrabarti S. K., 2001, ApJ, 557, 983 37, 68

Doeleman S. S., Fish V. L., Schenck D. E., et al., 2012, Science, 338, 355 5

Fabbiano G., Kim D.-W., Fragos T., et al., 2006, ApJ, 650, 879 1

Fender R., Gallo E., 2014, SSRv, 183, 323 5

Fender R. P., Belloni T. M., Gallo E., 2004, MNRAS, 355, 1105 6

Fender R. P., Gallo E., Russell D., 2010, MNRAS, 406, 1425 111

Feng H., Soria R., 2011, NewAR, 55, 166 1

Frank J., King A. R., Raine D. J., 1985, Accretion power in astrophysics 17

Fukue J., 1987, PASJ, 39, 309 9, 77

Gallo E., Fender R. P., Pooley G. G., 2003, MNRAS, 344, 60 4, 127

Gammie C. F., Popham R., 1998, ApJ, 498, 313 130

Genzel R., Eisenhauer F., Gillessen S., 2010, Reviews of Modern Physics, 82, 3121 1

Gierliński M., Middleton M., Ward M., Done C., 2008, Nature, 455, 369 4

Greiner J., 2001, ArXiv Astrophysics e-prints 4

Gu W.-M., Lu J.-F., 2004, Chinese Physics Letters, 21, 2551 9, 17, 19

Harten A., 1983, Journal of Computational Physics, 49, 357 66, 67

Ichimaru S., 1977, ApJ, 214, 840 9

Junor W., Biretta J. A., Livio M., 1999, Nature, 401, 891 5

Kumar R., Chattopadhyay I., 2013, MNRAS, 430, 386 17, 19, 21, 53, 68, 77, 133

Kumar R., Chattopadhyay I., 2014, MNRAS, 443, 3444 17, 68, 97, 98, 101, 103, 105, 106, 107, 109

Kumar R., Chattopadhyay I., Mandal S., 2014, MNRAS, 437, 2992 19, 21, 68, 93, 128, 135

Kumar R., Singh C. B., Chattopadhyay I., Chakrabarti S. K., 2013, MNRAS, 436, 2864 27, 68, 76, 85, 87, 88, 90, 91, 92

Landau L. D., Lifshitz E. M., 1959, Fluid mechanics 13, 18, 19, 20

Lanzafame G., Molteni D., Chakrabarti S. K., 1998, MNRAS, 299, 799 9, 43

Lee S.-J., Ryu D., Chattopadhyay I., 2011, ApJ, 728, 142 43, 67, 128

Lewin W. H. G., van der Klis M., 2006, Compact Stellar X-ray Sources 4

Liang E. P. T., Thompson K. A., 1980, ApJ, 240, 271 9, 77

Lightman A. P., Eardley D. M., 1974, ApJL, 187, L1 9

Liu Q. Z., Mirabel I. F., 2005, A&A, 429, 1125 1

Lu J.-F., Gu W.-M., Yuan F., 1999, ApJ, 523, 340 9, 39

Margon B., 1984, ARA&A, 22, 507 5

Michel F. C., 1972, Ap&SS, 15, 153 7

Mihalas D., Mihalas B. W., 1984, Foundations of radiation hydrodynamics 31

Miller-Jones J. C. A., Sivakoff G. R., Altamirano D., et al., 2012, MNRAS, 421, 468 4

Mirabel I. F., Rodrigues I., 2003, Science, 300, 1119 1

Mirabel I. F., Rodríguez L. F., 1994, Nature, 371, 46 4, 5

Mirabel I. F., Rodriguez L. F., Cordier B., Paul J., Lebrun F., 1992, Nature, 358, 215 4

Molteni D., Lanzafame G., Chakrabarti S. K., 1994, ApJ, 425, 161 9, 36

Molteni D., Ryu D., Chakrabarti S. K., 1996a, ApJ, 470, 460 9, 20, 68, 126, 127

Molteni D., Sponholz H., Chakrabarti S. K., 1996b, ApJ, 457, 805 9

Nagakura H., Yamada S., 2009, ApJ, 696, 2026 36

Nandi A., Debnath D., Mandal S., Chakrabarti S. K., 2012, A&A, 542, A56 4

Nandi A., Radhika D., Seetha S., 2013, in Astronomical Society of India Conference Series, edited by S. Das, A. Nandi, I. Chattopadhyay, vol. 8 of Astronomical Society of India Conference Series, 71–77 4

Narayan R., Yi I., 1994, ApJL, 428, L13 9

Novikov I. D., Thorne K. S., 1973, in Black Holes (Les Astres Occlus), edited by C. Dewitt, B. S. Dewitt, 343–450 8

Paczyński B., 1982, Mitteilungen der Astronomischen Gesellschaft Hamburg, 57, 27 9

Paczyńsky B., Wiita P. J., 1980, A&A, 88, 23 9, 10, 111

Pasham D. R., Strohmayer T. E., Mushotzky R. F., 2014, Nature, 513, 74 1

Peitz J., Appl S., 1997, MNRAS, 286, 681 23, 130

Press W. H., Teukolsky S. A., Vetterling W. T., Flannery B. P., 1992, Numerical recipes in FORTRAN. The art of scientific computing 68

Rees M. J., Begelman M. C., Blandford R. D., Phinney E. S., 1982, Nature, 295, 17 9

Remillard R. A., McClintock J. E., 2006, ARA&A, 44, 49 4

Riffert H., Herold H., 1995, ApJ, 450, 508 23

Rybicki G. B., Lightman A. P., 1979, Radiative processes in astrophysics 93

Ryu D., Chattopadhyay I., Choi E., 2006, ApJS, 166, 410 26

Ryu D., Ostriker J. P., Kang H., Cen R., 1993, ApJ, 414, 1 66

Shakura N. I., Sunyaev R. A., 1973, A&A, 24, 337 8, 43, 67

Shapiro S. L., 1973, ApJ, 180, 531 7

Shapiro S. L., Teukolsky S. A., 1983, Black holes, white dwarfs, and neutron stars: The physics of compact objects 50, 93

Shaposhnikov N., Swank J., Shrader C. R., et al., 2007, ApJ, 655, 434 4

Shaposhnikov N., Titarchuk L., 2007, ApJ, 663, 445 4

Shaposhnikov N., Titarchuk L., 2009, ApJ, 699, 453 4

Sobolewska M. A., Gierliński M., Siemiginowska A., 2009, MNRAS, 394, 1640 4

Svensson R., 1982, ApJ, 258, 335 93

Swartz D. A., Soria R., Tennant A. F., Yukita M., 2011, ApJ, 741, 49 1

Takahashi R., 2007, MNRAS, 382, 567 130

Thorne K. S., Price R. H., 1975, ApJL, 195, L101 9

Ziółkowski J., 2014, MNRAS, 440, L61 4

SCHOOL OF STUDIES IN PHYSICS AND ASTROPHYSICS
Pt. RAVISHANKAR SHUKLA UNIVERSITY,
RAIPUR - 492010 , CHHATTISGARH (INDIA)

Dr. R. N. Baghel
Ph. D. (IIT Delhi), MCA,
Diploma in English,
Prof. & Head

Phone : (Mo) 9198934-24482
: (O) (0771) 2262864
: (R) (0771) 2262739
Fax : (0771) 2262583,2262857
Email : rnbaghel20@gmail.com

Ref. :1044/Phy/15 Date :12-03-2015

List of Publications

This is to certify that **Mr. Rajiv Kumar** has following publications.

`Estimation of the mass outflow rates from viscous accretion discs'; **Kumar R.**, Chattopadhyay I., 2013, MNRAS, 430, 386. **(Impact Factor 5.2)**

`Effect of the flow composition on outflow rates from accretion discs around black holes'; **Kumar R.**, Singh C. B., Chattopadhyay I., Chakrabarti S. K., 2013, MNRAS, 436, 2864. **(Impact Factor 5.2)**

`Radiatively and thermally driven self-consistent bipolar outflows from accretion discs around compact objects'; **Kumar R.**, Chattopadhyay I., Mandal S., 2014, MNRAS, 437, 2992. **(Impact Factor 5.2)**

`Dissipative advective accretion disc solutions with variable adiabatic index around black holes'; **Kumar R.**, Chattopadhyay I., 2014, MNRAS, 443, 3444. **(Impact Factor 5.2)**

`Time-dependent viscous accretion flow in two-dimensional cylindrical geometry'; Lee S-J, Chattopadhyay I., **Kumar R.**, Ryu D., Hyung S. **to be submitted soon.**

`Estimation of mass outflow rates from general relativistic advective accretion discs'; Chattopadhyay I. **Kumar R. to be submitted soon.**

Conference proceedings:

`Study of jet properties around compact objects with the change in accretion disc parameters';
Kumar, R., Chattopadhyay, I., Mandal, S., 2013, ASInC, 8, 147.

`Accretion disc spectrum in presence of mass outflow around black holes';
Mandal, S., **Kumar, R.**, Chattopadhyay, I., 2013, ASInC, 8, 45.

`Viscous accretion disc around black holes with variable adiabatic index';
Chattopadhyay, I., **Kumar, R.**, 2013, ASInC, 8, 19.

`Effect of equation of state and composition on relativistic flows';
Chattopadhyay, I., Mandal, S., Ghosh, H., Garain, S., **Kumar, R.**, Ryu, D., 2012, ASInC, 5, 81.

Chairman
Departmental Research Committee (DRC)
School of Studies in Physics & Astrophysics
Pt. Ravishankar Shukla University, Raipur, (C. G), 492010 India